Department of Physics and Astronomy
University of Heidelberg

Master Thesis in Physics
submitted by

Ido Siovitz

born in Haifa (Israel)

Submitted February 2022

Topological Excitations and Universal Scaling of the One-Dimensional Spin-1 Bose-Einstein Condensate Far from Equilibrium

This Master Thesis has been carried out by Ido Siovitz

at the

Kirchhoff-Institut für Physik in Heidelberg

under the supervision of

Prof. Dr. Thomas Gasenzer

Abstract

In this thesis, we numerically investigate the dynamics of a one-dimensional spin-1 Bose-Einstein condensate far from equilibrium following a sudden Hamiltonian parameter change, known as a parameter quench. Utilizing the truncated Wigner approximation and a split-step Fourier algorithm to solve the Gross-Pitaevskii equations, we simulate a cloud of ^{87}Rb-like atoms in a one-dimensional setting after a quench of the quadratic Zeeman effect q. The resulting dynamics are characterized by a critically slowed time evolution described by self-similar universal scaling of correlation functions with time associated with a non-thermal fixed point with dynamical exponents $\alpha \approx \beta \approx 0.25$. The emergence and subsequent dynamics of topological objects in the system are thought to be driving mechanisms for the universal time evolution. We classify the topological defects in the system and investigate their contribution to the coarsening of the governing length scales. We find evidence of instantons in the system and study their contribution to spin domain coarsening. Motivated by recent experiments, we investigate the quench dynamics of a system with vector solitons imprinted onto the initial condition via local spin rotations. Lastly, we explore the q dependency of the universal scaling and find a spectrum of effective scaling exponents.

Zusammenfassung

Die vorliegende Arbeit befasst sich mit numerischen Untersuchungen der Dynamik eines eindimensionalen Bose-Einstein Kondensats weit vom thermischen Gleichgewicht nach einer plötzlichen Änderung eines Parameters im Hamiltonian, auch bekannt als Quench. Mithilfe der Truncated Wigner Näherung und einer Split-Operator-Fourier Methode werden die Gross-Pitaevskii Gleichungen gelöst, womit eine ^{87}Rb -ähnliche Atomwolke in einer eindimensionalen Geometrie nach einem Quench des quadratischen Zeemaneffekts q simuliert wird. Die resultierende Dynamik wird charakterisiert durch eine verlangsamte universelle selbstähnliche Zeitentwicklung der Korrelationsfunktionen verknüpft mit einem nicht-thermischen Fixpunkt mit dynamischen Exponenten $\alpha \approx \beta \approx 0.25$. Die Entstehung und darauffolgende Zeitentwicklung von topologischen Objekten im System gelten als antreibende Mechanismen der universellen Dynamik. Die topologischen Defekte des Systems werden klassifiziert und ihr Beitrag zu der Vergrößerung der herrschenden Längenskalen wird untersucht. Es werden Nachweise für die Existenz von Instantonen gefunden und ihr Einfluss auf die Vergröberung von Spindomänen wird analysiert. Motiviert durch jüngste Experimente wird die Dynamik des Systems nach einem Quench mit Vektorsolitonen, die im Anfangszustand mit Hilfe von Rotationen im Spinraum erzeugt werden, betrachtet. Zuletzt wird die Abhängigkeit des Skalierverhaltens von q erkundet und folglich wird ein Spektrum von effektiven Skalierungsexponenten gefunden.

Contents

List of Figures

1. Introduction

The study of quantum many-body systems far from equilibrium has been of particular interest in the past few years, since the behavior of such systems poses an opportunity to gain a deeper understanding of the mechanisms underlying the time evolution of many physical configurations. The notion of universal non-thermal fixed points (NTFPs) gives us a strong tool to probe macroscopic universal dynamics, thus allowing us to classify many systems with only a handful of macroscopic parameters [1, 2]. The idea of NTFPs is based on the phenomenological understanding that a system far from equilibrium will reach a regime of critically slowed dynamics during its time evolution towards thermal equilibrium. This regime is connected to the system's vicinity to a stationary non-equilibrium state associated with an NTFP [3]. The critically slowed down dynamics are characterized by a self-similar time evolution of the order parameter correlation functions [4, 5, 6, 7], in analogy to critical phenomena in equilibrium, where such a fixed point acts as a universal attractor belonging to a renormalization group.

The aforementioned universal behavior will apply to a large range of initial conditions, reflecting the emergence of universality classes, each characterized by its own set of universal scaling exponents. It is at this point that the true advantage of such a description becomes clear: The time evolution of the system does not depend on the microscopic details of the system anymore, and a variety of different systems belonging to the same universality class will all behave identically on the macroscopic level. Therefore, it presents us with an opportunity to understand and predict the real-time evolution of various systems, such as quark-gluon plasmas in QCD [8] or the post inflationary dynamics in the early universe [9], by probing a more experimentally accessible system of the same universality class.

Due to the high degree of experimental control over various system parameters, isolated ultracold quantum many-body systems such as Bose-Einstein condensates (BECs) present an excellent opportunity to probing and simulating far-from-equilibrium physics [3, 10, 6]. So-called spinor Bose gases with multiple components corresponding to the respective magnetic sublevels are of special interest, since the interactions in their spin degree of freedom allow us to observe different phenomena such as phase transitions, spin-mixing dynamics [11], spin domain formation and its subsequent coarsening dynamics [4].

This thesis will concentrate on numerically investigating the far-from-equilibrium dynamics of the one-dimensional spin-1 BEC, which is a Bose gas with three components corresponding to the three different magnetic sublevels $m_f = -1, 0, 1$. We will explore the dynamics far from equilibrium via a sudden change of a parameter in the spin-1 Hamiltonian, forcing the system through a second order quantum phase transition (QPT), an operation known as a parameter quench. In theoretical investigations of multi-component $U(N)$ symmetric systems, a low-energy effective theory of relative phase excitations was developed to predict the far-from-equilibrium scaling behavior of correlations [12]. The appearance of $U(N)$ symmetry breaking terms in the spin-1 Hamiltonian due to the additional spin degrees of freedom results in a different scaling behavior, demonstrated by Ref. [4]. The coarsening dynamics in the system are attributed to various mechanisms governing the time evolution, such as the conserved redistribution of collective excitations or by the appearance, disappearance and scattering of topological excitations in the system [13]. The aim of this thesis is to better understand the underlying mechanisms of the coarsening dynamics in the spin-1 BEC. To this end, we concentrate on classifying the various (quasi)topological excitations in the system by utilizing different numerical approaches to detecting and characterizing these objects.

In chapter 2, we introduce the theoretical model of the spin-1 BEC. We begin by defining the full quantum Hamiltonian of the system and characterize its symmetries. Unfortunately, the full quantum dynamics of the system are analytically inaccessible. Therefore, we introduce the mean-field approximation of the system and derive the classical equations of motion, known as the Gross-Pitaevskii equations (GPEs). We present the four phases of the spin-1 mean-field ground states and explain the quench setup of the quadratic Zeeman effect q, with which we create an extreme out-of-equilibrium initial condition. Then, we go over the effective one-dimensional description, modifying the GPEs slightly to accommodate for the new geometry. The chapter then proceeds and moves beyond mean-field theory by introducing small quantum fluctuations into the system via Bogoliubov theory. We discuss the emerging dynamical instabilities and the predictions of the short-time evolution of the system following a parameter quench.

The subsequent chapter 3 then introduces the concepts of topology, giving a brief introduction to the notion of homotopy theory and homotopy groups. This is then taken as a basis to apply these theories to derive solitonic field configurations in a simple ϕ^4 field theory. The importance and calculation of topological currents and charges will also be discussed, and the idea of instantons in the context of a general Yang-Mills theory will be presented. Concluding the chapter, we will connect the ideas of homotopy groups to the symmetries of the spin-1 Hamiltonian and derive the order parameter manifolds for relevant two phases of the spin-1 BEC. The resulting homotopy groups provide an indication of which topological objects can be found in the system, possibly affecting the resulting dynamics.

In chapter 4, we discuss our numerical setup with which we simulate the time evolution of the spinor BEC. We motivate the chosen method for simulating semi-classical dynamics beyond the mean-field description: the truncated Wigner approximation (TWA). The method includes the sampling of quantum noise from the initial probability distribution of our quantum state, given by its Wigner function which, due to highly occupied modes, acts as a classical probability distribution function. We subsequently solve the classical equations of motion by means of a split-step Fourier method which will be outlined in the concluding section of the chapter.

In chapter 5, we begin our numerical analysis of the spin-1 BEC. First, we investigate the qualitative behavior of the system following a parameter quench from the polar phase to the easy-plane phase by discussing single truncated Wigner realizations. Next, we discuss the self-similar scaling dynamics of the transverse spin correlation function, also known as the structure factor. We carry on to characterize the topology of the setup and find signs of instantonic excitations in the system. To gather some more intuition as to the effect of instantons in the system, we investigate the dynamics of an initial condition with all spins pointing in the $F_x = 1$ direction. Using our newly won intuition, we localize instantons in the BEC with a plaqutte algorithm. We study the quantitative behavior of the instantons in the system in the context of scaling, and propose a connection to a sine-Gordon-like model. Thereafter, we inspect a setup motivated by recent experimental results by the research group of Prof. Dr. Markus Oberthaler [10, 14]. The experiments involve the investigation of far-from-equilibrium dynamics of a cloud of ^{87}Rb atoms confined in a thin cylinder shaped trap. The initial condition of the gas was imprinted with defects in the polar phase by means of local rotations in spin space and subsequently quenched to the easy-plane. We numerically study the dynamics of the system with written-in defects in the wave-function and observe the space-time evolution of the system. We probe its scaling dynamics and give an argument as to the difficulties of topological arguments in the one-dimensional case.

Finally, in chapter 6, we will discuss our results in the context of the experiment. We will attempt to give an argument as to the mismatch of results by means of inspecting the dimensionality of the system. We perform a fully three-dimensional simulation of a quasi-one-dimensional thin cylinder trap with parameters corresponding to that of the experiment. We find that the dynamics of the system were not altered substantially from the pure one-dimensional case, but that a few caveats in this description may cause us to doubt the validity of such simulations. A further explanation for discrepancies could be given by experimental limitations which give rise to uncertainties in the value of the quadratic Zeeman effect after the quench q_f. We thus inspect the dependency of the scaling behavior on the value of q_f. We find that for lower values of q_f, we obtain larger scaling exponents, whereas for larger q_f, we find a significantly slower scaling behavior for an initial condition imprinted with defects.

2. The Spin-1 Bose Gas

In our study of non-equilibrium dynamics in quantum many-body systems, we shall take a spinor Bose-Einstein condensate (BEC) as the system of interest of this thesis. In this chapter, we aim to introduce the main building blocks of the theory of the spinor BEC and it shall pose as a basis for all subsequent analysis. We base our introduction to the topic of spin-1 BECs on the works of [15, 5, 16]. The spinor BEC is a Bose-condensed cloud of atoms of mass M and a total spin F, including the magnetic sub-levels $m_f = -F, -F+1, ..., F$. In our case, we concentrate on a spin-1 BEC, such that we set $F = 1$, which in turn implies $m_f = -1, 0, 1$. The appearance of additional degrees of freedom due to the different spin configurations of the gas leads to several interesting dynamical phenomena, such as spin changing collisions [17], which give rise to the formation of structures in the condensate and the resulting domain coarsening dynamics [4, 18] which will become the main topic of discussion in the course of this thesis.

As mentioned in the introduction, the discussion in this thesis is motivated by the close cooperation with the research group led by Prof. Dr. Markus Oberthaler and their recent experiments with a cylinder-shaped BEC of ^{87}Rb atoms in the $F = 1$ manifold. Together, we probe the far-from-equilibrium dynamics of such a condensate in order to gain a better understanding of the underlying physics of this setup. Should the reader be interested, an overview of the experimental setup and a few interesting results over the past few years can be found in references [19, 7, 3, 10].

2.1 The Spin-1 Hamiltonian

We begin by defining the mathematical object describing the spin-1 BEC which is a 3 component quantum spinor operator

$$\hat{\boldsymbol{\Psi}}(\boldsymbol{x}, t) = \begin{pmatrix} \hat{\Psi}_{-1}(\boldsymbol{x}, t) \\ \hat{\Psi}_{0}(\boldsymbol{x}, t) \\ \hat{\Psi}_{1}(\boldsymbol{x}, t) \end{pmatrix}, \tag{2.1}$$

where each individual field is a bosonic field operator corresponding to the respective magnetic sub-level. Each bosonic field operator must satisfy the canonical commutation relations

$$\left[\hat{\Psi}_i(\boldsymbol{x},t),\hat{\Psi}_j(\boldsymbol{y},t)\right]=\left[\hat{\Psi}_i^\dagger(\boldsymbol{x},t),\hat{\Psi}_j^\dagger(\boldsymbol{y},t)\right]=0 \tag{2.2}$$

$$\left[\hat{\Psi}_i(\boldsymbol{x},t),\hat{\Psi}_j^\dagger(\boldsymbol{y},t)\right]=\delta_{ij}\,\delta(\boldsymbol{x}-\boldsymbol{y}), \tag{2.3}$$

where δ_{ij} is the Kroneckar delta symbol and $\delta(x)$ is the dirac delta function. Considering the possible interactions of the system, one obtains the Hamiltonian of the spin-1 BEC as follows

$$\begin{aligned}\hat{H}=\int \mathrm{d}\boldsymbol{x}\left\{\hat{\boldsymbol{\Psi}}^\dagger(\boldsymbol{x},t)\left[-\frac{\hbar^2}{2M}\nabla^2+V(\boldsymbol{x})+qf_z^2\right]\hat{\boldsymbol{\Psi}}(\boldsymbol{x},t)\right. \\ \left.+\frac{1}{2}c_0:\hat{n}^2(\boldsymbol{x},t):+\frac{1}{2}c_1:\hat{\boldsymbol{F}}^2(\boldsymbol{x},t):\right\},\end{aligned} \tag{2.4}$$

with the number density operator

$$\hat{n}(\boldsymbol{x},t)=\hat{\boldsymbol{\Psi}}^\dagger(\boldsymbol{x},t)\hat{\boldsymbol{\Psi}}(\boldsymbol{x},t) \tag{2.5}$$

and the spin density operator

$$\hat{\boldsymbol{F}}=\hat{\boldsymbol{\Psi}}^\dagger(\boldsymbol{x},t)\cdot\boldsymbol{f}\cdot\hat{\boldsymbol{\Psi}}(\boldsymbol{x},t), \tag{2.6}$$

where the vector $\boldsymbol{f}=(f_x,f_y,f_z)$ contains the three spin-1 matrices. The latter are the generators of $SU(2)$ in their three-dimensional irreducible representation:

$$f_x=\frac{1}{\sqrt{2}}\begin{pmatrix}0&1&0\\1&0&1\\0&1&0\end{pmatrix},\qquad f_y=\frac{i}{\sqrt{2}}\begin{pmatrix}0&-1&0\\1&0&-1\\0&1&0\end{pmatrix},\qquad f_z=\begin{pmatrix}1&0&0\\0&0&0\\0&0&-1\end{pmatrix}. \tag{2.7}$$

Lastly, the operator :: denotes normal ordering. A few explanations regarding the structure of the Hamiltonian and its terms are in order. We begin by viewing the quadratic terms in the fundamental fields. The first term describes the kinetic part of the Hamiltonian, where $\hbar$ denotes the reduced Planck constant, ∇ defines the gradient, and M is the mass of the particle. The term $V(x)$ is the contribution from an external trapping potential and the last term introduces the quadratic Zeeman effect to the energy of our system. The strength of this effect is characterized by the coupling strength q which will cause the energy levels of our splitted 3-level system to be shifted towards the same direction, according to the value of q. This will affect the nature of the ground-state of the system, as occupation of the different magnetic sub-levels and their associated energy eigenstates will favored or suppressed as a consequence of changing the value of q. This will be further elaborated in section 2.2.2. Furthermore, we remark that the main mechanism in this thesis to probe dynamics far from equilibrium will be to suddenly change the value of q, also known as a parameter quench. This will brings the system through a quantum phase transition (QPT) and thus drive it out of thermal equilibrium. It is also worthy to note that a certain term was omitted from the Hamiltonian: the linear Zeeman effect, which contributes a term of $\hat{\mathbf{\Psi}}^{\dagger}(\boldsymbol{x},t)pf_z\hat{\mathbf{\Psi}}(\boldsymbol{x},t)$. This term can be eliminated from our considerations by going into the rotating frame of reference w.r.t the Larmor precession caused by the linear Zeeman effect.

The next terms we must consider are the two density operators. The density-density interactions of the system are given by $\hat{n}^2$ with a coupling strength c_0. Similarly, the term proportional to c_1 describes the spin-spin interactions of the system with a strength given by the value of c_1. In the theory of dilute ultra-cold Bose gases one considers low-energy scattering processes, leading us to only examine s-wave scattering processes which restrict the possible contributions to the coupling constants $c_{0,1}$. In our case we regard a two-body contact interaction potential $V_F(\boldsymbol{x},\boldsymbol{y}) = g_F\delta(\boldsymbol{x}-\boldsymbol{y})$ with the interaction strength

$$g_F = \frac{4\pi\hbar^2}{M}a_F, \tag{2.8}$$

where a_F denotes the s-wave scattering length of the spin-F scattering channel. Due to parity arguments of the wave function and the restriction of our considerations to interactions which do not change the overall spin, we can only allow interactions with even total spin [17]. Thus, we can calculate the density-density and spin-spin interactions and find

$$c_0 = \frac{g_0+2g_2}{3}, \qquad c_1 = \frac{g_2-g_0}{3}. \tag{2.9}$$

The value of c_0 and c_1 is an inherent property of the atoms we consider. In this thesis we are considering interaction regimes which resemble the experimentally used ^{87}Rb atoms. Therefore, we consider only $c_1 < 0$ and $|c_1| \ll |c_0|$ as seen in Table 4 of Ref. [15].

2.1.1 Symmetries of the Spin-1 Hamiltonian

In the course of our discussion, we will focus on topology arguments and classification of defects in the system to gain a deeper understanding of the dynamics of the condensate far from equilibrium. Dealing with such (quasi) topological defects requires us to examine the symmetries of our system more carefully. The classification of the symmetry groups, under which the Hamiltonian or the ground state remain invariant, is of utmost importance for the characterization of the topological objects occupying our system. This classification could help us identify the mechanisms which drive the system to coarsen and its associated universality class [13].

We begin by considering the isotropic case, where we do not have any contribution from the quadratic or linear Zeeman effect. We set $q = 0$ and see that the Hamiltonian itself is invariant under a global $U(1)$ gauge transformation and $SO(3)$ rotations in spin space. Therefore, the symmetry group of the spinor BEC Hamiltonian reads

$$G = SO(3)_f \times U(1)_\phi, \tag{2.10}$$

where the subscript f denotes spin space and ϕ the wave function. In most of our discussions though, the quadratic Zeeman effect would have a non-zero value. This will break the $SO(3)$ symmetry of the Hamiltonian and the symmetry group would change to

$$G' = (D_\infty)_{f_z} \times U(1)_\phi, \tag{2.11}$$

where $D_\infty = SO(2) \rtimes \mathbb{Z}_2$ with the $\mathbb{Z}_2$ symmetry referring to rotations about the $x - y$ plane by an angle of π. For now we will postpone further discussion of this topic to section 3.5, where we will deal with these symmetry groups, the order parameter manifold and its resulting topological properties.

2.2 Mean-Field Description

2.2.1 The Spin-1 GPEs

After having discussed the Hamiltonian of the system, we may begin with calculating the equations of motion (EOM) and the resulting dynamics given some initial condition. Yet the problem arises that the full quantum dynamics of the system is extremely difficult to calculate and one must resort to employing approximations to ease calculations. Our goal is to be able to perform semi-classical calculations of the so called Gross-Pitaevski Equations (GPEs) by integrating a classical equation of motion provided with sampled quantum noise. In this section, we introduce the classical EOM by employing the mean-field description: replacing the full quantum operator $\hat{\mathbf{\Psi}}(\boldsymbol{x}, t)$ with its field expectation value

$$\boldsymbol{\psi}(\boldsymbol{x}, t) = \left\langle \hat{\mathbf{\Psi}}(\boldsymbol{x}, t) \right\rangle . \tag{2.12}$$

By definition, $\boldsymbol{\psi}(\boldsymbol{x}, t)$ is a three-component complex function of time and space. The mean-field description is only valid under some assumptions which have to be taken into account during simulations: We have to ensure a large enough atom number, keep the interactions between them weak and make sure that the temperature is low [20]. The latter is of no concern to us, since we simulate a zero temperature setting. This may only play a role in the comparison with experimental setups. Furthermore, we note that in the mean-field low-energy theory of quantum many-body systems, one makes use of the following representation for the components of the mean-field configuration

$$\psi_m = \sqrt{\rho_m} e^{i\theta_m}, \quad \text{with } m \in \{-1, 0, 1\}. \tag{2.13}$$

We denote ρ_m as the density of the m-th component and θ_m as its complex phase. As we shall see in chapters 5 and 6, the phases of the wave-functions are an important degree of freedom for the dynamics of the system.

We plug Eq. (2.12) into the Hamiltonian (2.4) and obtain the following energy functional

$$E[\boldsymbol{\psi}] = \int \mathrm{d}\boldsymbol{x} \left\{ \boldsymbol{\psi}^*(\boldsymbol{x},t) \left[-\frac{\hbar}{2M}\nabla^2 + V(\boldsymbol{x}) + q f_z^2 \right] \boldsymbol{\psi}(\boldsymbol{x},t) + \frac{1}{2} c_0 n^2(\boldsymbol{x},t) + \frac{1}{2} c_1 \boldsymbol{F}^2(\boldsymbol{x},t) \right\}, \tag{2.14}$$

where the definitions of the operators $n(\boldsymbol{x},t)$ and $\boldsymbol{F}(\boldsymbol{x},t)$ are analogous to Eq. (2.5) and (2.6) respectively, but with the quantum operators replaced with the complex function $\boldsymbol{\psi}(\boldsymbol{x},t)$. This description, ignoring quantum fluctuations, allows us to define the local spin densities of the system as follows

$$F_x = \frac{1}{\sqrt{2}} \left[\psi_0^*(\psi_1 + \psi_{-1}) + \text{c.c.} \right], \tag{2.15}$$

$$F_y = \frac{i}{\sqrt{2}} \left[\psi_0^*(\psi_1 - \psi_{-1}) + \text{c.c.} \right], \tag{2.16}$$

$$F_z = |\psi_1|^2 - |\psi_{-1}|^2, \tag{2.17}$$

where c.c. stands for the complex conjugate. We see that an interplay between the different magnetic sub-levels is responsible for the orientation of local spins. Especially the spin in the z direction is determined by the difference of the densities of the $m_f = \pm 1$ levels alone. We will also suggestively define a further spin component, which we will call the transverse spin as

$$F_\perp = F_x + iF_y = \sqrt{2}\left(\psi_1^*\psi_0 + \psi_0^*\psi_{-1}\right). \tag{2.18}$$

Per definition the transverse spin is a complex function and may be written in a density-phase representation [4] with

$$F_\perp = |F_\perp| e^{i\varphi_L}, \tag{2.19}$$

where $|F_\perp|$ describes the spin length and φ_L is known as the Larmor phase and is defined as

$$\varphi_L \propto \theta_1 - \theta_{-1}. \tag{2.20}$$

In the course of this thesis, Eq. (2.19) and (2.20) will be the main interest and degree of freedom which we will consider. To understand why this is so, we will discuss the mean-field phase diagram in section 2.2.2.

After deriving the mean-field energy functional, we may turn to calculating the classical equations of motion for our Bose fields, also known as the Gross-Pitaevskii equations. These are obtained by utilizing the variational principle

$$i\hbar\partial_t\psi_m(\boldsymbol{x},t) = \frac{\delta E}{\delta\psi_m^*}. \tag{2.21}$$

Applying this to Eq. (2.14) yields the coupled GPEs for the spin-1 BEC

$$i\hbar\partial_t\boldsymbol{\psi}(\boldsymbol{x},t) = \left[-\frac{\hbar^2}{2M}\nabla^2 + V(\boldsymbol{x}) + qf_z^2(\boldsymbol{x},t) + \frac{1}{2}c_0 n(\boldsymbol{x},t) + \frac{1}{2}c_1\boldsymbol{F}(\boldsymbol{x},t)\cdot\boldsymbol{f}\right]\boldsymbol{\psi}(\boldsymbol{x},t). \tag{2.22}$$

As mentioned above, these are the classical equations of motion for the mean-field configuration of the condensate. Solving these equations does not encapsulate the full quantum dynamics of the BEC and in order to recover the quantum nature of the system, we have to result to the truncated Wigner approximation (TWA), which will be thoroughly discussed in section 4.2.

2.2.2 Mean Field Phase Diagram

After deriving the equations of motion, we might ask ourselves which configurations of our three-component spinor are possible? We notice in the energy functional (2.14) that the coupling strengths of the $U(3)$ symmetry breaking terms, given by q and c_1 respectively, pose as energy scales which compete with each other to determine the favored spin configuration of the spinor. In other words, the favored occupation of the components, and with it the ground state, is determined by these contesting energy scales [5]. This leads to a phase diagram in the $q - c_1$ plane which gives rise to four qualitatively different ground states of the system on the mean-field level.

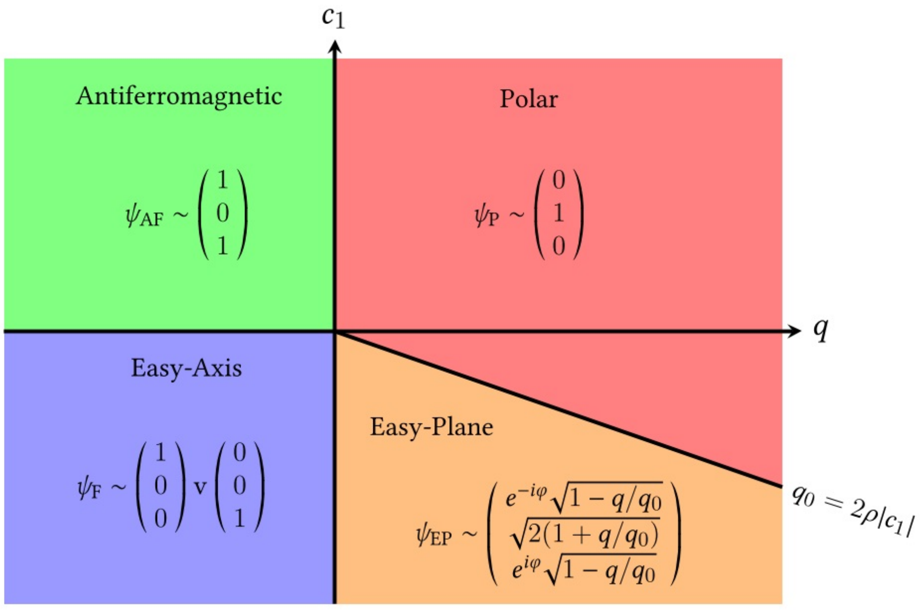

Figure 2.1: Mean-field phase diagram in the $q - c_1$ plane. Figure taken from [5].

By minimizing the energy functional (2.14) in the absence of a trapping potential, known as the homogeneous case, we obtain different ground states, according to the sign and amplitude of the parameters q and c_1. These ground states are the known phases of the spin-1 BEC and knowledge of their limits helps us prepare a system in an extreme out-of-equilibrium initial condition to probe its time evolution [4, 5, 7]. Fig. 2.1 shows the different phases and their respective ground states. We shall now elaborate further on each ground state:

Anti-Ferromagnetic Phase

For $c_1 > 0$ and $q < 0$ we find our condensate in the so-called antiferromagnetic phase. This state of the BEC is characterized by a complete symmetric occupation of the $m_f = \pm 1$ modes, thus leading to a vanishing total magnetization $\langle |F| \rangle = 0$. The spinor takes the form

$$\psi_{AF} = \sqrt{\rho} \begin{pmatrix} e^{i\theta_1} \\ 0 \\ e^{i\theta_{-1}} \end{pmatrix}, \tag{2.23}$$

where ρ is the homogeneous total density of the condensate.

Polar Phase

For anti-ferromagnetic interactions, i.e. $c_1 > 0$, and positive q the system takes on the polar ground state. This state is characterized by a vanishing total magnetization $\langle |F| \rangle = 0$ and an occupation of the $m_f = 0$ component alone. The spinor takes the form

$$\psi_P = e^{i\phi} \sqrt{\rho} \begin{pmatrix} 0 \\ 1 \\ 0 \end{pmatrix}, \tag{2.24}$$

where ϕ is the global $U(1)$ phase of the system as discussed in section 2.1.1. Notice that also for ferromagnetic interactions $c_1 < 0$ we may still be in the polar phase for a range of values of $q > 2\rho|c_1|$. An intricate interplay between the energy scales brings the system to either energetically prefer a vanishing magnetization or to acquire a finite orientated magnetization.

Easy-plane

For $c_1 < 0$ and $q = 2n|c_1| =: \tilde{q}$, the system exhibits a QPT from the polar phase to easy-plane phase, breaking the full spin symmetry of the ground state [21]. Thus, for $0 < q < \tilde{q}$ the condensate finds itself in the easy-plane phase. The easy-plane is characterized by symmetric occupations of the $m_f = \pm 1$ modes with a relative phase and a finite occupation of the $m_f = 0$

mode. The ground state reads

$$\psi_{EP} = \sqrt{\rho}\frac{e^{i\phi}}{2}\begin{pmatrix} e^{-i\varphi}\sqrt{1-q/\tilde{q}} \\ \sqrt{2(1+q/\tilde{q})} \\ e^{i\varphi}\sqrt{1-q/\tilde{q}} \end{pmatrix}. \tag{2.25}$$

As the name easy-plane suggests, the dynamics of the system is restricted to the $F_x - F_y$ plane, whereas the system exhibits no magnetization in the F_z direction. Thus, the order parameter of the system in the context of phase transitions will be the transverse spin $F_\perp$ as defined in Eq. 2.19. With the definition given in Eq. 2.25 we find the transverse spin length to be dependent on q and it reads

$$|F_\perp|/\rho = \left(1 - (q/\tilde{q})^2\right)^{1/2}. \tag{2.26}$$

Easy-Axis Phase

Lastly, should we now tune our ferromagnetic interacting system, i.e. $c_1 < 0$, to a $q < 0$ we obtain the ferromagnetic phase, where the system shows a broken $\mathbb{Z}_2$ symmetry w.r.t the magnetization in F_z direction. This leads to an arbitrarily chosen ground state which is fully magnetized in the $F_z = \pm 1$ direction. The spinor thus reads

$$\psi_F = e^{i\phi}\sqrt{\rho}\begin{pmatrix} 1 \\ 0 \\ 0 \end{pmatrix}, \quad \text{or} \quad \psi_F = e^{i\phi}\sqrt{\rho}\begin{pmatrix} 0 \\ 0 \\ 1 \end{pmatrix}. \tag{2.27}$$

The main interest of this thesis is the rapid change in the quadratic Zeeman effect to create an initial state far from equilibrium, by forcing the system through the QPT from the polar to the easy-plane phase. This is the main mechanism, by which we probe the dynamics of the system in an out-of-equilibrium setting.

2.2.3 One-Dimensional Description

The physical system which we study in this thesis is a one-dimensional BEC, as motivated by the quasi-one-dimensional setting investigated in the aforementioned experiment. Therefore, we must adjust our theory slightly to incorporate an effective one-dimensional description of the system. As mentioned before, the experimental setting which we aim to simulate and investigate makes use of a highly anisotropic harmonic trap, with an additional laser to create potential barriers in the longitudinal direction, thus creating a very thin cylinder shaped condensate, which we can consider as quasi-one-dimensional [3, 10]. In order to be able to truly consider the system as one-dimensional, we must assure that the energy scales set by the harmonic confinement overpower all other relevant energy scales in the system. This implies that the length scales set by the trap in the transverse direction are small enough w.r.t the length scales set by the condensate.

The harmonic trapping of the BEC translates to an external harmonic potential in the Hamiltonian

$$V(\boldsymbol{x}) = \frac{1}{2}\omega_\perp^2 r^2 + \frac{1}{2}\omega_\parallel^2 x^2, \tag{2.28}$$

where $r = y^2 + z^2$, and $\omega_{\perp,\parallel}$ are the harmonic trap frequencies in the transverse or longitudinal direction respectively. According to [22], in order to consider the system kinematically one-dimensional in a zero temperature setting, we must demand

$$\hbar\omega_\perp \gg \rho|c_0|, \rho|c_1|. \tag{2.29}$$

Another way of looking at Eq. (2.29) is by utilizing length scales. Quantum many-body systems such as the spin-1 BEC exhibit two main length scales governing the dynamics in the systems. These are referred to as the density healing length ξ and the spin healing length ξ_s and they are given by

$$\xi = \frac{\hbar}{\sqrt{2M\rho c_0}}, \qquad \xi_s = \frac{\hbar}{\sqrt{2M\rho|c_1|}}. \tag{2.30}$$

The name healing length already suggests the main context of these length scales: they give us a characteristic length by which the BEC recovers its mean density from a local defect in the component densities or spin densities respectively. Such defects may include various kinds of solitons, which will be introduced in chapter 3. If the extent of the system in the transverse direction is much smaller than these length scales, we can assume that no significant dynamical phenomena play a role in those degrees of freedom and we may consider the dynamics in the transverse direction frozen. Thus, we can formulate a more intuitive, yet equivalent, criterion for the reduction of dimensionality: A harmonic potential in the transverse directions also sets a characteristic length, known as the oscillator length

$$a_\perp = \sqrt{\frac{\hbar}{M\omega_\perp}}. \tag{2.31}$$

$a_\perp$ gives a characteristic extent of the trap depending on its harmonic frequency. We must hence demand

$$a_\perp \ll \xi, \xi_s, \tag{2.32}$$

i.e. that the extent of the trap in the transverse direction is much smaller than the characteristic length scales of the system. By further demanding that the longitudinal trap frequency $\omega_\parallel$ is much smaller than the transverse trap frequency $\omega_\perp$, we achieve an elongated trap geometry. This allows us to make an ansatz, in which we separate the wave functions ψ_m into a transverse and longitudinal part. The transverse wave function would correspond to the ground state of the harmonic oscillator and can be thus integrated out. This results with modified GPEs with modified density-density and spin-spin couplings. We find the one-dimensional mean-field equations of motion to be

$$
\begin{aligned}
i\hbar\partial_t\psi_{\pm 1} &= H_0\psi_{\pm 1} + q\psi_{\pm 1} + c_1^{1D}\left(|\psi_{\pm 1}|^2 + |\psi_0|^2 - |\psi_{\mp 1}|\right)\psi_{\pm 1} + c_1^{1D}\psi_0^2\psi_{\mp 1}^* && (2.33)\\
i\hbar\partial_t\psi_0 &= H_0\psi_0 + c_1^{1D}\left(|\psi_1|^2 + |\psi_{-1}|^2\right)\psi_0 + 2c_1^{1D}\psi_{-1}\psi_0^*\psi_1, && (2.34)
\end{aligned}
$$

where we define the spin - independent part of the Hamiltonian as

$$
H_0 = -\frac{\hbar^2}{2M}\partial_x^2 + V(x) + c_0^{1D}n'(x), \tag{2.35}
$$

where $n'(x) = \sum_{i=-1}^{1}|\psi_i|^2$ is the total density and the effective one-dimensional couplings are given by

$$
c_{0,1}^{1D} = \frac{c_{0,1}}{2\pi a_\perp^2}. \tag{2.36}
$$

In Eq. (2.35), we have left the potential form in the x direction to be arbitrary. In reality, it will be a sum of an harmonic trap and a box potential in longitudinal direction, reflecting the cylindrical geometry of this setting.

2.3 Dynamical Instabilities

As discussed in section 2.2.2, a parameter quench, e.g., from the polar phase to the easy-plane phase, forces the system through a QPT. To describe the dynamics of the system after such a phase transition we must go beyond the mean-field level and introduce small quantum fluctuations to the classical field. This would in turn introduce instabilities in the system, which are described by the unstable Bogoliubov modes[23, 21]. Bogoliubov theory gives us a tool to study excitations on the mean-field ground state to a certain degree, where the fluctuations remain small [4]. Thus, the theory is expected to be valid for a short time period of the evolution until the underlying assumption of small fluctuations breaks down.

2.3.1 Bogoliubov Theory

We begin by outlining the Bogoliubov theory for the spin 1 BEC in the polar phase in the absence of a trapping potential, and then discuss the formation of instabilities after a parameter quench into the easy-plane, by considering the quasiparticle excitations and their respective energy spectrum. This discussion follows the works of [15, 21] and only gives a rough outline of the derivation of the Bogoliubov spectrum. For a detailed table of the possible Bogoliubov spectrum of each spin-1 BEC phase see Ref. [5]. The first step is to perform a wave expansion of the respective wave functions, since momentum space will prove most advantageous. We write

$$\hat{\psi}_m = \frac{1}{\sqrt{\Omega}} \sum_{\boldsymbol{k}} \hat{a}_{\boldsymbol{k},m} e^{i\boldsymbol{k}\boldsymbol{x}}, \tag{2.37}$$

where Ω denotes the volume of the system and the coefficients $\hat{a}_{\boldsymbol{k},m}$ are the bosonic annihilation operators of the m-th magnetic sub-level with wave vector $\boldsymbol{k}$. Next, as explained in [16], we assume that the $\boldsymbol{k} = \boldsymbol{0}$ mode is macroscopically occupied, which allows us to exchange the operator $\hat{a}^{\dagger}_{\boldsymbol{0},m}$ with a complex number. This is done by considering that the zero-momentum mode of the ground state of the Bose gas $|\Phi_0\rangle$ is described by a coherent state.

$$\hat{a}_{\boldsymbol{0},m} |\Phi_0\rangle = \sqrt{N_0}\, |\Phi_0\rangle\,. \tag{2.38}$$

Thus, we can write the fixed total number of atoms in the system N as

$$N_0 + \sum_{\boldsymbol{k}\neq 0} \sum_{m} \hat{a}^{\dagger}_{\boldsymbol{k},m} \hat{a}_{\boldsymbol{k},m} = N. \tag{2.39}$$

Therefore, we assume the occupation of the modes with $\boldsymbol{k} \neq 0$ are very small. This allows us to insert the wave expansion (2.37) into the Hamiltonian (2.4) and neglect terms which are higher than second order in $\hat{a}^{\dagger}_{\boldsymbol{k},m}$. This is to say that fluctuations in the occupation number of the zeroth mode are small. The next step constitutes a convenient way of splitting the relevant fluctuations. We define a new set of operators $\hat{a}_{\boldsymbol{k},f_x}$ and $\hat{a}_{\boldsymbol{k},f_y}$ as the fluctuations in the transverse spin direction. These operators are given by

$$\hat{a}_{\boldsymbol{k},f_x} = \frac{1}{\sqrt{2}} \left(\hat{a}_{\boldsymbol{k},1} + \hat{a}_{\boldsymbol{k},-1}\right), \quad \hat{a}_{\boldsymbol{k},f_y} = \frac{1}{\sqrt{2}} \left(\hat{a}_{\boldsymbol{k},1} - \hat{a}_{\boldsymbol{k},-1}\right). \tag{2.40}$$

Hence, we obtain the expanded Hamiltonian up to second order the annihilation and creation operators:

$$\begin{aligned}\hat{H}^{(2)} = \frac{\Omega n^2 c_0}{2} &+ \sum_{\boldsymbol{k}\neq 0} \Bigg[(\epsilon_k + nc_0) \hat{a}^{\dagger}_{\boldsymbol{k},0} \hat{a}_{\boldsymbol{k},0} + \frac{nc_0}{2} \left(\hat{a}^{\dagger}_{\boldsymbol{k},0} \hat{a}^{\dagger}_{-\boldsymbol{k},1} + \hat{a}_{\boldsymbol{k},0} \hat{a}_{-\boldsymbol{k},0} \right) \\ &+ \sum_{f=f_x,f_y} \left\{ (\epsilon_k + q + nc_1) \hat{a}^{\dagger}_{\boldsymbol{k},f} \hat{a}_{\boldsymbol{k},f} + \frac{nc_1}{2} \left(\hat{a^{\dagger}}_{\boldsymbol{k},f} \hat{a}_{-\boldsymbol{k},f} + \hat{a}_{\boldsymbol{k},f} \hat{a}_{-\boldsymbol{k},f} \right) \right\} \Bigg],\end{aligned} \tag{2.41}$$

where $\epsilon_k = \hbar^2 k^2 / 2M$ and $n = N/\Omega$ is the homogeneous density. The obtained Hamiltonian can now be diagonlized in momentum space by means of a Bogoliubov transformation, defining new quasi-particle annihilation and creation operators as

$$\hat{b}_{\boldsymbol{k},0} = \sqrt{\frac{\epsilon_k + nc_0 + \omega_{\boldsymbol{k},0}}{2\omega_{\boldsymbol{k},0}}}\hat{a}_{\boldsymbol{k},0} + \sqrt{\frac{\epsilon_k + nc_0 - \omega_{\boldsymbol{k},0}}{2\omega_{\boldsymbol{k},0}}}\hat{a}^\dagger_{-\boldsymbol{k},0} \tag{2.42}$$

$$\hat{b}_{\boldsymbol{k},f} = \sqrt{\frac{\epsilon_k + q + nc_1 + \omega_{\boldsymbol{k},f}}{2\omega_{\boldsymbol{k},f}}}\hat{a}_{\boldsymbol{k},0} + \sqrt{\frac{\epsilon_k + nc_1 - \omega_{\boldsymbol{k},f}}{2\omega_{\boldsymbol{k},f}}}\hat{a}^\dagger_{-\boldsymbol{k},f}, \tag{2.43}$$

where we have already made use of the energy eigenvalues $\omega_{\boldsymbol{k},0}$ and $\omega_{\boldsymbol{k},f}$ that we obtain in the diagonalized Hamiltonian

$$\hat{H}^{(2)} = E_0 + \sum_{\boldsymbol{k}\neq 0}\left[\omega_{\boldsymbol{k},0}\hat{b}^\dagger_{\boldsymbol{k},0}\hat{b}_{\boldsymbol{k},0} + \omega_{\boldsymbol{k},f}\left(\hat{b}^\dagger_{\boldsymbol{k},f_x}\hat{b}_{\boldsymbol{k},f_x} + \hat{b}^\dagger_{\boldsymbol{k},f_y}\hat{b}_{\boldsymbol{k},f_y}\right)\right], \tag{2.44}$$

with

$$\omega_{\boldsymbol{k},0} = \sqrt{\epsilon_{\boldsymbol{k}}(\epsilon_{\boldsymbol{k}} + 2nc_0)} \tag{2.45}$$

$$\omega_{\boldsymbol{k},f} = \sqrt{(\epsilon_{\boldsymbol{k}} + q)(\epsilon_{\boldsymbol{k}} + q + 2nc_1)} \tag{2.46}$$

and E_0 is the ground state energy, which is regarded is a constant. The dynamical instabilities which may arise in the system are caused by imaginary energy eigenvalues, since time evolution of our quantum states evolve with $\propto e^{-i\omega_{k,0}t}$ or alternatively $\propto e^{-i\omega_{k,f}t}$. Should the energy eigenvalue of a certain mode turn imaginary, i.e. $\omega^2 < 0$, the time evolution of these modes will be given by an exponential growth function, these modes are thus considered as unstable modes at which the amplitude grows exponentially. In Eq. (2.45) we observe a gapless spectrum which remains stable and thus the density excitations do not give rise to any dynamical instabilities. In contrast, the transverse spin excitation spectrum (2.46) is gapped for $q \neq 0$ and for certain values of q w.r.t the critical value $2nc_1$ one can obtain unstable modes.

Consider now a quench from the polar phase to the easy-plane phase of the ferromagnetic spin-1 BEC. We recall that $c_1 < 0$ and we quench from $q_i > 2n|c_1|$ to $q_f < 2n|c_1|$. The ground state of the system changes suddenly, and the quasiparticle operators describing the unstable modes (Eq. (2.43)) are responsible for exciting particles in the $m_f = \pm 1$ components, thus causing an exponential increase in their populations. By calculating the Heisenberg equations of motion of the operators $\hat{a}_{\boldsymbol{k},\pm 1}$ and solving them, we can calculate the occupation number of the $m_f = \pm 1$ components $n_{\pm 1}(\boldsymbol{k}, t) = \left\langle \hat{a}^\dagger_{\boldsymbol{k},\pm 1}\hat{a}_{\boldsymbol{k},\pm 1}\right\rangle$ as a function of time. We consider a region of momentum space where the energy eigenvalues are negative and we substitute $\omega_{\boldsymbol{k},f} = i\hbar\gamma_{\boldsymbol{k}}$, where $\gamma_{\boldsymbol{k}}$ is referred to as the growth rate. With some algebra we obtain

$$n_{\pm1}(\boldsymbol{k},t) = \left[\cosh^2(\gamma_{\boldsymbol{k}}t) + \left(\frac{\epsilon_{\boldsymbol{k}} + q + nc_1}{\hbar\gamma_{\boldsymbol{k}}}\right)^2 \sinh^2(\gamma_{\boldsymbol{k}}t)\right] n_{\pm1}(\boldsymbol{k},0) \\ + \left(\frac{nc_1}{\hbar\gamma_{\boldsymbol{k}}}\right)^2 \sinh^2(\gamma_{\boldsymbol{k}}t)[n_{\mp1}(-\boldsymbol{k},0)+1]. \tag{2.47}$$

Eq. (2.47) shows us in its last term that even if the initial occupation of the $m_f = \pm1$ components was zero, their population would still increase exponentially with the growth rate $\gamma_{\boldsymbol{k}}$. In mean-field theory, we occupy a mode which is stable for all times. The appearance of instabilities in the system comes from introducing quantum fluctuations in all the momentum modes of the system, thus creating an initial seed for the instabilities. The unstable modes occupied by the quantum noise will be amplified exponentially and we shall observe non-trivial and rich dynamics in the system given at first by the Bogoliubov predictions up to a point, where fluctuations have grown too large and Bogoliubov theory can no longer hold [5, 4, 24]. Our theory up to this point in the discussion has only included classical EOM given by the mean-fied configuration. The introduction of quantum fluctuations to the system seems to be crucial to the formation of the dynamics in the system. Therefore, we must introduce such fluctuations to the classical EOM. How we do this will be discussed in section 4.2 as we introduce the theory behind the truncated Wigner approximation (TWA).

At this moment, it is worth noting that the dynamical instabilities which the system exhibits are not the sole point of interest in a system after a sudden parameter quench. Quenching the system through a QPT may cause the formation of topological defects in the condensate due to the Kibble-Zurek Mechanism (KZM) [25, 1]. In the case of our interest, we consider the breaking of the $SO(2)$ symmetry of the polar phase as we go over to the easy-plane. The aforementioned dynamical instabilities cause the population of the $m_f = \pm1$ modes to be exponentially occupied, which in turn give rise to finite transverse spin length. Though the length of the spin should be rather well-defined the orientation of the transverse spin, governed by the Larmor phase φ_L will be chosen spontaneously at each point of the condensate, reflecting the broken $SO(2)$ symmetry. As such spin domains evolve, topological objects may form as various values of the Larmor phase may not be able to adjust in a continuous way. Therefore, in a one-dimensional setting we expect the formation of kinks and anti kinks in the Larmor phase, which can be seen as solitonic excitations [4, 26]. The topic of topology will be discussed in the next chapter and its understanding will prove to be a major step in understanding the underlying physics in this far-from-equilibrium one-dimensional setting.

3. Topology

In the theory of phase ordering kinetics, the emergence of topological defects in the form of, e.g. domain walls between domains of opposite magnetization, is crucial to the derivation of scaling phenomena in a far-from-equilibrium setting [13, 27]. The topology of the system is given by symmetries set by the Hamiltonian, which lead to submanifolds where the quantum field can take its values. These submanifolds provide us with a notion of what kinds of topological objects may exist in the system. Their associated charges and currents give rise to conservation laws that affect the scaling behavior of the system. In the example of domain walls, such topological objects lead to the formation of length scales in the system, which may change with time as these objects collide, scatter and merge, sometimes causing an effective coarsening effect due to the magnetic domains growing larger with time [27]. Another relevant example is the XY model, where the governing length scale of the correlation functions is given by the mean distance between vortices. As the vortices of opposite winding numbers annihilate, the mean separation between these objects grows larger, as they grow more sparse, leading to a coarsening of the correlation functions in time [28]. Hence, considering the topology of our model is crucial to understanding what kind of objects live in the system, their energetics and their contribution to the time evolution of the system as hypothesized in [6, 4, 13]. The discussion of homotopy groups, solitons and the associated currents is based mainly on the works of [29, 30, 31] .

3.1 Homotopy Theory

First and foremost, we must understand how to characterize topological objects in the system. To do so, we must recall the mathematical concepts of homotopy groups. The homotopy groups describe what types of topological objects are allowed within a given order-parameter manifold and give us a tool to characterize these objects. For simplicity, we give some general expressions at first, yet we will subsequently concentrate on the theory relevant to us, which is one-dimensional. Let X and Y be two manifolds without boundary. Two maps $\Psi_1 : X \mapsto Y$,

$\Psi_2 : X \mapsto Y$ are called homotopic if there is a continuous map

$$\tilde{\Psi} : X \times [0,1] \mapsto Y, \tag{3.1}$$

with a time parameter τ in the interval $[0,1]$ such that $\tilde{\Psi}|_{\tau=0} = \Psi_1$ and $\tilde{\Psi}|_{\tau=1} = \Psi_2$. In other words, two maps are homotopic if the maps can be continuously deformed into each other. This relation between two maps is an equivalence relation, and thus a set of homotopic maps build an homotopy class. We now assume that the manifold X is the unit circle S^1, which is the manifold of the group $U(1)$ and $SO(2)$. We denote the set of homotopy classes of based maps $\Psi : S^1 \mapsto Y$ by $\pi_1(Y)$, also known as the fundamental homotopy group. This group has the identity element $S^1 \mapsto y_0$, where y_0 is some point on the manifold Y. If all sets of maps in $\pi_1(Y)$ are homotopic to the identity element ,also know as the trivial loop, then the group itself is trivial and is denoted by $\pi_1(Y) = 0$. If Y is simply connected then we can continuously contract all loops on the manifold to one point, the trivial loop. Physically such a construction will imply that topological objects of this sort are not protected by any conservation law and any such arrangement may be continuously deformed back to its constant ground state.

Now we specify Y to also be the unit circle S^1. One can show that the fundamental homotopy group is given by

$$\pi_1(S^1) = \mathbb{Z}, \tag{3.2}$$

where each homotopy class is characterized by one integer also known as a winding number. More intuitively speaking, we see that by circling S^1 once on the base manifold we encircle the target manifold S^1 an integer valued number of times. Finding homotopy groups with various base and target manifolds is a task mathematicians have set their mind to and much can be said about this interesting topic. For simplicity, we shall give the main point of interest for this thesis, which is the following statement:

$$\pi_n(S^m) \cong \begin{cases} \mathbb{Z} & \text{if} \quad m = n \geq 1 \\ 0 & \text{if} \quad m > n \geq 1, \end{cases} \tag{3.3}$$

as stated in [15]. To put it in a geometrical interpretation, we say that we cannot wrap an m sphere by going over an n sphere with $n < m$, since the target manifold is "too large". The case of $n > m$ is not trivial and should be investigated for each case by itself. for example there are non-trivial homotopy groups with such constructions such as $\pi_3(S^2) = \mathbb{Z}$. The concepts of the winding number and non-trivial homotopy groups seems rather abstract, but in the next section, we will connect these concepts to the physical objects which appear in the condensate.

3.2 Solitons

The term soliton referes to constant shaped wave packets in nonlinear dispersive media. The non-linear interactions of, e.g., our spin-1 BEC model, allow for the formation of such solitonic solutions which may propagate through the system with constant velocity, undergoing scattering events and display various interesting dynamical properties [32, 33]. In this section we give a brief review of how such solutions arise in the system and their classification by homotopy groups.

We begin by imposing a rather strong and physically sensible restriction to the solitons: they should have a finite total energy and their energy density decays rapidly as $r \to \infty$, where now r is the distance from the soliton origin. Let us consider an energy functional of the form

$$E = \int \mathrm{d}^d x \left[\frac{1}{2} (\nabla \phi)^2 + V(\phi) \right], \tag{3.4}$$

where $V(\phi)$ is some arbitrary potential. We know that the ground state of the system is found at $\min(V)$, which is a submanifold $\mathcal{V} \subset \mathbb{R}^n$. The constraint we have imposed on the fields implies that at spatial infinity the field must take its values in the vacuum submanifold $\mathcal{V}$. Therefore, a field configuration defines a map from the unit sphere at infinity of $\mathbb{R}^d$, which we will denote as S^{d-1}_∞, to the vacuum submanifold. No loss of information results from considering only this asymptotic data

$$\phi^\infty : S^{d-1}_\infty \mapsto \mathcal{V}. \tag{3.5}$$

The topological character of any configuration ϕ is determined by the homotopy class of $\phi^\infty \in \pi_{d-1}(\mathcal{V})$.

We observe that if $\mathcal{V}$ is only one point, we can speak of an unbroken symmetry phase in the vacuum. Thus, the homotopy class of such a configuration is the trivial one and we obtain no topological objects. Should $\mathcal{V} = S^{n-1}$ then we speak of spontaneously broken symmetries and the asymptotic field map is given by

$$\phi^\infty : S^{d-1}_\infty \mapsto S^{n-1}, \tag{3.6}$$

which in turn means that the fields are classified by elements of $\pi_{d-1}(S^{n-1})$. According to Eq. (3.3) this means we must demand $n \leq d$ in order to observe topological objects in the system.

The Relevant Example

To gain intuition as to the physical meaning of these configurations, it is instructive to consider the ϕ^4 kink solutions. The famous Mexican hat potential for a field $\boldsymbol{\phi} = (\phi_1, ..., \phi_n)$ is given by $V(\boldsymbol{\phi}) = (1 - \boldsymbol{\phi})^2$ which has the vacuum submanifold $\mathcal{V} = S^{n-1}$, i.e. the vacuum takes its values along S^{n-1} and each field value is chosen spontaneously along that surface (see Fig. 3.1). Therefore, the field configurations are topologically characterized by $\pi_{d-1}(S^{n-1})$, and a field with a given homotopy class given by an integer cannot be continuously deformed to another field configuration of a different class. To see this, we consider the simple case of ϕ^4 theory with a single component scalar field ϕ with a Lagrangian

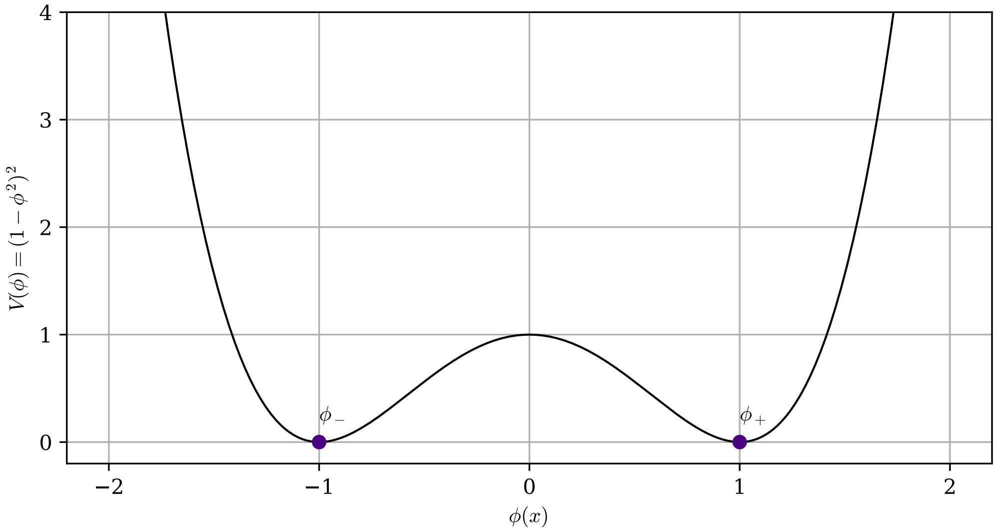

Figure 3.1: Mexican hat potential for a scalar field $\phi(x)$. The vacuum manifold has only two discrete values, as the scalar field takes its vacuum value at $\phi_\pm(x) = \pm 1$.

$$\mathcal{L} = \frac{1}{2}\partial_\mu\phi\,\partial^\mu\phi - (1 - \phi^2)^2. \tag{3.7}$$

The potential $V(\phi) = (1 - \phi^2)^2$ takes its minimum value for the field value of $\phi_\pm = \pm 1$. Thus, we see that we have $\mathcal{V} = S^0$ and

$$\phi^\infty : \{-\infty, \infty\} \mapsto S^0. \tag{3.8}$$

This brings us to the homotopy group $\pi_0(S^0) = \mathbb{Z}_2$. Let us now consider the field configuration where $\phi_\pm = \lim_{x\to\pm\infty} \phi(x)$. The occurrence of non-trivial topology requires two different vacua $\phi_\pm$, since if $\phi_+ = \phi_-$, each field configuration ϕ may be continuously transformed into the constant vacuum solution, which has vanishing energy. Should now $\phi_+ \neq \phi_-$, the field cannot be continuously deformed into a constant zero energy solution with any map which keeps the energy finite. The field configuration must thus interpolate between the two vacua, and is a stable configuration of the system, due to our constraint of finite energy.

In order to derive the form of the field, we must first introduce a lower bound of the energy of the field configuration, also known as the Bogomolny energy bound. Through a series of algebraic manipulations of the energy E we arrive at

$$E \geq \left| \int_{-\infty}^{\infty} \left(\frac{1}{2} (\partial_x \phi)^2 + V(\phi) \right) \mathrm{d}x \right| = \left| \int_{\phi_-}^{\phi_+} \sqrt{2V(\phi)\, \mathrm{d}\phi} \right|. \tag{3.9}$$

The lower bound is satisfied by considering a static solution, i.e. one where the kinetic energy vanishes. This leads us to a lower bound given by the topological data of the asymptotic information of the degenerate ground states. Satisfying the lower bound we may rewrite (3.9) to the so called first order Bogomolny equation

$$\partial_x \phi = \pm \sqrt{2V(\phi)} = (1 - \phi^2), \tag{3.10}$$

which has the solution

$$\phi(x) = \tanh(x - a), \tag{3.11}$$

where a is a free constant of integration determining the position of the soliton. By applying a Lorentz boost to the solution we obtain the propagating soliton solution

$$\phi(x, t) = \tanh \left(\gamma [x - vt - a] \right), \tag{3.12}$$

where v is the velocity, $\gamma = 1/\sqrt{1 - v^2}$ is the Lorentz factor and t denotes the time.

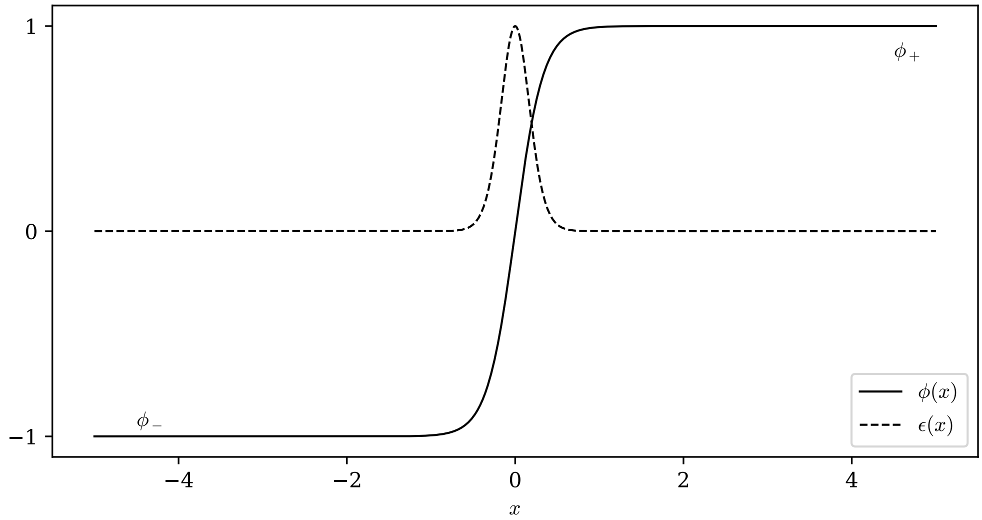

Figure 3.2: Solid curve shows the shape of the ϕ^4 kink soliton. The solution interpolates between the two degenerate vacua $\phi_\pm$. The dashed line shows the energy density ϵ of the soliton solution, showing the solution is strongly localized.

3.3 Topological Currents and Charges

The above discussed topological defects carry so-called topological currents and charges. These concepts help us calculate the homotopy class of an object, thus allowing us to further understand what object is dealt with and its interpretation in the system. According to [30], given a smooth n-component field $\boldsymbol{\phi} = (\phi^1, ..., \phi^n)$ on a d-dimensional space-time, then for $n \leq d$ we can define conserved quantities according to

$$\partial_{\mu_1}\left[\epsilon^{\mu_1...\mu_n...\mu_d}\epsilon_{\alpha_1...\alpha_n}\phi^{\alpha_1}\partial_{\mu_2}\phi^{\alpha_2}...\partial_{\mu_n}\phi^{\alpha_n}\right] = 0. \tag{3.13}$$

Hence, the term inside the brackets is conserved. For the case $n = d$ we define a conserved current

$$j^{\mu} = \frac{1}{(n-1)\Omega^{n-1}}\epsilon^{\mu\mu_2...\mu_n...\mu_d}\epsilon_{\alpha_1...\alpha_n}\phi^{\alpha_1}\partial_{\mu_2}\phi^{\alpha_2}...\partial_{\mu_n}\phi^{\alpha_n}, \tag{3.14}$$

where Ω^{n-1} is the surface area of a unit n-sphere. From this current, one can calculate a charge associated with this topological current as

$$Q = \int_{-\infty}^{\infty} \mathrm{d}x^{n-1}\, j^0. \tag{3.15}$$

Due to the boundary conditions which we have imposed on the fields regarding their values in spatial infinity, this charge number is necessarily an integer. The integer corresponds to the respective homotopy class given by the homotopy group of the configuration, thus giving us a tool to calculate the classes and types of topological objects in the system. Moreover, it allows us to probe if such objects even exist in the system. The value of Q is a constant of motion and should thus be a conserved quantity at all times. This is due to the fact that as we have previously discussed, one cannot continuously deform the field configuration corresponding to this homotopy class into another homotopy class, without having to invest an infinite amount of energy.

For the previous discussion of ϕ^4 kinks with a scalar field in $d = 1$ space-time one obtains

$$j = \frac{1}{2}\partial_x\phi \tag{3.16}$$

$$\implies Q = \frac{1}{2}\int_{-\infty}^{\infty} \mathrm{d}x\,\partial_x\phi = \frac{1}{2}(\phi(\infty) - \phi(-\infty)) = 1, \tag{3.17}$$

in case of a kink.

3.4 Instantons

In our previous discussion, we have seen that defects in the system may be associated with different homotopy groups, which classify the spatial defects of the system such as kinks in the ϕ^4 case. Their associated topological charges, or winding numbers, were of great importance. We shall now take upon ourselves to understand the concept of instantons. These objects can be interpreted as tunneling events between different vacua of the system in imaginary time [31]. The concept of instantons is best understood by considering a pure Yang-Mills quantum field theory.

Consider a pure gauge field

$$A_\mu = \frac{1}{i} U(\boldsymbol{x}) \partial_\mu U^\dagger(\boldsymbol{x}), \tag{3.18}$$

where $U(\boldsymbol{x})$ is the an element of the Lie group of interest. We impose a condition that the pure gauge $U(x)$ reaches a constant value at spatial infinity to compactify the configuration space, allowing us to consider the gauge transformations as maps between spheres, as we have previously considered. The Yang-Mills Lagrangian density reads

$$\mathcal{L}_{YM} = \frac{1}{4} F^a_{\mu\nu} F^a_{\mu\nu} \tag{3.19}$$

where $F^a_{\mu\nu} = \partial_\mu A^a_\nu - \partial_\nu A^a_\mu$ is the so called field strength tensor corresponding to the color index a. To further understand the intuitive meaning of the toplogical objects in this arrangement, we must turn to the mathematical treatment of instantons, which is best made in imaginary time. This is done by performing an analytic continuation, also known as a Wick rotation

$$t \rightarrow -it = \tau, \qquad A_0 \rightarrow -iA_0. \tag{3.20}$$

We thus obtain the Euclidean Yang-Mills action as

$$S_E = \frac{1}{4} \int \mathrm{d}^d x F^a_{\mu\nu} F^a_{\mu\nu}. \tag{3.21}$$

The pure gauge fields defined in Eq. (3.18) minimize the energy and thus pose as "classical vacua", since they minimize the Yang-Mills Euclidean action as well. The next step is to recall that for a given field, we may define a winding number of the system Q_w using the construction given in Eq. (3.14) and (3.15). The pure gauge fields that accommodate such winding numbers are constructed from gauge transformations $U_n(\boldsymbol{x})$ which give rise to well-defined winding numbers $Q_w = n$, for example:

$$U_n(\boldsymbol{x}) = \exp\left[i\pi n \frac{\boldsymbol{x}}{|\boldsymbol{x}|} \boldsymbol{\tau} \right], \tag{3.22}$$

$$A_\mu^{(n)} = \frac{1}{i} U_n(\boldsymbol{x}) \partial_\mu U_n^\dagger(\boldsymbol{x}), \tag{3.23}$$

where $\boldsymbol{\tau}$ are the generators of the gauge group. As we know from quantum field theory, these gauge transformations describe the additional redundant degrees of freedom we have in the system due to degenerate states. This is to say that such small gauge transformations, as given by $U_n(\boldsymbol{x})$, connect physically equivalent configurations with each other through continuous transformations. In the topological language we state that small gauge transformations may hence be continuously deformed to the identity element. There exist also large gauge transformations which connect physically in-equivalent settings such as configurations with different winding numbers Q_w, which are regarded as being topologically distinct vacua of the system [34]. From topological considerations we know that we have no possibility to continuously transform from $A_\mu^{(n)}$ to $A_\mu^{(m)}$ with $m \neq n$ without leaving the pure gauge. As a consequence, any transformation interpolating between two such pure gauges must go through a barrier of non zero energy. Thus, such transformations, which are the instantons, are said to describe tunneling effects between various topological vacua as illustrated in Fig. 3.3.

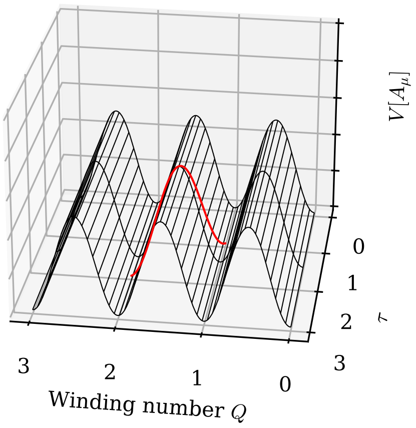

Figure 3.3: illustrative example of a shape of the potential energy (black) as a function of the winding number and imaginary time. The instanton solution (red) interpolates between two topologically distinct vacua.

Now we turn to the task of defining the instanton charge. In analogy to our derivation of the soliton shape in section 3.2, we make use of the Bogomolny bound for the Euclidean Yang-

Mills action

$$S_E = \frac{1}{4}\int \mathrm{d}^d x F^a_{\mu\nu} F^a_{\mu\nu} \geq \pm\frac{1}{4}\int \mathrm{d}^d x F^a_{\mu\nu} \tilde{F}^a_{\mu\nu}, \tag{3.24}$$

where we have defined the dual field strength tensor $\tilde{F}^a_{\mu\nu} = \epsilon_{\mu\nu\lambda\sigma} F^{a\,\lambda\sigma}$. Satisfying this lower bound, we can write the instanton charge as

$$Q_I = \int_{-\infty}^{\infty} \mathrm{d}\tau\, \partial_\tau \int j^0\, \mathrm{d}\mathbf{x} = Q_w(\tau = \infty) - Q_w(\tau = -\infty) \in \mathbb{Z}. \tag{3.25}$$

Therefore, we see that instantons with a charge $Q_I = 1$ can be seen as events at times where the system tunnels from a configuration with a winding number $Q_{w,I}$ to one with a winding number $Q_{w,II}$. Hence, if we would look for changes in the winding number of the system in time, it would be suggestive that we have instantons in our system. The calculation of the winding numbers is slightly different for the 1 + 1 dimensional system, and it is worth noting that the topological charge is given by

$$Q_I = \int_{-\infty}^{\infty} \mathrm{d}\tau\, \partial_\tau \int_{0}^{L} \frac{1}{2\pi} A_1\, \mathrm{d}x\,, \tag{3.26}$$

where L is the size of the system.

3.5 Homotopy Groups of the Spin-1 BEC

We have now discussed the importance of homotopy groups and classes in the context of field theory and we have seen two sorts of objects which can come about in general field theories. An example was always given for the simplest form of objects which are the ϕ^4 kinks, but now we must apply what we have discussed to our system. To this end, it is important to investigate the symmetries of the spin-1 Hamiltonian further and extract the vacuum manifolds of the system. Following the works of [15, 35], we consider the mean-field description once more and explore the (broken) symmetries of the ground state of the spinor gas in question. We have already seen in section 2.1.1 that for a system with $q \neq 0$, the symmetry of the Hamiltonian is invariant under rotations of the group

$$G = SO(2) \rtimes \mathbb{Z}_2 \times U(1). \tag{3.27}$$

We can now turn to investigating the order parameter itself. Consider the normalized spinor

$$\zeta = \frac{\psi}{\sqrt{\psi^\dagger \psi}}. \tag{3.28}$$

The space spanned by ζ is ismorphic to the five dimensional sphere $\mathcal{M} = S^5$. For each $\zeta \in \mathcal{M}$ we define a subgroup $H_\zeta \subset G$, as the subgroup that leaves ζ invariant.

$$H_\zeta = \{g \in G | g\boldsymbol{\zeta} = \zeta\}. \tag{3.29}$$

Next, we define the orbit of $\boldsymbol{\zeta}$ as

$$\mathcal{M}_O(\boldsymbol{\zeta}) = \{g\boldsymbol{\zeta} | g \in G\} \subset \mathcal{M}, \tag{3.30}$$

In other words, the orbit of $\boldsymbol{\zeta}$ is the set of all points we obtain by letting the transformations in G act on the order parameter. These transformations do not change the energy and constitute a degenerate space in $\mathcal{M}$. In a more intuitive way, we might see how such a transformation acts on the order parmeter of the polar phase $\boldsymbol{\zeta}^P = (0, 1, 0)^T$

$$g\boldsymbol{\zeta}^P = e^{i\phi} e^{-i\alpha f_z} e^{-i\beta f_y} e^{-i\gamma f_z} \begin{pmatrix} 0 \\ 1 \\ 0 \end{pmatrix} = e^{i\phi} \begin{pmatrix} -\frac{e^{-i\alpha}}{\sqrt{2}} \sin\beta \\ \cos\beta \\ \frac{e^{i\alpha}}{\sqrt{2}} \sin\beta \end{pmatrix}. \tag{3.31}$$

We see that by rotating by $\beta = \pi$ and subsequently a rotation of $\phi = \pi$ we leave $\boldsymbol{\zeta}^P$ invariant, even with an arbitrary rotation about the f_z axis by an angle α. Therefore, we see that $H_{\zeta^P} = SO(2)_{f_z} \rtimes (\mathbb{Z}_2)_{f,\phi}$. As a last step, we define the order parameter manifold $\mathcal{R}^P$ as a left coset of H_{ζ^P}

$$\mathcal{R}^P = G/H_{\zeta^P} = \{gH_{\zeta^P} | g \in G\}. \tag{3.32}$$

The order parameter manifold describes the broken symmetry of the system, which is a manifold of the degenerate space. As we recall from the discussion in section 3.2, the existence of degenerate vacua is crucial for the existence of topologically stable configurations. The order parameter manifold for the polar phase is thus

$$\mathcal{R}^P \cong \frac{S_f^2 \times U(1)_\phi}{(\mathbb{Z}_2)_{f,\phi}}. \tag{3.33}$$

In one dimension, the fundamental homotopy group of the order parameter manifold is

$$\pi_1(\mathcal{R}^P) = \mathbb{Z}, \tag{3.34}$$

allowing for soliton solutions of integer winding numbers in the system. We note that we have not made any assumption regarding the dynamics of the system other than looking at the present symmetries of the Hamiltonian and its ground state. This shows the power of topological considerations.

Of further interest is the order parameter manifold of the easy-plane phase. As discussed above, quenching the system from the polar into the easy-plane phase breaks all remaining symmetries of the system. Hence, the order parameter manifold is given by

$$\mathcal{R}^{EP} = S^1_f \times U(1)_\phi. \tag{3.35}$$

We thus expect in this phase to find also the homotopy group

$$\pi_1(\mathcal{R}^{EP}) = \mathbb{Z}. \tag{3.36}$$

4. Numerical Methods

In the previous chapters, we have introduced the basic analytic theory of the spin-1 BEC, stating at each step that the full dynamics are not analytically soluble. One must thus turn to the most powerful tool we have at our disposal: the computation power of modern computers. Previous works done in the research group of Prof. Dr. Thomas Gasenzer here in Heidelberg have been utilizing a code developed over the years in order to investigate dynamics of ultra-cold Bose gases far-from equilibrium [36, 37, 38, 4]. Use of numerical computations has led to significant progress in the understanding of out-of-equilibrium physics, due to powerful phenomenological insights gained from such numerical simulations. The main method by which we compute the time evolution of the system is the semi-classical truncated Wigner approximation, which allows us to compute the GPEs beyond the mean-field configuration.

Research conducted by Dr. Christian Schmied has improved on the efficiency and availability of methods to simulate and analyze the spin-1 Bose gas numerically [5, 4, 39, 40]. The code solves the coupled spin-1 GPEs by use of the split-step Fourier algorithm. The efficiency is increased substantially by performing discrete fast Fourier transforms (DFFT) and propagation on GPUs using the coding language CUDA. His code is the base for the simulations run in the course of this thesis.

In this chapter, we outline the numerical tools and methods for simulating the dynamics of the homogeneous or alternatively trapped spin-1 BEC in one spatial dimension. First, in section 4.1 we will discuss how the numerical grid is defined in momentum and position space. Then, we will outline the derivation of the truncated Wigner approximation (TWA) in section 4.2. The TWA introduces the quantum fluctuations by sampling quantum noise to the initial state in momentum space according to the density matrix of said state. Thereupon, the configuration is evolved in time according to the GPEs. Simulating many such single trajectories, each with its own sampled noise, and averaging over these runs recovers the dynamics of the system beyond the mean-field approximation. The time evolution of the system is calculated from the GPEs by means of a split-step Fourier algorithm, which will be outlined in section 4.3.

4.1 Discretization of the GPEs

The EOM derived in section 2.2.1 must first be discretized in order to be solved numerically. To this end, we follow the procedure outlined in [24] and [5]. On a computer, the wave functions $\boldsymbol{\psi}(x)$ live each as a function on a discrete grid of N_g grid points, meaning the functions are vectors of size N_g. We define the grid spacing as Δx_g and observe that conversion between numerical units and physical units is given by the length scale Δx_g, to which we can associate a real physical length L, such that $\Delta x_g = L/N_g$, and a time scale $\omega_g = \hbar/M\Delta x_g^2$. The resulting variables of the system are given as

$$\bar{x} = \frac{x}{\Delta x_g}, \quad \bar{t} = \omega_g t, \quad \bar{c}_{0,1} = \frac{c_{0,1}}{\hbar\omega_g\Delta x_g}, \quad \bar{\omega}_{\|,\perp} = \frac{\omega_{\|,\perp}}{\omega}, \quad \bar{q} = \frac{q}{\hbar\omega}, \quad \bar{\psi}_m = \sqrt{\Delta x_g}\psi_m, \tag{4.1}$$

where the barred quantities are the numerical dimensionless quantities. For the rest of this thesis, we will omit the bar and discuss quantities in their numerical units, unless specified otherwise.

Thus far, we have discussed the spatial grid in position space, yet especially when using the split-step Fourier we are also interested in the momentum space grid. Many features of interest can be better seen in momentum space and it is hence of utmost importance to define a sensible momentum grid. To derive the momenta we expand the fields into discrete plane waves, which is equivalent to performing a discrete Fourier transform (DFT). We then compute the discrete finite size Laplacian on the grid, which as we know for plane waves will simply give a factor of k^2. We write $\psi(x_j) = \psi_j$ and obtain

$$\hat{k}^2\psi_j = \Delta\psi_j = \frac{\psi_{j+1} - 2\psi_j + \psi_{j-1}}{\Delta x_g^2}. \tag{4.2}$$

We insert the wave expansion into to the Laplacian and obtain the lattice momenta

$$k_n = \frac{2}{N_g}\sin\left(\frac{\pi n}{N_g}\right), \tag{4.3}$$

where $n \in [-N_g/2 + 1, N_g/2]$. This definition leads to a denser momentum spacing in the ultra-violet (UV) and a nearly linear spacing in the infra-red (IR). The main reason for such a definition is the equivalence of the split-step Fourier method to that of finite difference methods for solving partial differential equations. A sensible definition to allow comparison of results is of course an important step.

4.2 Truncated Wigner Approximation

As stated in the introduction of this chapter, the workhorse of our numerical investigation of the system is the TWA. The TWA makes use of a phase space description of quantum many-body systems and thus we must first introduce the most important concepts of this description. Following the works of [41, 42, 24] we first introduce a map between quantum operators and ordinary complex functions in phase space. We assume a coherent state representation of the phase space and introduce the Weyl symbol (also Weyl transform) of an arbitrary operator $\hat{A}\left(\hat{\boldsymbol{\Psi}}, \hat{\boldsymbol{\Psi}}^{\dagger}\right)$, which is defined as

$$A_W(\boldsymbol{\psi}, \boldsymbol{\psi}^*) = \int\int \frac{\mathrm{d}\boldsymbol{\gamma}^*\,\mathrm{d}\boldsymbol{\gamma}}{2^D} \left\langle \boldsymbol{\psi} - \frac{\boldsymbol{\gamma}}{2} \middle| \hat{A}\left(\hat{\boldsymbol{\Psi}}, \hat{\boldsymbol{\Psi}}^{\dagger}\right) \middle| \boldsymbol{\psi} + \frac{\boldsymbol{\gamma}}{2} \right\rangle e^{-|\boldsymbol{\psi}|^2 - \frac{1}{4}|\boldsymbol{\gamma}|^2} e^{\frac{1}{2}(\boldsymbol{\gamma}^*\boldsymbol{\psi} - \boldsymbol{\gamma}\boldsymbol{\psi}^*)}, \tag{4.4}$$

where once more $\boldsymbol{\psi}$ is the spinor vector containing the magnetic sub-levels of the spin-1 BEC and D is the size of the Hilbert space. We now choose the arbitrary operator to be the density matrix $\hat{\rho}$ of our quantum state. This special construction of the Weyl symbol is called the Wigner function $\mathcal{W}(\boldsymbol{\psi}, \boldsymbol{\psi}^*)$. The Wigner function serves as a quasi-probability distribution in the sense that, unlike a classical probability function, it can take on negative values. For large occupation numbers the Wigner function is semi-positive definite and may be treated as a classical probability distribution function [41]. We see that by inserting the density matrix into Eq. (4.4) we can write the expectation values of any arbitrary operator as

$$\left\langle \hat{A}\left(\hat{\boldsymbol{\Psi}}, \hat{\boldsymbol{\Psi}}^{\dagger}\right) \right\rangle = \int\int \mathrm{d}\boldsymbol{\psi}\,\mathrm{d}\boldsymbol{\psi}^*\, \mathcal{W}(\boldsymbol{\psi}, \boldsymbol{\psi}^*) A_W(\boldsymbol{\psi}, \boldsymbol{\psi}^*). \tag{4.5}$$

The next step is to understand how we acquire the quantum equations of motion from the Wigner function and the GPEs we have derived earlier. To this end, we investigate the Weyl symbols of products and commutators of quantum operators. We find that the Weyl symbol of a product of two operators is given by a Moyal product relation

$$(A_1 A_2)_W = A_{1,W} \exp\left[\frac{\Lambda}{2}\right] A_{2,W}, \tag{4.6}$$

where we have defined the symplectic coherent state operator

$$\Lambda = \sum_j \frac{\overleftarrow{\partial}}{\partial\psi_j}\frac{\overleftarrow{\partial}}{\partial\psi_j^*} - \frac{\overrightarrow{\partial}}{\partial\psi_j}\frac{\overrightarrow{\partial}}{\partial\psi_j^*}, \tag{4.7}$$

where the arrows above the differential operators indicate the direction on which they operate. Thus, with equations (4.6) and (4.7) we find the Weyl symbol of the commutator $\hat{A} = \left[\hat{A}_1, \hat{A}_2\right]$

is

$$A_w = 2A_{1,W} \sinh\left[\frac{\Lambda}{2}\right] A_{2,W}. \tag{4.8}$$

Next, we consider the famous von Neumann equation, describing the quantum dynamics of a density matrix in the Schrödinger picture

$$i\hbar\frac{\partial\hat{\rho}}{\partial t} = \left[\hat{H}, \hat{\rho}\right]. \tag{4.9}$$

We perform the Weyl transformation to both sides of the equation and make use of Eq. (4.8) to obtain the equations of motion for the Wigner function

$$i\hbar\frac{\partial\mathcal{W}}{\partial t} = 2H_W \sinh\left[\frac{\Lambda}{2}\right]\mathcal{W}, \tag{4.10}$$

where H_W is the Weyl symbol of the Hamiltonian of the system. In order to solve the equations of motion, we expand the hyperbolic sine in Λ and truncate the series expansion at the relevant order for our purposes. In the case of high occupation numbers, the modulus of the wave function is a very large number and the leading orders of the series expansion dominate, whereas the higher-order terms become less and less significant. We should always keep this condition in mind when we simulate the semi-classical dynamics of the system, as to make sure that the higher order corrections do not contribute significantly, and our calculated dynamics are a good approximation of reality. We thus truncate the series expansion in leading order of Λ, which is known as the truncated Wigner approximation. This truncation leads us to solve the classical Liouville equation

$$i\hbar\frac{\partial\mathcal{W}}{\partial t} = \{H_W, \mathcal{W}\}_P, \tag{4.11}$$

where $\{\cdot,\cdot\}_P$ denotes the Poisson brackets. This differential equation may be solved by the method of characteristics, which brings us to the final equations of motion

$$i\hbar\frac{\partial\psi_m}{\partial t} = \frac{\partial H_W}{\partial\psi_m^*}. \tag{4.12}$$

The Weyl symbol of the spin-1 Hamiltonian will introduce additional terms which are proportional to $|\psi_m|^2$, which in turn may be removed by global gauge transformations. This leads us to the final conclusion that the GPEs are the equations of motion we have now derived. Thus, we do not evolve the Wigner function itself in time, instead, we sample the initial condition from the initial density matrix, given by the Wigner function in momentum space and propagate such a sample of the classical field in time according to the GPEs. Hence, each run consists of an initial mean-field state, upon which quantum fluctuations are added by means of sampling from the Wigner function of the vacuum. This process is repeated many times and the quantum physics is recovered by averaging over many realizations. The sampling of quantum noise is explained thoroughly in [24]. Briefly, for the homogeneous case of no trapping potential, the initial Wigner function of a coherent state such as the ground state of the Bose gas (see section 2.3.1) is given by a Gaussian. Therefore, we add Gaussian noise to the Bogoliubov modes corresponding to an average occupation of half a particle in each mode

$$\left\langle \hat{a}^{\dagger}_{\boldsymbol{k},m}\hat{a}^{\dagger}_{\boldsymbol{k}',m'}\right\rangle = \frac{1}{2}\delta_{mm'}\delta_{\boldsymbol{k}\boldsymbol{k}'}. \tag{4.13}$$

4.3 Split-Step Fourier

In our previous discussion, we have defined the discretization of our grid in both position and momentum space and derived the equations of motion for the spin-1 BEC. Now we aim to numerically solve the EOM using pseudo-spectral time-splitting methods, also known as the split-step Fourier algorithm. As seen in the works of [43], the method preserves the particle number as well as the total energy and is a common method used to discretize times for a numerical solution of non-linear Schrödinger equations, such as the GPEs. In this section we give a brief introduction to the idea behind a single time-step integration. We begin by writing the EOM in matrix notation

$$i\hbar\frac{\partial\psi_m}{\partial t} = H_{ml}\psi_l, \tag{4.14}$$

where the indices m and l label the three magnetic sub-levels of the system. We can decompose the matrix-form Hamiltonian into a diagonal kinetic part $\mathcal{D}$ and an off-diagonal part containing the non-linear and other terms $\mathcal{N}$

$$H_{ml} = \mathcal{D}_{ml} + \mathcal{N}_{ml}. \tag{4.15}$$

As well known, the time evolution of the system by is given by multiplying the wave function with $e^{-iHt/\hbar}$. Thus, the solution of the wave function after a propagation by one time-step is given by

$$\psi_m(x, t+\Delta t) = \left(e^{-\frac{i}{\hbar}\Delta t H}\right)_{ml}\psi_l(x,t) = \left(e^{-\frac{i}{\hbar}\Delta t(\mathcal{D}+\mathcal{N})}\right)_{ml}\psi_l(x,t). \tag{4.16}$$

Now we come to the time-splitting part of the algorithm. Evolving the equations of motion in time is easily made if the term inside the exponential is diagonal, since then we only deal with a simple element-wise exponential. Thus, it is advantageous to operate in configurations where the matrices $\mathcal{D}$ and $\mathcal{N}$ are diagonal. Sadly, in general they are not simultanously diagonal. Fortunately, we may make a time-splitting ansatz and, with the help of the Baker-Hausdorff-Campbell formula, split the exponential function into two operations, hence gaining an error of $\mathcal{O}(\Delta t^2)$.

$$\psi_m(x, t + \Delta t) = \left(e^{-\frac{i}{\hbar}\Delta t \mathcal{D}}\right)_{ml} \left(e^{-\frac{i}{\hbar}\Delta t \mathcal{N}}\right)_{lk} \psi_k(x, t) + \mathcal{O}(\Delta t^2). \tag{4.17}$$

In our case, the kinetic part $\mathcal{D}$ is diagonal in momentum space and it is of great advantage to perform the time step in Fourier space, where $\mathcal{D}_{ml} = \frac{\hbar^2 k^2}{2M}\delta_{ml}$. For better visualization of the scheme, we define $\mathfrak{D}_{ml} = \left(e^{-\frac{i}{\hbar}\Delta t \mathcal{D}}\right)_{ml}$ and $\mathfrak{N}_{ml} = \left(e^{-\frac{i}{\hbar}\Delta t \mathcal{N}}\right)_{ml}$. Hence, by utilizing a three fractional step as outlined in [44, 45] to increase accuracy, we obtain the final integration scheme of one time step

$$\psi_m(x, t + \Delta t) = \mathcal{F}^{-1}\left\{\mathfrak{D}_{ml}\mathcal{F}\left[\mathfrak{N}_{lk}\,\mathcal{F}^{-1}\left(\mathfrak{D}_{kj}\mathcal{F}\left(\psi_j(x, t)\right)\right)\right]\right\} + \mathcal{O}(\Delta t^3), \tag{4.18}$$

where $\mathcal{F}$ denotes the Fourier transform. Thus, by utilizing the efficiency of applying fast Fourier transforms parallelized on GPUs to each time-step propagation, we increase the efficiency of the integration scheme significantly.

5. Dynamics After Parameter Quench

After concluding our introduction of the spin-1 BEC and the numerical methods we use to study it, we may begin our analysis of the spin-1 BEC far from equilibrium. In this chapter, we take a look into the time evolution of the system following a parameter quench of the quadratic Zeeman effect q. This procedure is of special interest due to its experimental accessibility. The quadratic Zeeman effect can be relatively simply manipulated by tuning either the magnetic field or the manipulation of an off-resonant microwave field, a technique known as microwave dressing [3]. After quenching the system, we expect to observe a complicated time evolution, as the system tries to return to equilibrium. After a short period of time, the system will reach a regime of slowed down time evolution, and it will begin to evolve in a self-similar manner, implying the scaling of a universal correlation function in time with two macroscopic exponents α and β [39, 46].

In the dynamics of the system we will observe the formation of structures in the different degrees of freedom in the spin-1 BEC which we set our minds to investigate by utilizing various concepts of topology and statistics. The discussion of the dynamics of the system will be held for three different initial conditions. Firstly, in section 5.1 we will study the system initially prepared in the polar phase and subsequently quenched to the easy-plane. While investigating the topology of the system, we will find evidence of instantons in the dynamics of the BEC. In section 5.2, we aim to further investigate the role of instantons play in the dynamics of the system. To this end, we take a look at the dynamics of the system prepared in the easy-plane with all the spins oriented in the $F_x = 1$ direction and subsequently quenched deeper into the easy-plane. This construction will allow us to observe instantons and their effect in an isolated manner. We calculate the statistics of instantons in the system in the context of scaling in the system. In the last section 5.3 we write in defects into the polar phase by the use of local rotations in spin space, thereupon quenching the system to the easy-plane. We explore the arising universal dynamics and discuss their implication.

The results of the simulations are given mostly in characteristic dimensionless length- and time-scales which are determined by the energy scale of the system. We give lengths in units of the spin healing length ξ_s and times in units of the spin collision time t_s, which is a characteristic time-scale on which spin interactions happen. These are given in numerical units by

$$\xi_s = \frac{1}{\sqrt{2n|c_1|}}, \quad t_s = \frac{2\pi}{n|c_1|}. \tag{5.1}$$

Amplitudes of various observables such as spin lengths and densities are all normalized with respect to the homogeneous mean density $n = \langle\rho\rangle$.

5.1 Polar Initial Condition

The first scenario we will investigate is a quench from the polar to the easy-plane phase. To do so, we calculate the time evolution of the wave functions using truncated Wigner simulations. We prepare our system initially in the mean-field ground state of the polar phase, with the entire condensate occupation in the $m_f = 0$ component. Then, we add quantum noise to the Bogoliubov modes as discussed in section 4.2, thus planting the seed for dynamical instabilities to take place. After the initial preparation of the system, the quadratic Zeeman effect strength q is changed instantly to a value of $q_f = 0.9n|c_1|$. This construction takes the BEC through a second order QPT and thus out of equilibrium. Furthermore, we note that this specific dynamical arrangement was thoroughly studied by Dr. Christian Schmied in his research of bi-directional scaling in the one-dimensional spin-1 BEC [4]. We deliberately investigate this known case in order to be able and expand on the present knowledge without getting into the details of inspecting a new system.

5.1.1 Space-Time Evolution After a Quench

In the following section, we will present and discuss single truncated Wigner realizations of space-time evolution following the quench from the polar to the easy-plane. This discussion will help us gain some qualitative intuition as to the dynamics and structures found in the system in its far-from-equilibrium time evolution. For future reference we shall call this construction the polar quench.

We simulated a ^{87}Rb-like spin-1 condensate in a zero temperature, homogeneous (i.e. no trapping potential) setting on a grid of $N_g = 4096$ grid points with periodic boundary conditions. The grid corresponds to a physical length of $L = 220\mu m$. A particle number of $N = 3 \cdot 10^6$ was chosen and interaction strengths were set to $c_0 = c_0^{^{87}Rb}$ and $c_1/c_0 = -0.01$. The chosen c_1 value does not deviate significantly from the experimentally obtained value [15], and it allows us to better resolve certain length scales in the system. Our ultimate goal is to further understand the self-similar scaling behavior of the system, which is associated with the system evolving to a non-thermal fixed point (NTFP) on its way to equilibrium. In order to qualitatively understand

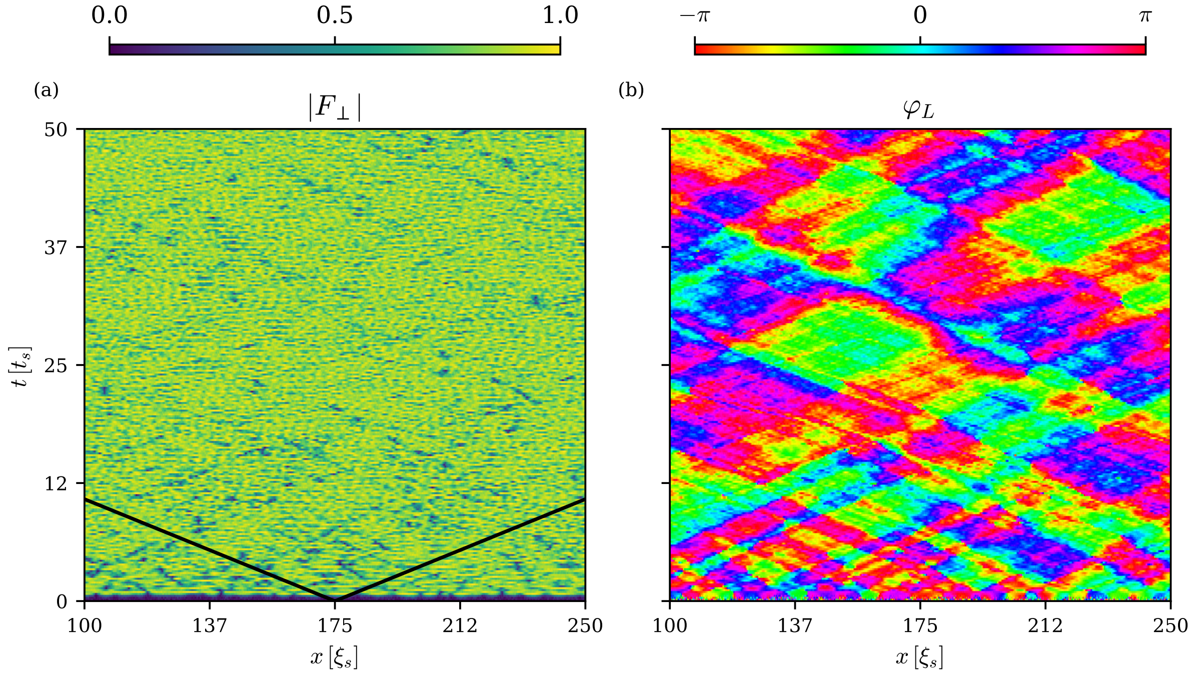

Figure 5.1: A small excerpt of the space-time evolution of the transverse spin $F_\perp = |F_\perp|e^{i\varphi_L}$ as given by a single truncated Wigner trajectory for $N = 3 \cdot 10^6$, $L = 220\mu m$, $|c_1/c_0| = 0.01$ and $q_f = 0.9n|c_1|$. Panel (a) shows the transverse spin length $|F_\perp|$. The sound cone of the spin speed of sound $c_s = \sqrt{n|c_1|}$ (black solid lines) is also plotted. Panel (b) displays the Larmor Phase φ_L.

this self-similar scaling of the order parameter, it is advantageous to first study the structures in said order parameter. As mentioned in section 2.2.2, the QPT between the polar phase and the easy-plane phase is characterized by a phase transition between a phase with no magnetization, and a phase with non-vanishing transverse magnetization. Thus, the order parameter in question is the transverse spin $F_\perp = F_x + iF_y = |F_\perp|e^{i\varphi_L}$.

In Fig. 5.1 we observe the spatially resolved short-time evolution of an excerpt of the entire system. We see that the system is indeed initially in the polar phase, where the system displays no magnetization. Then, after an adjustment time of $t \approx t_s$, spin changing collisions occur and the system obtains a mean background transverse spin length, with additional fluctuations of the spin length, as seen by the random dips in mean density. The dips show no obvious structure in the condensate and the fluctuations seem to be of relatively low amplitude. The case seems to be rather different in the dynamics of the Larmor phase φ_L. It appears as though phase fluctuations dominate the dynamics of the system and one can recognize patterns and structures forming in this degree of freedom. These structures, or domains of approximately equal phase, look like they are following some sort of length scale, which grows in time. This is to say that we may already see some length scale coarsening phenomena in our system by looking at a single realization. Furthermore, the phase domains seem to be separated by sharp jumps in the phase of approximately π, already giving a notion of perhaps quasi-topological

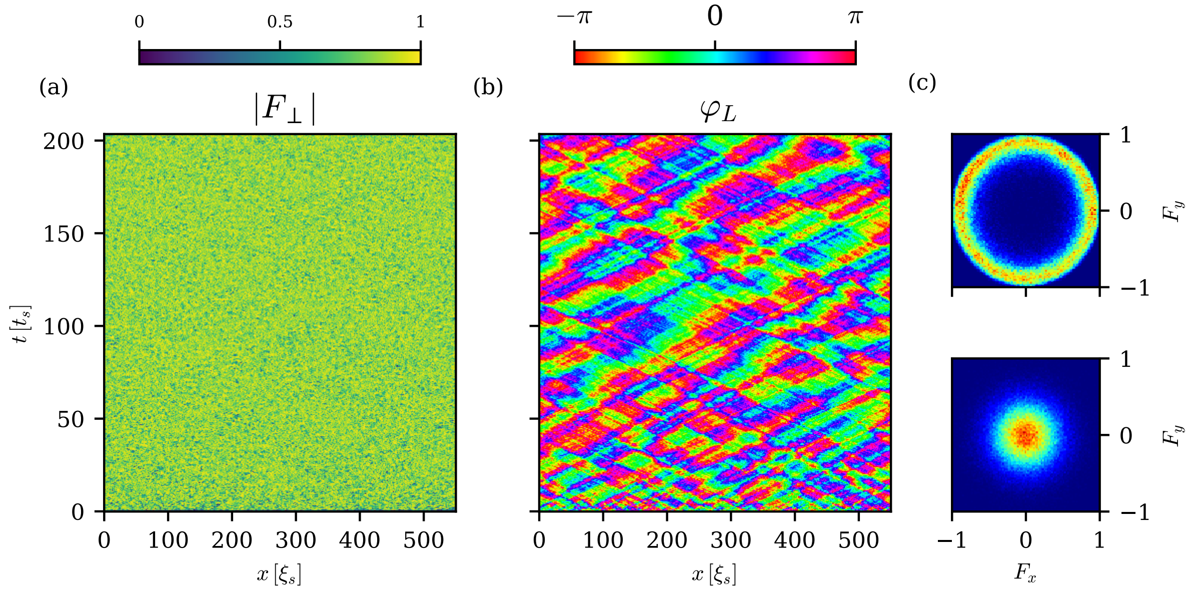

Figure 5.2: Space-time evolution of the transverse spin $F_\perp = |F_\perp|e^{i\varphi_L}$ in a single truncated Wigner realization after a quench from the polar phase to the easy-plane phase with $q_f = 0.9n|c_1|$. The system is initialy prepared in the polar phase with a particle number of $N = 3 \cdot 10^6$, a physical length of $L = 220\mu m$ and interactions $|c_1/c_0| = 0.01$. Panels (a) and (b) show the transverse spin length and its phase respectively. Panel (c) shows the histograms in spin space in $t = 0$ (bottom) and $t = 160t_s$ (top).

objects propagating in the system.

In Fig. 5.2 we observe the space-time evolution of the system for times up to $t = 200t_s$. Also in the long-time evolution the structures appearing in the Larmor phase are dominant and appear to obey some length scale, which seems to grow in time. At each time, each grid point has a certain spin orientation. This orientation is recorded into a two dimensional histogram of the $F_x - F_y$ plane and averaged over several realizations to give a realistic statistic of the local spin orientations of the system, as presented in Fig. 5.2 (c). This representation of the spins allows us to gain some more intuition to the fluctuations of the spin length and the broken symmetry of the system. At time $t = 0$, we see the spin is localized around the origin of a ball and one might already get a notion of the $SO(2)$ symmetry present. Then, at later times $t = 160t_s$ we see that the spin histogram forms a ring-like structure. Firstly, we might already conclude that as stated above, the formation of a ring agrees with the statement about small spin length fluctuations, since if the fluctuations would have been large, we would observe a much thicker ring. Second, we see the aforementioned broken $SO(2)$ in its full glory, thus confirming our discussions in section 3.5. At each grid point at each time the Larmor phase, i.e. the orientation of the spin in the $F_x - F_y$ plane is chosen at random, due to the degeneracy of the ground state configuration.

Next, we might ask ourselves if our restriction to the $F_x - F_y$ plane is justified. Fig. 5.2 shows the dynamics in the transverse directions, but does not yield information about the F_z

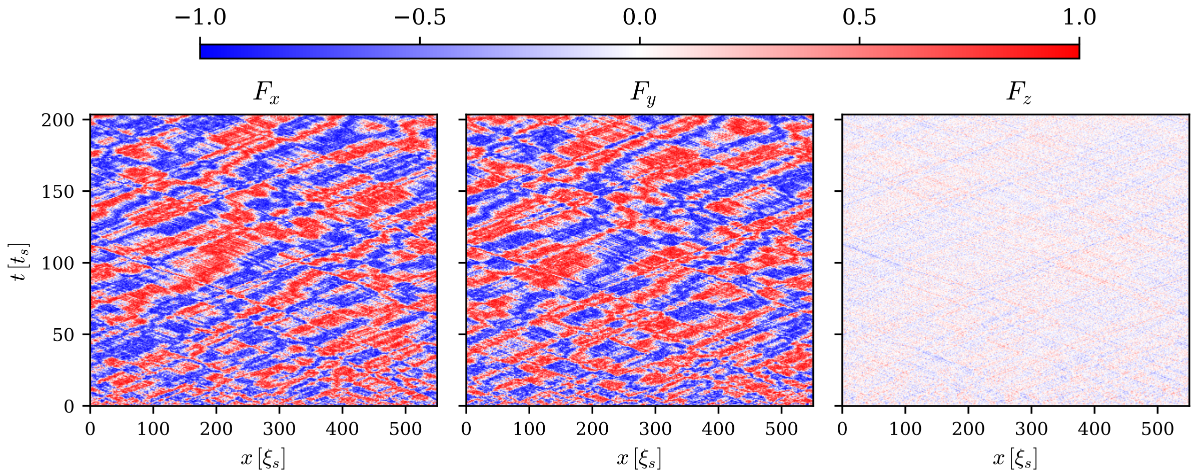

Figure 5.3: Space-time evolution of the three spin components of a single truncated Wigner realization after a quench from the polar phase to the easy-plane for $N = 3 \cdot 10^6$, $L = 220\mu m$. $|c_1/c_0|$ and $q_f = 0.9n|c_1|$.

direction. In Fig. 5.3 we observe the three spin directions and their amplitude. It is rather apparent that in the F_z orientation only very small fluctuations about a mean zero background take place and the dynamics of interest are concentrated mainly in the F_x and F_y directions. The structures seen remind of magnetic domains of two different ground states interacting with one another to comprise a complicated, yet beautiful dynamic. This representation of the spin sphere, given by Figures 5.2 and 5.3, allows us to characterize the structures in the system after a quench. The domains in the spin are separated by domain walls, which can be observed as rather straight white lines which propagate in a sea of red and blue. These same objects can be seen in the Larmor phase as sharp jumps in the phase of approximately π that propagate through the gas. These sharp jumps can be seen as a sort of defect in the system. These defects would show themselves in the histograms as trajectories going from one grid point to the next one (or a very near grid point) through the middle of the ring, also causing a dip in the transverse spin length. The close inspection and statistics of these spin textures will be discussed in section 5.2.2.

5.1.2 Spectra and Self-Similar Scaling

The above discussed single realizations gave us a qualitative idea of the phenomena in the system, but now we turn to analyzing the dynamics quantitatively. The TWA requires us to calculate many such single trajectories and gather statistics. As discussed in chapter 1, the theory of the NTFP states that after the system ends its short-time evolution it will approach a regime of slowed self-similar scaling according to a certain universality class. Therefore, we expect the correlations of the order parameter of the system to scale in momentum space according to

$$S(k,t) = \left(\frac{t}{t_{ref}}\right)^{\alpha} f_s\left([t/t_{ref}]^{-\beta}k\right), \tag{5.2}$$

where f_s is the universal scaling function, t_{ref} is an arbitrary reference time and in our case

$$S(k,t) = \left\langle |F_\perp(k,t)|^2 \right\rangle. \tag{5.3}$$

The real-space dynamics seen in Fig. 5.1 give us a notion of what we should expect from the behavior of the transverse spin structure factor, namely, we expect the structure factor to first show only the seeded quantum fluctuations in all the modes, then as the system is immediately quenched to the easy-plane, we anticipate that dynamical instabilities in the Bogoliubov modes

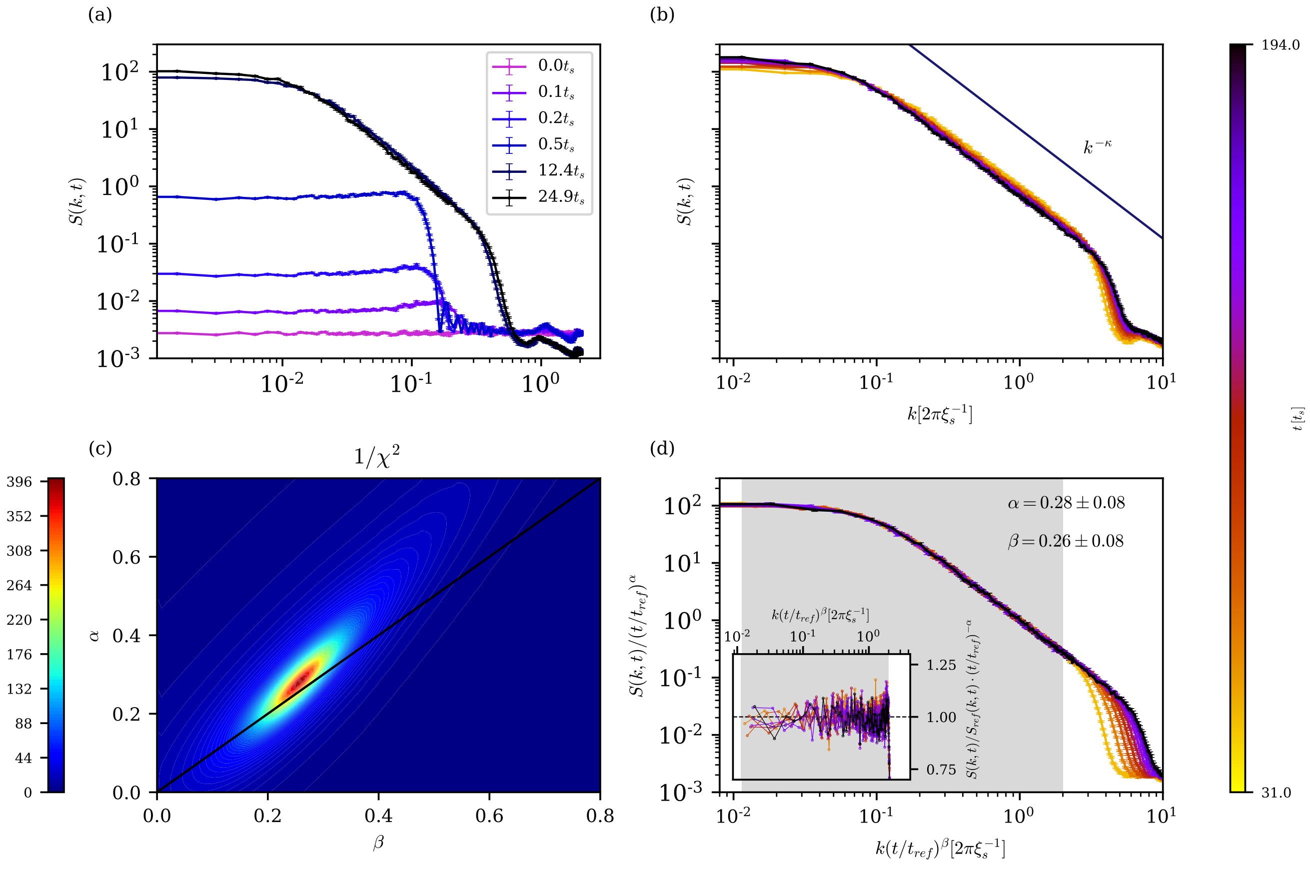

Figure 5.4: Self-similar time evolution of the transverse spin structure factor $S(k,t) = \left\langle |F_\perp(k,t)|^2 \right\rangle$. Panel (a) presents the short-time evolution of the spectrum, as dynamical instabilities give rise to structure in the transverse spin. Panel (b) shows the raw spectra at times between $t = 31t_s$ and $t = 194t_s$. As a visual aid a power law of k^{-2} was plotted. In panel (c) we see a contour plot of the inverse cumulative error $1/\chi^2$ of the rescaling algorithm as a function of α and β. Panel (d) displays the rescaled spectra with $\alpha = 0.28 \pm 0.08$ and $\beta = 0.26 \pm 0.08$. The inset presents the residuals of the rescaled spectra from the reference spectrum. Spectra were averaged over $\sim 10^3$ truncated Wigner realizations of a BEC with $N = 3 \cdot 10^6$, on a physical length $L = 220\mu m$, with interactions $|c_1/c_0| = 0.01$, quenched from the polar phase to the easy-plane with $q_f = 0.9n|c_1|$.

will cause a rise in occupation in the $m_f = \pm 1$ components, leading to a quick build-up of transverse spin. The short-time evolution of the structure factor is seen in Fig. 5.4 (a) and appears to corroborate our expectations.

In this thesis, we will only give the main results of scaling in the IR, without going into detail regarding Bogoliubov predictions and conservation laws. Should the reader be interested in a more thorough discussion of the transverse spin spectra, we refer to Ref. [4]. We find that after a time of $t \approx 25t_s$, the system enters said universal regime and the structure factor spectra seem to scale in time. According to the low-energy effective theory of multi-component Bose gases [12], we expect the spectra to follow a power law of $S(k,t) \propto k^{-\kappa}$ with $\kappa = -2$ in intermediate momenta ranges.

Fig. 5.4 (b)-(d) shows the results of averaging over $\sim 10^3$ truncated Wigner realizations. As expected, for intermediate times the spectra show a constant form, or more accurately put, they take the form of the universal scaling function. In order to extract the scaling exponents α and β, we utilize a rescaling algorithm based on a linear interpolation of the reference spectrum, i.e. the spectrum at the reference time t_{ref}, and a least squares method for fitting the other curves onto the interpolated reference spectrum as outlined in the appendix of [47]. The extracted exponents are thus the exponents corresponding to the minimal error χ^2 in the fit procedure. Upon interpolating the spectra, we can calculate the likelihood function of the exponents as

$$W(\alpha,\beta) = \frac{1}{\mathcal{N}} \exp\left[-\frac{-\chi^2(\alpha,\beta)}{2\chi^2_{min}}\right]. \tag{5.4}$$

Then, by integrating over one of the exponents, we obtain the marginal likelihood function of the other, for example

$$W(\alpha) = \int W(\alpha,\beta)\,\mathrm{d}\beta\,. \tag{5.5}$$

Each marginal likelihood function can be approximated by a Gaussian and we thus extract the error for each exponents out of the standard deviation of its respective marginal likelihood function. The results of the rescaling algorithm can be seen in Fig. 5.4 (d) and we obtain the scaling exponents

$$\alpha = 0.28 \pm 0.08, \quad \beta = 0.26 \pm 0.08. \tag{5.6}$$

As one can see, all curves fall unto the same line. The inset plot shows us the relative error of a rescaled spectrum w.r.t the reference spectrum. The equal distribution of the relative error implies the stability of the universal form of the spectra, since should we observe a preferred direction or strong deviations from the reference spectrum this would mean the shape of the spectrum is changing with time. Hence, we may still safely speak of self-similar scaling. In the contour plot 5.4 (c), we observe the possible values of α and β and their respective values of $1/\chi^2$. Also plotted, is the $\alpha = \beta$ line. It is important to notice that following the low-energy effective theory for multi-component Bose-gases, a few constraints are taken into account in order to calculate the scaling exponents. One of these constraints is the quasi-particle number conservation stating $\int_k S(k,t) = const$ [12]. As a result, one may constrain the two exponents to obey $\alpha = d\beta$, which in our one-dimensional case translates to $\alpha = \beta$. It is thus rather calming to see that the dynamics of the system obey the predictions of the low-energy effective theory in a $1 + 1D$ setting.

The question now remains, what is responsible for this anomalous scaling? In Ref. [4], [6] and many more, it was connected to the emergence of topological objects and spin textures in the system and the coarsening of the domains which they build. We now turn to some tools to help us analyze this claim and help us gain further insights into the dynamics of the system.

5.1.3 Topology of the System

In this section, we will connect the discussion of topology in chapter 3 to the relevant case of the polar quench. These topological considerations will help us gain further insight into the underlying physical processes governing the dynamics of the system. We begin by recalling that the order parameter manifold in the easy-plane was given by

$$\mathcal{R}^{EP} = SO(2)_f \times U(1)_\phi, \tag{5.7}$$

which has the non trivial homotopy group $\pi_1(S^1_f) = \mathbb{Z}$. Hence, we expect topological objects to be formed due to the broken $SO(2)$ symmetry which is reflected mainly in the Larmor phase. Thus, it is a sensible approach to concentrate on the Larmor phase as a scalar field and develop our theory around that notion. The phenomenological restriction to the $F_x - F_y$ plane with a weekly fluctuating spin length and strong fluctuating phase allows us to reduce our theory to a single component complex scalar field $F_\perp$. We consider a low-energy effective theory, where density fluctuations are integrated out (here the density corresponds to $|F_\perp|$), leaving us with the Larmor phase as our field. For now we shall refrain from giving an explicit expression for any Lagrangian, since the subtleties of the theory are not yet fully understood. In principle, we expect a Lagrangian of the form

$$\mathcal{L} \propto (\partial_t \varphi_L)^2 - (\partial_x \varphi_L)^2, \tag{5.8}$$

with some sort of potential term, whose configuration is unknown, yet we will later argue as to its possible nature. We recall that the appearance of topological objects is always connected to some topological charge and current, which we can calculate. A topological charge for our complex scalar field $F_\perp$ can be constructed by taking

$$\phi_I = \cos\varphi_L, \quad \phi_{II} = \sin\varphi_L \tag{5.9}$$

and defining the topological current according to the recipe in Eq. (3.14) as follows:

$$j^\mu = \frac{1}{2\pi}\epsilon^{\mu\nu}\epsilon_{ab}\phi^a\partial_\nu\phi^b, \tag{5.10}$$

where μ, $\nu \in \{0,1\}$, corresponding to the time and spatial x direction respectively and a, $b \in \{I, II\}$ correspond to the field components. Plugging Eq.(5.9) into Eq. (5.10) gives us the two topological currents

$$j^0 = \partial^x\varphi_L, \quad j^1 = \partial^t\varphi_L. \tag{5.11}$$

As introduced in section 3.3, a topological charge is calculated by taking the spatial integral over the zeroth current

$$Q = \int \mathrm{d}x\, j^0 \in \mathbb{Z}. \tag{5.12}$$

Now we turn to the concept of gauge fields to derive the expected instantonic excitations in the system. We can think of the gradient of the Larmor phase in this context as a sort of pure $U(1)$ gauge field as can be seen if we choose the gauge field A_μ to be

$$A_\mu = \frac{1}{i}U\partial_\mu U^\dagger, \tag{5.13}$$

with $U = \exp(i\varphi_L(x)) \in U(1)$. This gives us

$$A_\mu = \partial_\mu\varphi_L. \tag{5.14}$$

Following the construction in 3.4, we may thus introduce a 1 + 1D electrodynamics theory, which allows us to compute a winding number according to

$$Q = \frac{1}{2\pi}\int_0^L \mathrm{d}x\, A_1(x) = \frac{1}{2\pi}\int_0^L \mathrm{d}x\, \partial_x\varphi_L \in \mathbb{Z}. \tag{5.15}$$

Therefore, may compute the instanton charge in imaginary time as in Eq. (3.25). We recall that such an instanton charge gives us a change of the winding number of the system in the imaginary time direction.

Fig. 5.5 shows the first component of the current j^1 in panel (b) and the winding number of the Larmor phase Q in panel (a). A few explanations are in order: in panel (b) we observe that j^1 peaks at the position of the phase defects or fluctuations we saw in Fig. 5.2. We observe

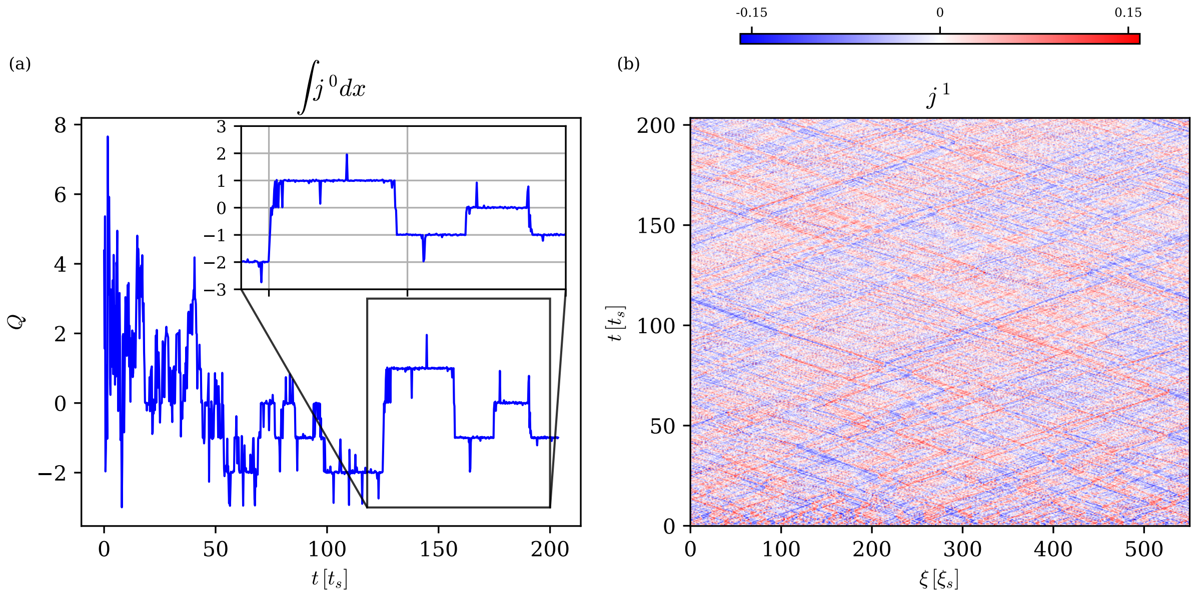

Figure 5.5: Topological considerations of the same single run seen in Fig. 5.2. Simulation was performed with a particle number of $N = 3 \cdot 10^6$, the physical length was set to $L = 220\mu m$, the interactions to $|c_1/c_0| = 0.01$ and the BEC was quenched to $q_f = 0.9n|c_1|$. Panel (a) shows the winding number $\int \partial^x \varphi_L \,\mathrm{d}x$ as a function of time, where the inset gives a zoomed in version of a time interval to resolve the integer values. Panel (b) displays the current $j^1 = \partial^t \varphi_L$, which identifies domain walls and their sign in the system.

that these peaks have a sign assigned to them and that at certain points in time, these peaks scatter off of each other. Sometimes, by doing so, they change their sign. Panel (a) shows that the topological charge Q performs integer valued jumps at various times during the time evolution of the system. The inset of the left figure shows that in late enough times the winding number of the system becomes stable for longer times, still showing sporadic jumps, yet these get less frequent with time. One may interpret these jumps as instantons and the lowered frequency as the decay in probability of instantonic excitations in the system.

One might ask oneself of the meaning of these phenomena. It turns out the interpretation is quite subtle. It is tempting to connect the winding number Q directly with the peaks and defects we observe in j^1 or in the Larmor phase space-time evolution in Fig. 5.2, but should these defects be the topological defects we are discussing, we would be able to circle around one defect and get its winding number, which should be a constant of motion. This seems not to be the case. The winding number is obtained by integrating over the entire length of the system. The appearance and subsequent change of these winding numbers may be a consequence of a complicated interplay of many degrees of freedom. In section 3.4 we have discussed the meaning of small and large gauge transformations. Here, we can see how the system tunnels between many kinds of topologically distinct vacua by means of large gauge transformations. Each vacuum is characterized by its respective homotopy class, i.e. its winding number. Thus, there exist an infinite amount of disjoint vacua configurations separated by some potential barrier in the gauge field $A_\mu = \partial_\mu \varphi_L$, across which the system must tunnel to arrive at the neighboring vacuum configuration as illustrated in Fig. 3.3. This might connect the theory of Larmor phase excitations to a sine-Gordon-like model, which is currently being investigated for its far-from-equilibrium scaling behavior [48, 49].

Furthermore, to explain why the topological objects seen in the spin degree of freedom come and go as they will, we mention that the target manifold we are dealing with is only phenomenologically S^1 on the mean-field level. The introduction of quantum noise means that the real target manifold may be a higher dimensional topological space. Since there is no strict constraint for the system to stay on this manifold, the topological charge does not enjoy any protection from its homotopy group and various configurations may be continuously deformed to the ground state.

5.2 Space-Time Vortices

After introducing the polar quench and discussing its topology, we may turn our focus on analyzing the appearance of instantons in the system. As we shall shortly see, we can treat these objects as some sort of space-time vortices. This notion is not strange to us, since the description of instantons in imaginary time allows us to treat the time dimension simply as an additional spatial dimension, which in turn allows us to observe them in analogy to vortices in $2D$. Naturally, since we are investigating dynamics far from equilibrium, an imaginary time description is not accessible to us and the real-time behavior of these objects is expected to be quite different. In order to better characterize these objects and their effect on the system, we turn to a different initial condition which has proven to be most useful.

5.2.1 Coherent State Initial Condition

We prepare the Bose gas in its easy-plane ground state, where all the spins are pointing into the positive F_x direction. That is to say, we prepare the system in a coherent state of full transverse spin length and a Larmor phase of $\varphi_L = 0$. Upon preparation, we quench the system within the easy-plane to a different quadratic Zeeman strength, coinciding with the one used for the polar quench scenario $q_f = 0.9n|c_1|$. Whether or not the system is to be considered far from equilibrium is not clear, but upon inspecting this system, an opportunity arose for us to be able to study the defects in the system in a more controlled setting than the polar quench. The simulations were run with slightly different parameters, mainly the atom number and thus the density have been change. The following system was simulated with $N = 5 \cdot 10^5$ particles, distributed over $L = 180\mu m$. The resolution in the x direction remains at $N_g = 4096$ grid points with periodic boundary conditions. This was done to ensure a better resolution of the density healing length.

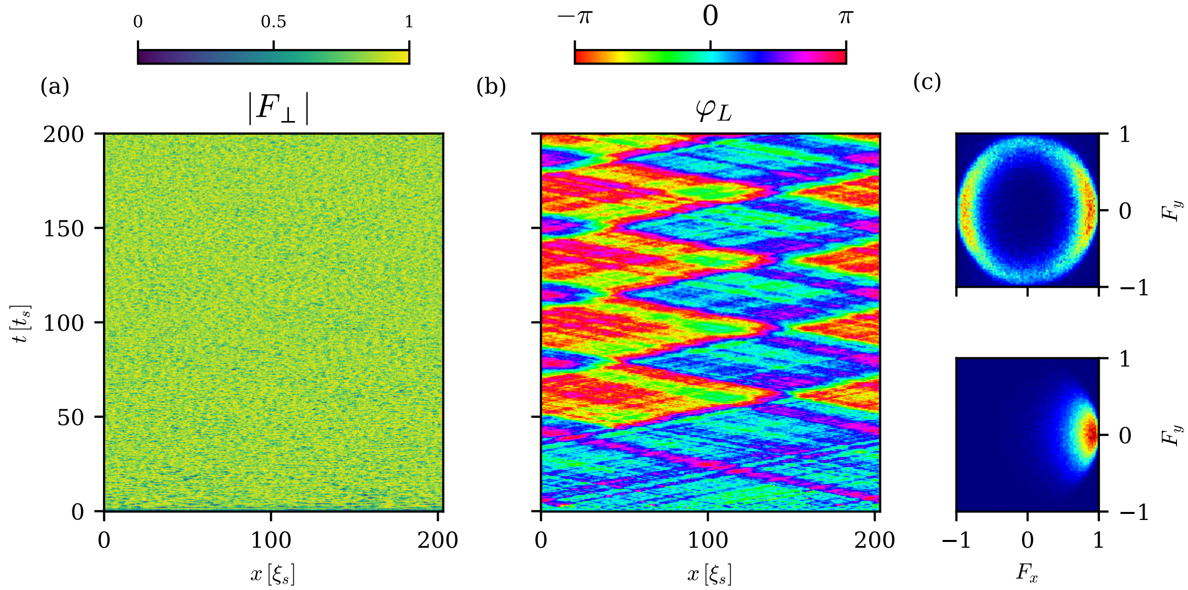

Figure 5.6: Space-time evolution of the transverse spin $F_\perp = |F_\perp|e^{i\varphi_L}$ in a single truncated Wigner realization of a coherent state in easy-plane phase with $q_f = 0.9n|c_1|$. The system is initialy prepared in the easy-plane phase with a full orientation of all spins in the $F_x = 1$ direction. The particle number was set to $N = 5 \cdot 10^5$, a physical length of $L = 180\mu m$ and interactions $|c_1/c_0| = 0.01$. Panels (a) and (b) show the transverse spin length and its phase respectively. Panel (c) shows the histograms in spin space in $t = 0$ (bottom) and $t = 160t_s$ (top). A different structure in the spin orientations is clear, as we no longer witness a ring in spin space, but rather a form reminiscent of "The Eye of Sauron".

in Fig. 5.6 we once more see the transverse spin degree of freedom and the structures arising in the condensate in time. From the Larmor phase and the histogram at $t = 0$, it is apparent that we begin with a fully orientated and coherent state. Through spin changing interactions the Larmor phase starts fluctuating. After a short while, at $t = 1 \cdot t_s$ we observe in panel (b) a kink and anti-kink forming in the Larmor phase and propagating through the system, seen as the pink line in the early stages of the time evolution up until a time at $t \approx 40t_s$. At that point in time, domains of the Larmor phase suddenly form, with a jump of approximately π.

The spin length itself remains approximately constant and fluctuates only slightly, same as we have seen in the polar quench case. Interestingly enough, one would expect in the easy-plane, a phase of complete broken symmetry, that the breaking of $SO(2)$ symmetry will lead the phase fluctuations to be distributed across a ring as in Fig. 5.2. This is not the case in this particular preparation. Instead, we observe something reminiscent of a broken $\mathbb{Z}_2$ symmetry, as the spin histograms give rise to a sort of "Eye of Sauron" as opposed to a ring. It is apparent that by giving the system a preferred direction, the system stays mainly on that axis fluctuating back and forth between the two F_x configurations. Why this configuration is energetically favorable, even though the system can obtain any value of spin along the $F_x - F_y$ plane is not yet clear.

5.2.2 Localizing Space-Time Vortices

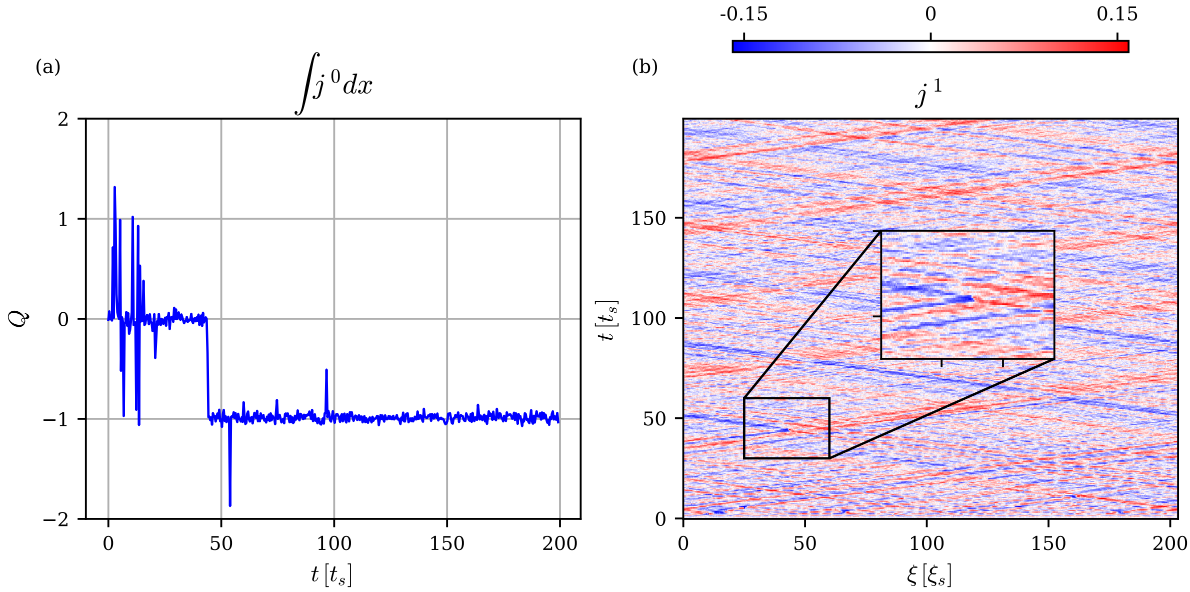

Figure 5.7: Topological considerations of the same single run seen in Fig. 5.6. The system was prepared in a coherent state of full spin orientation in the $F_x = 1$ direction. We set the particle number of $N = 5 \cdot 10^5$, the physical length to $L = 180\mu m$, the interactions to $|c_1/c_0| = 0.01$ and a quench to $q_f = 0.9n|c_1|$. Panel (a) shows the winding number $\int \partial^x \varphi_L \, dx$ as a function of time. Panel (b) shows the current $j^1 = \partial^t \varphi_L$, which identifies domain walls and their sign in the system. The inset shows a zoomed in view of a scattering event responsible for a change in the winding number, i.e. an instanton.

We now turn to investigating the topological properties of the coherent state initial condition. Since we are still in the easy-plane, the order parameter manifold remains the same and we expect to deal with the same topological objects as seen in the previous sections. In Fig. 5.7, we once more regard the winding number and first component of the topological current of the Larmor phase. We identify that, after a short time evolution, the system starts ordering itself and we observe a stabilization of the winding number to zero. After about $t \approx 40t_s$ we suddenly obtain a non vanishing negative winding number. This coincides with the above observation of the Larmor phase: at that instance in time suddenly phase domains have appeared! By studying the first component of the topological current j^1 we identify once more the domain walls that propagate through our system. Fig. 5.7 (b) contains the zoomed-in plot of j^1 as an inset. We find a peculiar scattering event in the current. A defect propagates, and then, by scattering off another defect, it changes its sign from positive to negative. Such an event does not repeat in the simulated time span, leading us to believe this spontaneous change of the current sign due to a scattering event is a spatial localization of an instanton, given by some sort of space-time vortex. Such events which give rise to Larmor phase domains, seem to concentrate on opposite spin configurations in the $F_x - F_y$ plane. such solutions are vacuum configurations with a well defined winding number, which in turn may be transformed with small gauge transformations to build the ring we have seen in the polar quench.

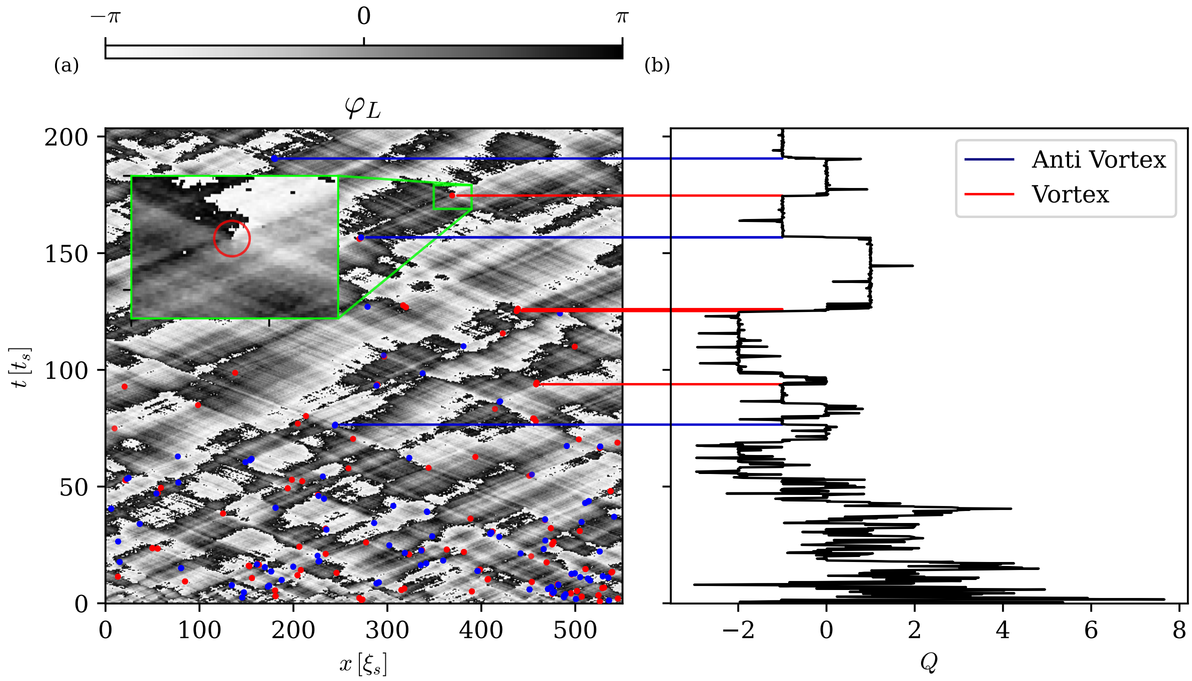

Figure 5.8: Space-time vortices of the Larmor phase within a single truncated Wigner trajectory of the polar quench. The system is initially prepared in the polar phase with $N = 3 \cdot 10^6$, $L = 220 \mu m$, $|c_1/c_0| = 0.01$ and subsequently quenched to $q_f = 0.9n|c_1|$. Panel (a) displays a greyscale version of the Larmor phase as seen in Fig. 5.2 with (anti-) vortices detected by a plaquette algorithm as (blue) red dots. The inset shows a zoomed-in view of a single a detected vortex. Panel (b) shows the winding number as a function of time (solid black) rotated by 90 degrees. A few exemplary (anti-) vortices were connected to their respective winding number jumps with (blue) red lines.

The existence of such space-time vortices can be further justified by applying a plaqutte algorithm to our space-time evolution of the polar quench, in analogy to the $2D$ vortex case. In Fig. 5.8 (a) we give a greyscale representation of the space-time evolution of the Larmor phase in the polar quench system, as previously seen in Fig. 5.2. A modified plaqutte algorithm in space-time was implemented. We choose a plaquette size of around $3\xi_s$ in the spatial direction and 3 time-steps in the t direction. Then, we integrate $\partial_x \varphi_L$ over the plaquette and iterate this procedure until we have covered the entire grid. Thereupon, we weight the results with the local deviation from the mean background transverse spin length $\langle |F_\perp| \rangle_x (t) - |F_\perp|(x,t)$, where $\langle \cdot \rangle_x$ denotes the spatial average. Thus, we expect a strong signal at exactly the point, where we have such a space-time vortex. Due to the noisy nature of the data, we will also obtain other sporadic strong signals at places of strong fluctuations, and some vortices may generate a signal too weak to detect, as it is on the level of the fluctuations in the signal. In order to filter unwanted data points, the location of the vortices in time was correlated to jumps in the winding number. Therefore, only plaquette peaks which are in the vicinity of a winding number jump were kept. The (blue) red dots in Fig 5.8 (a) are the found (anti-) vortices and the exemplary connecting lines show their correspondence to winding number changes, thus strengthening the notion of instantons in our spin-1 BEC.

This insight may lead to the interpretation of the coarsening in the system. The appearance of instantons in the system leads to a change in the winding number of the Larmor phase in the system, which in turn gives rise to domain formation of roughly equal phase values. For the case of the polar quench, where we give the system no preferred initial direction, many such events can happen with arbitrarily chosen orientations in the Larmor phase, causing a rather chaotic behavior in the Larmor phase as the system tunnels through various vacua through instantonic solutions. The winding and unwinding of the system becomes more rare as time passes and the system seeks to stabilize to a certain winding number, thus effectively causing less domains to appear in the system, which in turn gives rise to a changing and growing length scale, as the mean distance between such domain walls grows larger with time. In the next section, we will try and justify this argument quantitatively.

5.2.3 The Role of Space-Time Vortices in Universal Scaling

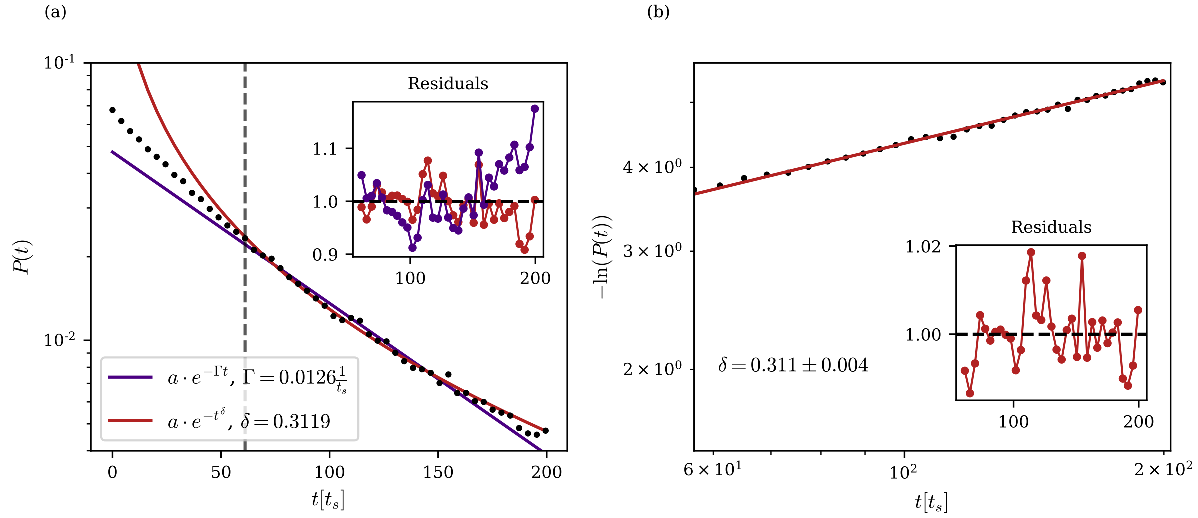

Figure 5.9: (a): Histogram of times at which a winding number jump (i.e. an instanton) was detected in the polar quench system on a linear-logarithmic scale. An exponential function $a \cdot e^{-\Gamma t}$ (purple) and a stretched exponential $a \cdot \exp\left(t^{\delta}\right)$ (red) were fitted on the data (black dots) in the time interval, at which the system shows self-similar scaling. The beginning of said time is marked by the gray dashed line. A decay rate of $\Gamma = (0.0126 \pm 0.001)\frac{1}{t_s}$ and a power law for the stretched exponential $\delta = 0.311 \pm 0.004$ were found. (b): Natural logarithm of the Histogram in (a) on a double logarithmic scale. A power law was fitted to obtain the same exponent for the stretched exponential. The insets show the relative deviation of the fits from the data.

As stated above, the data point gathered by the spatial localization of instantons may give unreliable statistics, due to falsly identified vortices. Nevertheless, we are interested in quantifying the effect the instantons have on the time evolution of the system as a whole. To this end, we constructed histograms of times, at which a topological charge jump was detected. We first filter the data using a median filter to reduce fluctuations. Then, we mark the times at which the time derivative of the charge reached a certain threshold, which is above the standard fluctuations. In Fig. 5.9, we observe the probability distribution of such events, associated with the appearance of instantons in the system. This probability distribution was fitted with an exponential function $f(t)$ and a stretched exponential function $g(t)$ using a least-squares method

$$f(t) = ae^{-\Gamma t}, \qquad g(t) = ae^{t^{\delta}} \tag{5.16}$$

where a, Γ and δ are free parameters. We fit the functions from a certain cutoff, representing the time at which we presume the system to be safely in the self-similar scaling regime. The results of the fits bring a rather engaging notion into play. The inset of Fig. 5.9 (a) shows that the stretched exponential is a much better fit than a function with a constant decay rate $\Gamma = (0.0142 \pm 0.001)\frac{1}{t_s}$. Furthermore, Fig. 5.9 (b) strengthens this assumption, since it shows the natural logarithm of the data, giving us a pure power law with a rather good fit for the exponent

$$\delta = 0.311 \pm 0.004. \tag{5.17}$$

This result endorses the hypothesis that instantonic excitations in the system cause a coarsening slower than $\beta = 0.5$. In the present works of [48, 49], it was found that a sine-Gordon like model for multi-component Bose-gases would cause a coarsening of length scales with $\beta = 1/(d+2) = 1/3$ for $d = 1$ as in our case. Hence, should we be truly dealing with tunneling phenomena in a periodic potential as suggested in Fig. 3.3, this is exactly the behavior we would expect!

We may now also attempt to connect some length scale in the system to the coarsening dynamics. As mentioned before, the current j^1 allows us to identify domain walls within the system and thus gives us a powerful tool to investigate their statistics. The current peaks at the sites at which we observe a sharp change in the Larmor phase. The same method as used to create Fig. 5.9 can be used to extract the spatial distance between such domain walls. To this end we investigated once more the polar quench initial condition. By looking at slices of j^1 in time and space, one observes a strongly fluctuating data set with peaks reaching beyond the typical fluctuation threshold. By means of peak identification and the subsequent calculation of the distance between each peak and its next neighbor, we construct a histogram of the distance values, averaging over many truncated-Wigner realizations to get reliable statistics. In Fig. 5.10 we see the histogram as calculated for the polar quench. The probability distribution of the distances between the peaks shows a behavior which can be approximated by an exponential decay. We fit an exponential function

$$a \cdot e^{-r/\zeta}, \tag{5.18}$$

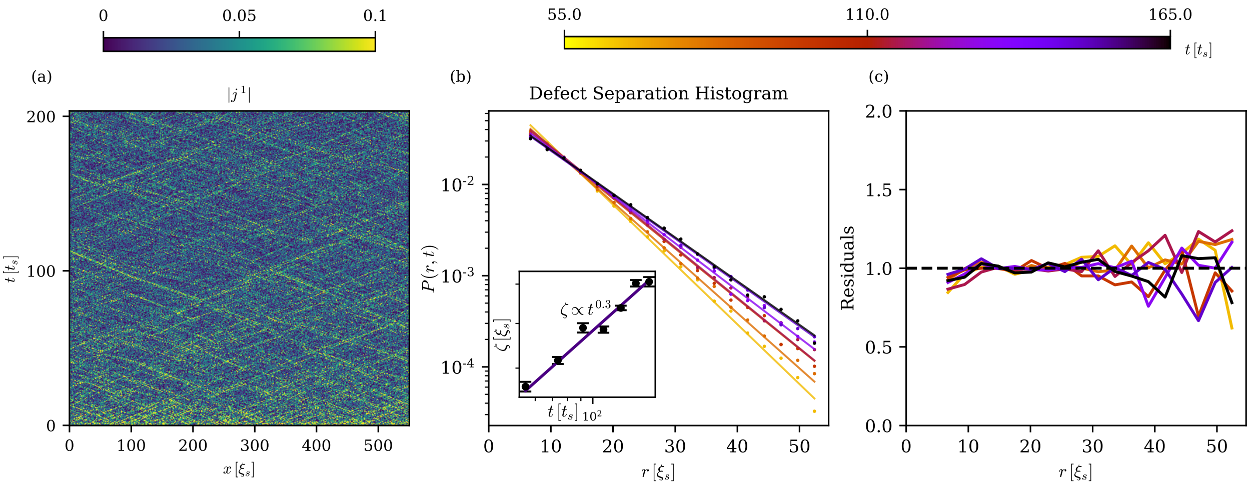

Figure 5.10: Defect distance analysis for the polar quench system. Panel (a) shows the absolute value of the topological current $j^1 = \partial^t \varphi_L$, which identifies the defects in the system. Panel (b) presents the histogram of relative distances between domain walls normalized to give a probability function on a linear-logarithmic scale. An exponential function $ae^{-r/\zeta}$ (solid lines) was fitted on the data (dots). The inset plot shows the changing length scale ζ with time on a double logarithmic scale. A power law $\zeta \propto t^\nu$ with a resulting $\nu = 0.30 \pm 0.04$ is found. (c) displays the residuals of the exponential fits to the data. At larger distances the error seems to grow, due to the finite statistics we can gather.

using a least-squares method. We define the free fit parameter $\zeta(t)$ as a mean separation scale. The suggestiveness of the definition is of course intentional. In Fig. 5.10 (b) we see that with increasing time the length scale governing the exponential decay changes and grows. In the inset of the figure we see the mean separation ζ as function of time in a double logarithmic scale. Clearly, it follows some power law $\zeta \propto t^\nu$. An additional least squares fit of a power law in time to the evolution of the mean separation shows that it grows with an exponent

$$\nu = 0.30 \pm 0.04, \tag{5.19}$$

which happens to coincide with the scaling of order parameter spectrum within the error bounds and the power law of the stretched exponential function describing the frequency of instantons in the system. We can thus summarize our analysis up to this point: after the quench, defects and textures in spin space appear in the system and begin to evolve with time. These defects or spin textures can be associated with a current j^1, which identifies domain walls between areas of rapidly changing Larmor phase. The mean separation of such defects or textures grows larger with time and thus causes the spectra of the transverse spin structure factor to scale with the same behavior, since the latter is governed by dominant length scales in the system. As argued in [28], for a two-dimensional XY model such length scales are given by the mean separation of vortices. In our case we may have associated a length scale to the mean separation of space-time vortices.

5.3 Rotations in Spin Space

In the previous sections, we have discussed the dynamics of the system under a quench from the polar phase to the easy-plane. The ensuing time evolution included the appearance of defects in the densities as well as the spin degree of freedom. We may now ask ourselves, how would writing in defects affect the system? This question is motivated by recent experiments conducted by the Oberthaler group in the Kirchoff Institute for Physics here in Heidelberg. Utilizing a clever array of lasers they have managed to write in solitonic defects in the system, characterized by a bright-dark-bright soliton in the densities [10]. Such solitonic excitations are characterized by a rise in density of the $m_f = \pm 1$ components and a dip in the $m_f = 0$ density accompanied by a phase jump of π. For more details about vector solitons in the density of the wave functions, I refer the reader to Ref. [50], which gives an excellent review of the subject. After writing in the defects in the polar phase, the system is then quenched into the easy-plane phase.

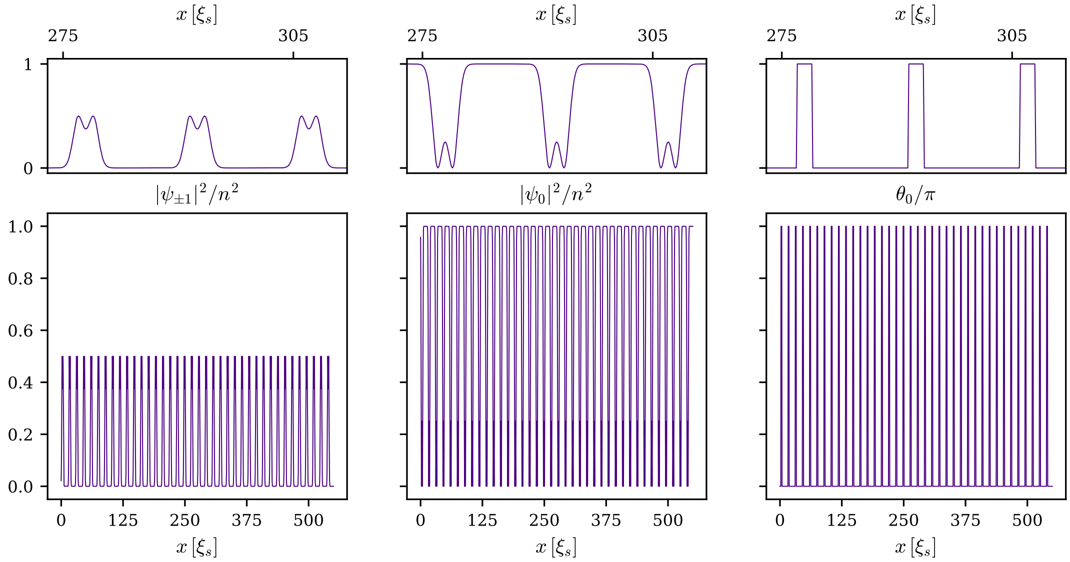

Figure 5.11: Exemplary initial condition for the case of 40 Rotations. The system is prepared in the polar phase with $N = 3 \cdot 10^6$, $L = 220\mu m$ and interactions of $|c_1/c_0| = 0.01$. The left column shows the density of the $m_f = \pm 1$ components, which are symmetric and can thus be plotted together. The central column displays the density of $m_f = 0$ component and the right column shows the complex phase of the $m_f = 0$ component, which we denote by θ_0. The bottom row shows the full grid, whereas the top row shows a zoomed in view of only a few defects.

The theory of experimentaly realizing the rotations in spin space is handled in Ref. [10]. Briefly, the experiment uses a steerable laser beam to coherently transfer atoms from the $m_f = 0$ component to the $m_f = \pm 1$ components via a position dependent Rabi coupling $\Omega(x)$. The Rabi oscillations will cause the wave function ψ_0 to acquire an amplitude $\psi_0 \propto \cos(\Omega t)$. Tuning the lighting time such that $\Omega t > \pi/2$, one acquires a minus sign in the wave function, thus inducing a phase jump of π as expected for a bright-dark-bright soliton. Following this procedure, we also imprint such defects in the condensate numerically. On a theoretical level the Gaussian laser beam profile induces a local rotation in spin space about an axis of our choice in the $F_x - F_y$ plane. For this we prepare the condensate in the polar phase and, for simplicity, rotate the spinor about the F_x axis according to

$$\psi \to \exp\left(-i\gamma f_x e^{-(x-x_i)/2\sigma^2}\right)\psi, \tag{5.20}$$

where once more f_x denotes the x spin matrix, γ is the rotation angle corresponding to Ωt, σ is the standard deviation of the Gaussian profile and x_i is the middle point of the i-th soliton. By applying these local rotations to the condensate, we will obtain a redistribution of spinor components with an amplitude and width given by a Gaussian. It is thus advantageous to choose the standard deviation of the Gaussian to be of the order of the spin healing length ξ_s. By probing different rotation angles, it was found that the wanted redistribution of populations accompanied by a phase jump are obtained by rotating by an angle $\gamma = \frac{2\pi}{3}$. An example of the results for 40 rotations on the initial condition is seen in Fig. 5.11 The local rotation creates a pair of kink and anti-kink which are characterized by a respective jump of π or $-\pi$ in the phase of the $m_f = 0$ component. These kinks and anti-kinks are accompanied by density dips and rises and will propagate in opposite directions in space, where they begin to interact with each other and other excitations to create a rich and interesting dynamic.

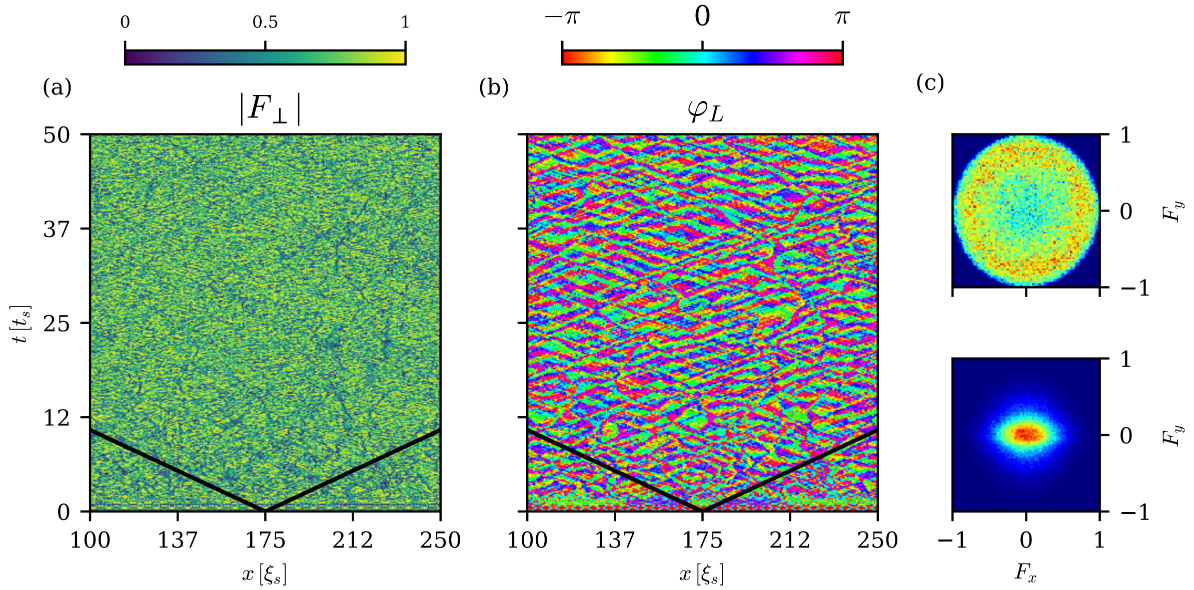

Figure 5.12: Zoomed in view of a single Trunacted Wigner realization of the condensate prepered in the polar phase with 80 local rotations, subsequently quenched to the easy-plane with $q_f = 0.9n|c_1|$. Simulation was preformed with a particle number of $N = 3 \cdot 10^6$, a physical length of $L = 220\mu m$ and interactions $|c_1/c_0| = 0.01$. (a): the transverse spin length. (b): the Larmor phase. The sound cone of the spin speed of sound $c_s = \sqrt{n|c_1|}$ ist plotted as solid black lines. (c): Spin histograms for times $t = 0$ (bottom) and $t = 160t_s$ (top).

Once more, a truncated Wigner simulation with periodic boundary conditions was made using the same parameters of the polar quench system, i.e. a quench to $q_f = 0.9n|c_1|$ of a system with a particle number of $N = 3 \cdot 10^6$, distributed on a physical length corresponding to $L = 220\mu m$ and the interactions strengths are given by $|c_1/c_0| = 0.01$. A total of 80 local rotations with a width of about $1.5\xi_s$, corresponding to 160 kinks and anti-kinks, were imprinted unto the initial condition. We integrate up to $t = 200t_s$ and observe the dynamics of the system. The condensate's behavior is qualitatively very different from what we investigated in section 5.1. The first obvious difference is observed in the spin histograms in Fig. 5.12 (c). The ring structure is all but gone and instead of obtaining a restriction to the topological space S^1 in the spin degree of freedom, we "fill up" the circle, implying large fluctuations of the transverse spin length. Indeed should we look at the F_z dynamics, we will see that these defects we have written in to our system force the dynamics out of $F_x - F_y$ plane and into the entire spin sphere as seen in Fig . 5.13.

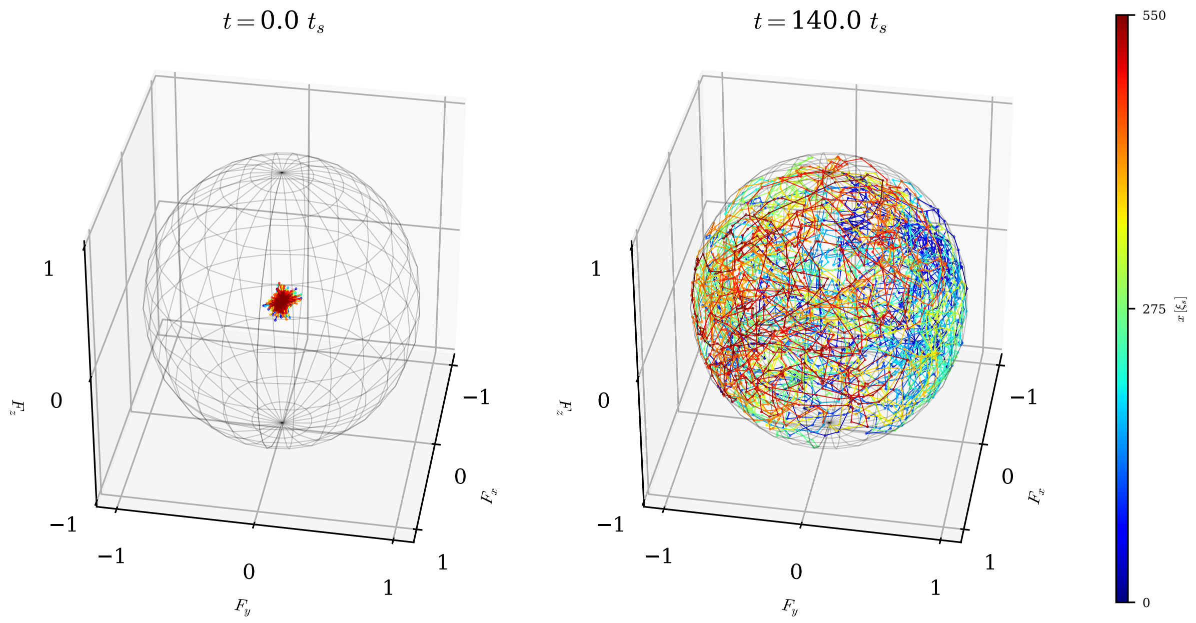

Figure 5.13: A single trajectory on the spin sphere for two different times in the dynamics of an initial condition with 80 local rotations. The color coding goes from one end of the spatial grid to the other. The strong fluctuations in spin space are seen along the entire sphere.

Furthermore, the space-time evolution of the spin length and its phase confirm the rather erratic dynamics we see in the histograms. Dips in the mean spin length are bountiful and propagate through the system in a quasi-particle-like manner. These propagating deep dips in the spin length correspond to phase kinks in the Larmor phase as well. In the Larmor phase we see and overlay of different kinds of kinks, defects and textures. We identify the phase kinks with the dark soliton-like spin length dips and also recognize the spin textures propagating with approximately the spin speed of sound in the system. The coarsening dynamics of the system seem to be less obvious in this setup, but one still sees that the length scale of the spin textures in the Larmor phase is slowly growing in time.

5.3.1 Spectra and Scaling

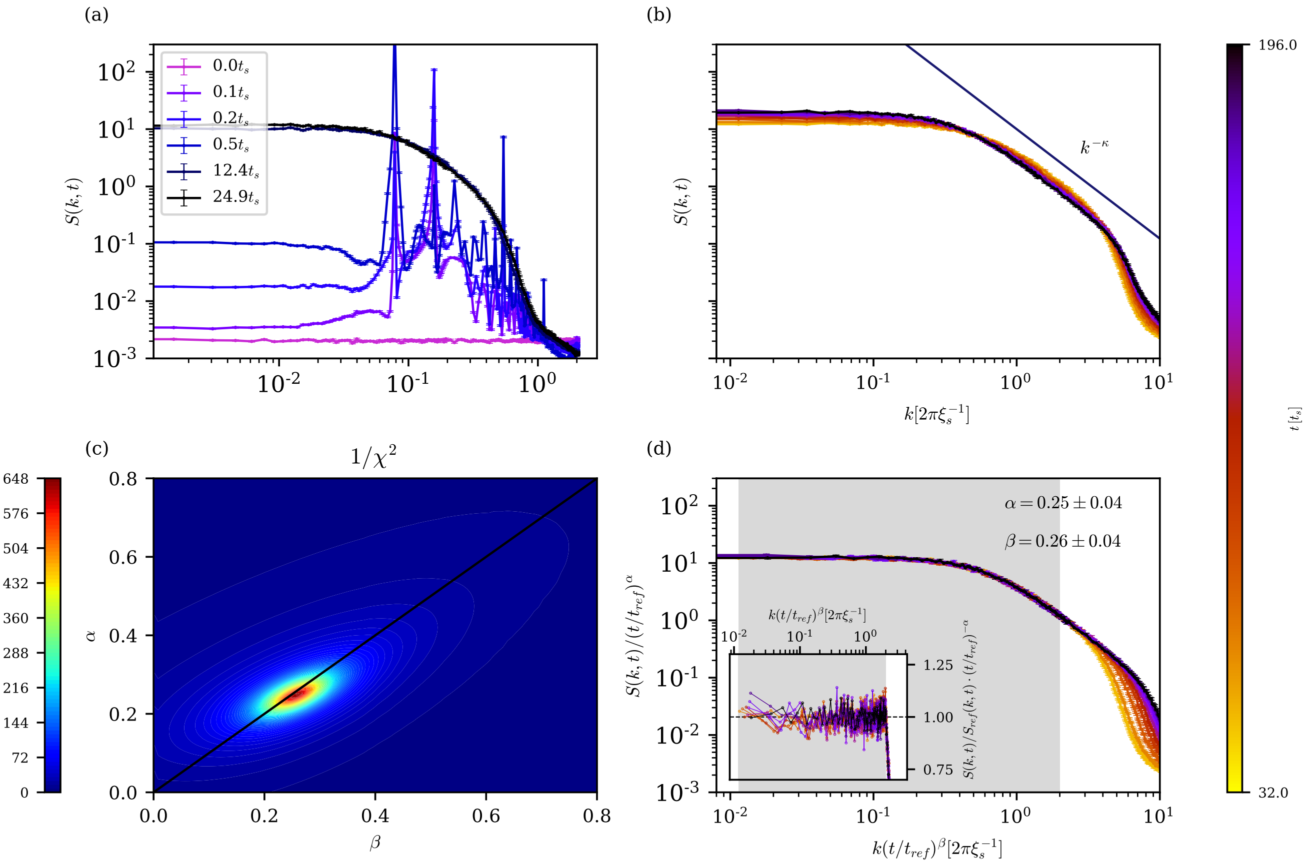

Figure 5.14: Self-similar time evolution of the transverse spin structure factor $S(k,t) = \left\langle |F_{\perp}(k,t)|^2 \right\rangle$. Panel (a) presents the short-time evolution of the spectrum, as the written-in defects give rise to an extreme over-occupation of certain modes. Panel (b) shows the raw spectra at times between $t = 32t_s$ and $t = 196t_s$. As a visual aid, a power law of k^{-2} was plotted. In panel (c) we see a contour plot of the inverse cumulative error $1/\chi^2$ of the rescaling algorithm as a function of α and β. Panel (d) displays the rescaled spectra with $\alpha = 0.25 \pm 0.04$ and $\beta = 0.26 \pm 0.04$. The inset presents the residuals of the rescaled spectra from the reference spectrum. The spectra were averaged over $\sim 10^3$ truncated Wigner realizations of a BEC with $N = 3 \cdot 10^6$, on a physical length $L = 220\mu m$, with interactions $|c_1/c_0| = 0.01$, quenched from the polar phase with 80 rotations imprinted on the initial condition to the easy-plane with $q_f = 0.9n|c_1|$.

As before, in our study of the polar quench, our main goal is the quantitative investigation of the time evolution of the condensate with regards to self-similar scaling, associated with the NTFP. The question arises if the different initial condition leads to a different scaling behavior, and if so, what are the differences between the two dynamical behaviors. This is once more motivated by the findings by the BEC lab in Heidelberg, in which two different sets of scaling exponents were found: one for the polar quench and one for the rotation initial condition [14].

To investigate the scaling behavior, we once more turn our attention to the calculation of the correlations of order parameter of the system. Since we remain in the easy-plane phase, the order parameter should still be the transverse spin. We thus calculate the transverse spin structure factor. This time, the initial evolution of the structure factor is somewhat different than in the polar quench, as seen in Fig. 5.14 (a). At first, we observe an extreme over-occupation of some modes, as the periodic structure of writing in local rotations at a constant distance from each other gives rise to these modes. During the short-time evolution of the spectrum, we identify that the over-occupied modes flatten with time as other unstable modes corresponding to the respective Bogoliubov modes are being occupied instead. After a short period of about $t \approx 12t_s$, the scaling function begins to take its form and the system enters the scaling regime at arround $t \approx 25t_s$. After investigating the short-time evolution of the system, we may turn our focus to the self-similar scaling regime and its resulting scaling behavior. The results can be seen in Fig. 5.14 (b)-(d).

The scaling function itself seems to have shifted and a much more present plateau is seen. Furthermore, the power law in the infrared seems to have shortened considerably. Whether or not this constitutes a new universal scaling function is a matter of current discussion. Nevertheless, the scaling exponents themselves remain the same within the error bounds of the polar quench system. They even seem to be more accurately determined, since a more pronounced plateau helps the rescaling algorithm to constrain α. The residuals of the rescaled spectra confirm that the rescaling itself was successful and the shape of the spectrum does not change significantly over the integrated time span. Furthermore, the contour plot shows the certainty of the scaling exponents to mainly be positioned on the $\alpha = \beta$ line.

It thus seems that although we have changed the initial condition significantly, we have not changed the scaling behavior of the system in the vicinity of the NTFP. Whether this result is fortunate or not, is a question left for further discussion. We can look at this result in two ways: on one hand, we may have shown the robustness of a universal NTFP. We have created two significantly different initial conditions which both scale with the same universal scaling exponents, thus strengthening the notion of universal scaling far-from equilibrium. Furthermore, the scaling exponents $\alpha = \beta \approx 1/4$ are obtained both numerically and experimentally for the rotation initial condition. On the other hand, we see a certain discrepancy with the experimental data. Experiments have shown that a polar quench leads to a scaling behavior of $\alpha = \beta \approx 1/2$ [7] and that the rotation initial condition leads to a slowing down of scaling to $\alpha = \beta \approx 1/4$ [14]. Thus, one would expect this slowing down to also happen in this case. The discussion of the numerical results in comparison to the experimental results and the questions rising from it is the subject of chapter 6.

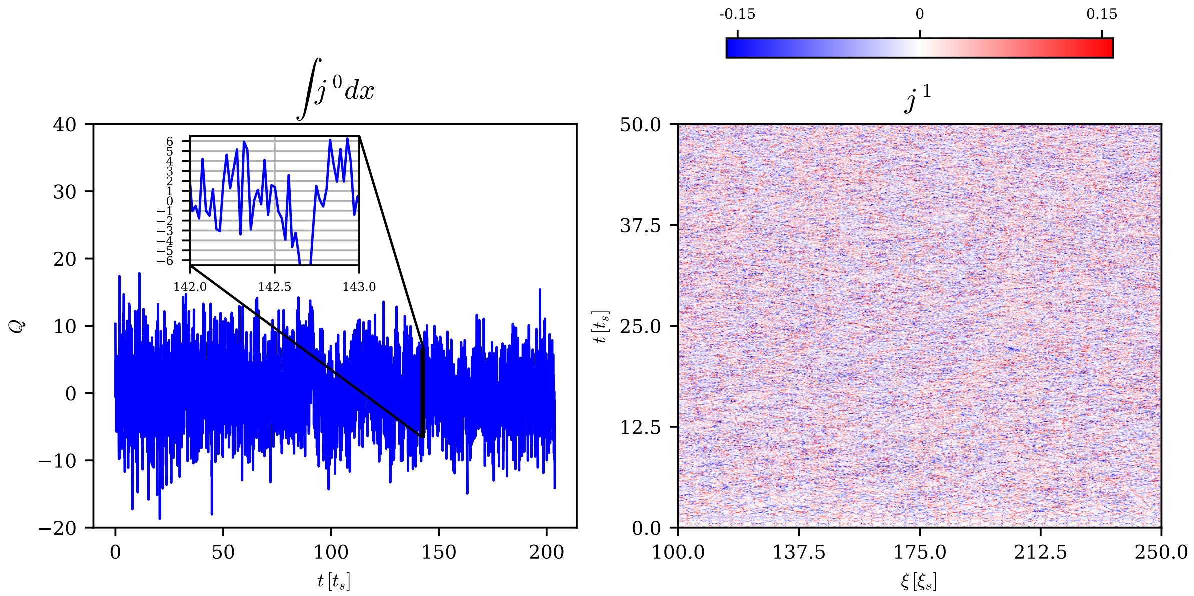

Figure 5.15: Winding number and topological current for an initial condition with 80 rotations. The disappearance of clear signals in the winding number and the noisy erratic structure in the topological current are apparent.

5.3.2 Disappearance of Topological Charges

The defects we have written into our systems seem to be the cause of chaotic behavior in our system. The spatial density of these defects raises the question if one can even talk about them being defects. Fig 5.11 shows us the initial condition for 40 rotations, yet the calculation of the spectra was made with a system with 80 rotations in the initial condition. Even in the case of 40 rotations we already see that one can only talk about these objects as a deviation from the mean field ground state densities, but if it is not a priori clear what the mean density should be and the fluctuations are on the order of the mean itself, we do not know how the system will behave. One thing is very clear: the inclusion of dynamics in all directions on the spin sphere washes away any clear sign of topological objects. This is not to say they do not exist in the background, but their detection is obstructed by a largely fluctuating system.

As shown in Fig. 5.15, the previously detected clear integer winding numbers are not seen anymore as the phase gradient seems to fluctuate excessively as well. As a possible explanation for this behavior, we can consider the fact that by including dynamics in the F_z direction, we have increased the dimension of the order parameter manifold from S^1 to S^2, leaving the homotopy group $\pi_1(S^2) = 0$ to be the trivial group. This imples that the Larmor phase can no longer be seen as the relevant degree of freedom and any sort of excitation in the Larmor phase could be continuously deformed back to the ground state, thus topologically trivializing the setup. The interpretation of the results we have obtained from the spectra is thus left somewhat unclear. Nevertheless, we can argue that, as seen in Fig. 5.12, we observe the chaotic noisy behavior of the system, yet in the Larmor phase one can still recognize the structures also seen in Fig. 5.2. The large fluctuations in the transverse spin length seem to not have an effect on the underlying coarsening effects of the system in the long-time evolution of the spectra. This could reflect the instability of vector solitons in the condensate, as investigated by Ref. [51]. More on this in section 6.2.

6. Comparison with Experiment

Needless to say, physics does not only live on paper or on our personal computers. Instead, it is our duty as physicists to verify predictions with experiments. During the course of the research for this thesis, the close collaboration with the BEC laboratory has led to the deep and thorough investigation of the system, in order to better understand and interpret the experimental results obtained in the few years predating this thesis. The experimental search for NTFP in the spinor BEC has led to some interesting developments in the field and the exchange between experiment and theory is crucial for the progress in the search for universal dynamics far from equilibrium [6, 7, 10]. In various parts in our previous discussions, we have mentioned the experiment and the resulting motivation to investigate the theoretical aspect of the different systems. In this chapter, we will explicitly discuss the numerical results with regard to experimental results found to the date of writing this thesis. No strict quantitative comparison will be made in this chapter, yet the efforts to better understand the system come mainly from the need to explain differences between numerics and experiment. First, we will discuss the discrepancies between numerical results and experiment. Then, in section 6.1 we will discuss the argument of the effect of dimensionality on the results. We give an argument to the discrepancy associated with the effect the transverse directions of the experimental trap has on the dynamics. We simulate a full three-dimensional simulation to investigate this claim. Following this attempt, in section 6.2, we consider that technical limitations in the experiment result in uncertainties in the value of q_f. Therefore, an investigation of the dependency of the scaling behavior on q_f may provide a possible explanation for discrepancies.

The main background of this project dates back to an experiment conducted in 2018 [7], where it was found that after a quench from the polar phase to the easy-plane phase, the system exhibits self-similar scaling corresponding to the universal exponent

$$\alpha_1 = 0.33 \pm 0.08, \quad \beta_1 = 0.54 \pm 0.06. \tag{6.1}$$

Recently, newly performed experiments done with writing in defects into the system using local rotations [14] show a qualitatively different System and a new set of universal scaling exponents

$$\alpha_2 \approx \beta_2 \approx \frac{1}{4}. \tag{6.2}$$

Thus, the search began to explain the differences of both systems. Are the rotated defects in the initial condition responsible for the anomalous scaling? what is their structure? Has the universality class of $\alpha = \beta = 1/4$ been experimentally proven? Moreover, is this a different universality class than that found in the polar quench? The theoretical simulations we have discussed up until now have shown only the scaling behavior $\alpha = \beta = 1/4$ and no other dynamics were detected. In the coming sections we discuss some arguments which were given to explain this discrepancy.

6.1 Dimensionality Argument

The discrepancy between numerics and the experiment is clear. Where the experiment sees a scaling with exponents close to 1/2, the numerics see a clear scaling with exponents near 1/4. A possible and rather popular explanation was given by the failure of the pure one-dimensional GPEs to account for the transverse directions and their effects as in the experiment [5]. It is important to note that the conducted experiment utilized a harmonic trap with frequencies $\omega_x = 1.6\text{Hz}$ and $\omega_y = \omega_z = 100\omega_x$. Should we calculate the oscillator length for this system we arrive at a value which is about ten times larger than the density healing length ξ, yet smaller than the spin healing length ξ_s. This implies the system is quasi one-dimensional in the spin degree of freedom, yet anisotropically three-dimensional in the densities. It was thus argued that due to these technical limitations and construction of the trap, the resulting dynamics may be altered by dimensionality, i.e. the offset from a true one-dimensional system. We know from kinetic theories of self-similar scaling dynamics far-from-equilibrium that the dimensionality of the system determines the scaling exponents of the NTFP [12, 13]. Therefore, it seems reasonable to assume the transverse directions which were not accounted for in the pure one-dimensional simulations can cause such discrepancies in the results.

Another important aspect connecting to dimensionality is that of the homotopy groups and topological defects. The argument of dimensionality may cause the topological objects which arise in the pure one-dimensional case to be no longer valid, as the homotopy groups, and with them the homotopy classes, change. In other words, we expect the dimensionality of the system to no longer accommodate for the same topological objects which caused scaling with $\alpha = \beta = 1/4$.

In order to investigate this claim, we have also computed a fully three dimensional simulation with the experimental parameters. With the aim to achieve a simulation resembling the experiment as closely as possible, the unique cylinder trap geometry of the experiment was

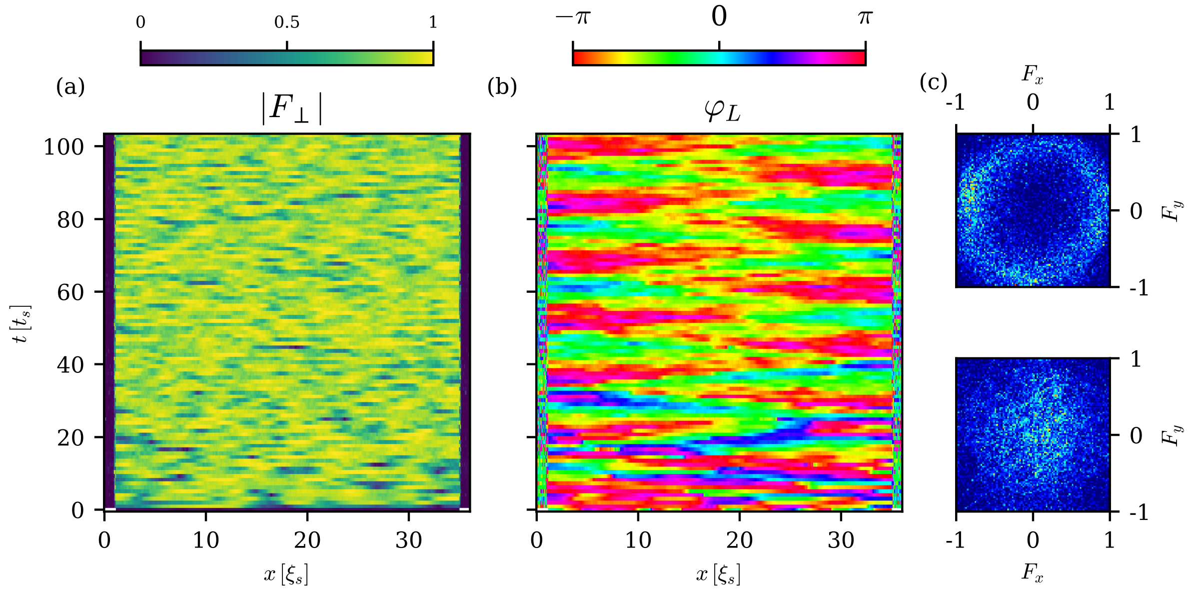

Figure 6.1: Space-time evolution of the transverse spin $F_\perp = |F_\perp|e^{i\varphi_L}$ in a single truncated Wigner realization after a quench from the polar phase to the easy-plane phase with $q_f = 0.5n_p|c_1|$. The system is initialy prepared in a cylinder trap in a three-dimensional setting in the polar phase with a particle number of $N = 1 \cdot 10^5$, a physical length of $L = 180\mu m$ and interactions $|c_1/c_0| \approx 0.005$. The resulting dynamics were integrated over the transverse directions to give an effective one-dimensional system. Panels (a) and (b) show the transverse spin length and its phase respectively. Panel (c) shows the histograms in spin space in $t = 0$ (bottom) and $t = 80t_s$ (top).

implemented: a box shaped trap in the longitudinal direction x and harmonic in the transverse directions y, z. This was done by implementing a continuous box function in the longitudinal direction in the potential term, making sure the amplitudes and size of the box prevent any unwanted tunneling effects. For the simulation we used a grid of $512 \times 32 \times 32$ grid points with $N = 1 \cdot 10^5$ particles distributed over a physical length of $L_x = 180\mu m$. The grid spacing is set by the grid length in the longitudinal direction and thus the physical lengths in the transverse directions may be obtained by considering Δx_g alone. The trap frequencies were chosen to correspond to the experimental setting, i.e. $\omega_x = 1.6$Hz and $\omega_y = \omega_z = 100\omega_x$, with a longitudinal trap size of $d = 168.75\mu m$. The spin and density coupling strengths were set to the known ^{87}Rb values and the system was quenched to a quadratic Zeeman strength of $q_f = 0.5n_p|c_1|$, where n_p denotes the peak density of the condensate.

The time evolution was integrated over $t = 50$s, corresponding to $t \approx 100t_s$, where now t_s is defined w.r.t the peak density $t_s = 2\pi/(n_p|c_1|)$. Notice that due to the inhomogeniety caused by the trap in the transverse directions, we must take into account how the length, energy and time scales (governed all by $n|c_1|$) change locally. This means that we work with the scale given by the peak density n_p, as this will be the shortest of all the scales. For the implementation of the truncated Wigner noise in a trapped setting, I refer the reader to the works of [24] for setting noise in a harmonic trap. In this case, we must change the solution in the longitudinal direction from the solution of the harmonic oscillator, to that of a particle in a box to occupy the correct modes with quantum noise.

In order to evaluate the three dimensional data as a quasi one-dimensional gas, we integrate over the transverse directions and leave only the longitudinal direction. The space-time evolution of the three-dimensional system is seen in Fig. 6.1. We observe a qualitatively similar behavior to that of Fig. 5.2 in the transverse spin length and Larmor phase, as some Larmor phase domains appear in the system. Notice that the temporal resolution of the simulation was reduced to accommodate for the large data volume. One can recognize the trap borders and it seems no tunneling effects can be seen. The spin Histograms also give us the desired ring structure as in the pure one dimensional case.

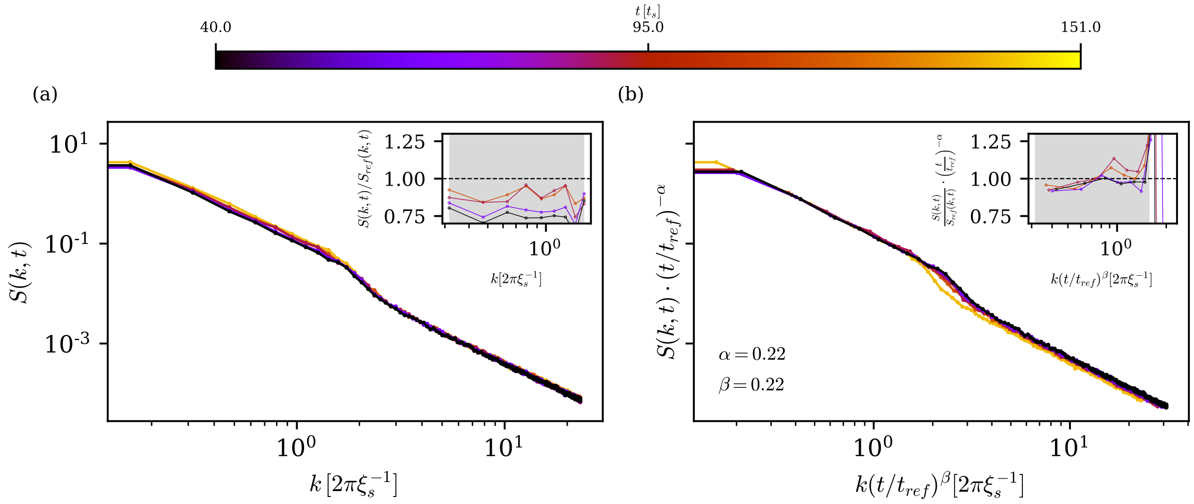

Figure 6.2: Spectrum of the transverse spin structure factor in the self-similar scaling regime of a three-dimensional simulation in a cylinder trap. The system was prepared to resemble the experimental setup in the polar phase with $N = 1 \cdot 10^5$, $L = 180\mu m$ with a trap size of $d = 168.75\mu m$, interaction strengths $|c_1/c_0| \approx 0.05$ and was subsequently quenched to $q_f = 0.5 n_p |c_1|$. The spectra were averaged over the transverse directions and only analyzed within the box shaped trap in the longitudinal direction. Panel (a) shows the unscaled raw spectra and their deviation from the reference spectrum in the inset. Panel (b) displays the manually rescaled spectra with $\alpha = \beta = 0.22$. The inset shows the residuals w.r.t the reference spectrum. After rescaling the curves seem to show a much lower deviation.

We now turn to the calculated spectra as seen in Fig 6.2. We calculate the spectrum only within the trap borders and we observe once more a power law of $\kappa \approx -2$ which scales with time. Unfortunetely, the rescaling algorithm has difficulties rescaling the spectra with two exponents given only a power law present and no plateau to constrain α. Rescaling done by hand with $\alpha = \beta = 0.22$ gives a rather satisfactory overlap of the spectra into one curve, as seen by the residual plots in the insets of Fig. 6.2. Before scaling, the residuals deviate significantly from the optimal value of 1. After rescaling the spectra, we identify an acceptable overlap of the residuals. Plugging in $\alpha = \beta = 0.5$ or the experimental values in Eq. (6.1) would cause the curves to overshoot. Thus, we may carefully assume the transverse directions and dynamics have not had such a dramatic effect on the scaling behavior of our system.

At this stage, I would like to point out some caveats of the three-dimensional simulations. In order to be able to fully confirm or falsify the effect of the transverse directions, one must investigate many different grid configurations to avoid any finite size effects caused by a small grid in the transverse directions. Furthermore, the existence of a trap in this setting will cause the simulation to calculate many low occupation modes on the grid. As mentioned in section 4.2, the TWA is a good approximation of the system in the limit of high occupations. Hence, the dynamics may be falsified by regions of lower occupations caused by the inhomogeniety of the trap. We must also note that we are dealing with very long integration times with about $\sim 10^6$ time-steps, where we gather an error of $(\Delta t)^3$ in each step, hence accumulating a potentially large error that can render the results unreliable in this setting. A more thorough inspection of this three-dimensional setup is advisable, as it would surely yield interesting results. A further solution to the uncertainty of the three-dimensional simulation could be the use of the non-polynomial Schördinger equations (NPSE) as outlined in Ref. [24]. The idea behind the NPSE is the inclusion of dynamics in the transverse directions in a pure one-dimensional EOM. This can be used to reduce the amount of low occupied modes in the simulation and obtain a better approximation of experimental results.

The question seems to remain and endure: why is the experiment seeing different scaling exponents than the numerics? An idea rose, as the inhomogeneity of the system implies that, given a fixed value for the quadratic Zeeman effect, different points in the cloud experience a different q with respects to the local density, which is the crucial value for the QPT from the polar phase to the easy-plane phase. A change of local density can thus shift the whereabouts of the condensate in the $c_1 - q$ plane, drawing the condensate either closer or further to the quantum phase transitions.

6.2 q-Dependency of Scaling Exponents

After searching for the culprit of the discrepancy between experiment and theory in the transverse directions and dimensionality of the trap, we may turn our attention to another potential argument: a NTFP is associated with a specific Hamiltonian, corresponding to a specific setting of the parameters in Eq. (2.4). The Spin-1 Hamiltonian in our case has an external parameter attached to a single-particle operator: the quadratic Zeeman shift q. Does changing q_f have an effect on the dynamics after a quench? Recent developments in the experiment led us to believe that the experimental value of q_f could have a rather large uncertainty and may fluctuate more than previously thought. The determination of the experimental value of q_f is a rather difficult task, as also particle loss in the trap may lead to a shift of the effective q_f w.r.t the density of the cloud. Could a change in the value of q_f have an effect on the scaling?

What began as a thought about the effects a different q would have due to the inhomogeniety of the condensate led to a study of an homogeneous system going through different parameter quenches to many different q_f values. We remind the reader once more that at a critical $\tilde{q} = 2n|c_1|$, a QPT takes place from the polar phase, characterized by a vanishing spin length and an occupation of solely the $m_f = 0$ mode, to the easy-plane phase, characterized by a non-vanishing transverse spin length and occupation of all components of the condensate. The notion of the clear borders between the different phases is applicable on the mean-field level, yet by adding quantum noise to the system we go beyond the mean-field description. This results in a "washing away" of a clear cut between the phases, and as one draws closer to the QPT from any direction, i.e. $q \to \tilde{q}$ or $q \to 0$, one could expect to move away from the characteristics of the easy-plane phase, e.g. gaining more dynamics in the F_z direction directly as we draw closer to the ferromagnetic phase.

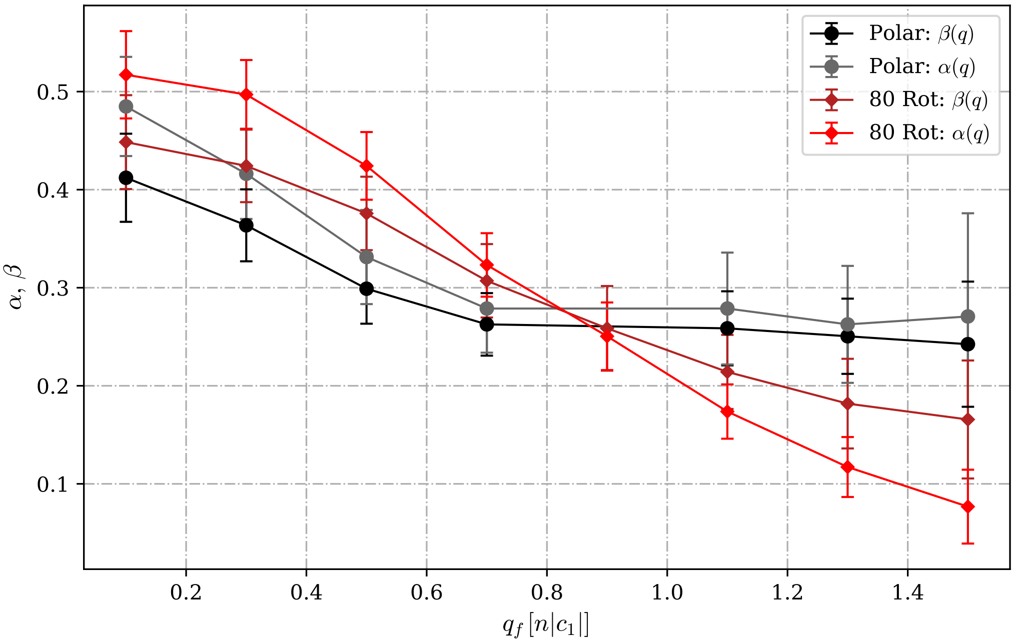

Figure 6.3: Dependency of the scaling exponents α and β on the final value of quadratic Zeeman effect q_f after a quench from the polar phase. All exponents were extracted by simulating a system with $N = 3 \cdot 10^6$, $L = 220\mu m$ and interactions strenghts $|c_1/c_0| = 0.01$. The red tinted curves show the development of the exponents with the rotation initial condition. The greyscale curves show the course of the scaling exponents for the polar quench. For the spectra of each data point see Appendix A

With that in mind, we investigated the behavior of the system after a quench from the polar phase to the easy-plane phase for a range of $q = 0.1n|c_1|$ to $q = 1.5n|c_1|$ in steps of $0.2n|c_1|$. The parameters of the simulation correspond to the same parameters of the simulation in the polar quench case discussed in section 5.1, meaning we set the particle number to $N = 3 \cdot 10^6$, the physical distance to $L = 220\mu m$ and interaction strength ration to $|c_1/c_0| = 0.01$. Furthermore, we also studied the effect the local rotations would have on the scaling exponents as a function of q_f. The results can be seen in Fig. 6.3. We observe a remarkable behavior of the system, and a careful interpretation is in order.

6.2.1 Polar Quench

Firstly, considering the polar quench case, for q_f far enough from any QPT we obtain the numerical scaling of $\alpha = \beta \approx 1/4$. Should we now venture forth to lower q_f values, we observe a rise in the value of the scaling exponents. The observant reader will also notice the values of α and β are drifting apart, thus implying the breaking down of the transverse spin quasi-particle conservation law we had previously seen. The signal is evident in the numerics: a faster coarsening in the system may be connected to a rather low q_f value in the system. The answer remains shrouded as to the cause of such an effect. To explain why the value of q_f should have such a dramatic effect on the scaling exponents, we turn once more to the concepts of topology: trying to identifying the objects in the system in analogy to our investigation of the system in section 5.1.3.

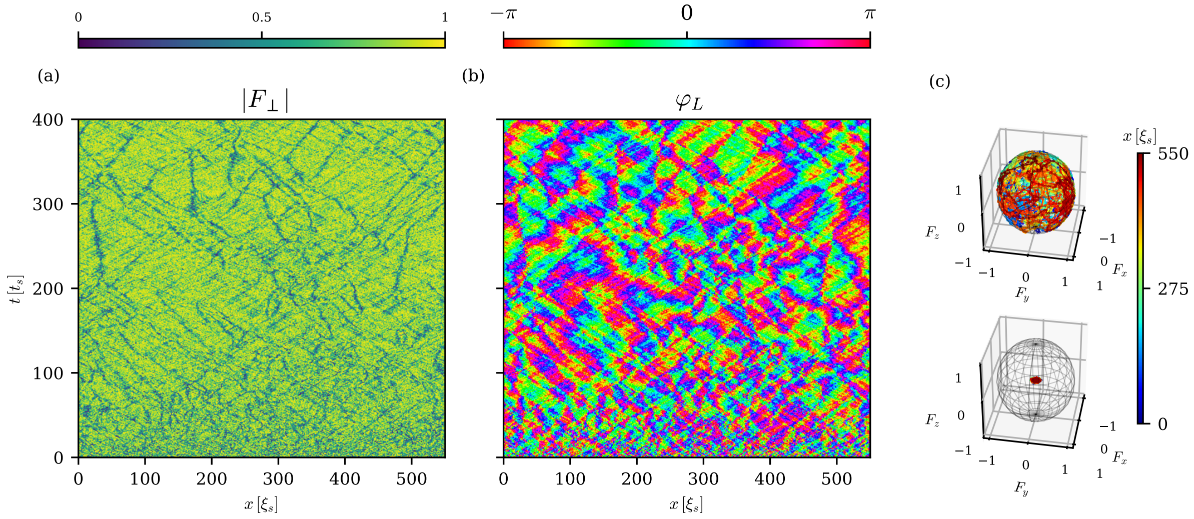

Figure 6.4: Space-time evolution of the transverse spin $F_\perp = |F_\perp|e^{i\varphi_L}$ in a single truncated Wigner realization after a quench from the polar phase to the easy-plane phase with $q_f = 0.1n|c_1|$. The system is initially prepared in the polar phase with a particle number of $N = 3 \cdot 10^6$, a physical length of $L = 220\mu m$ and interactions $|c_1/c_0| = 0.01$. Panels (a) and (b) show the transverse spin length and its phase respectively. Panel (c) shows single trajectories on the spin sphere for two different times: $t = 0$ (bottom) and $t = 160t_s$ (top).

In Fig. 6.4 we see the single realization of the system for a quench to $q_f = 0.1n|c_1|$. Immediately, one observes the qualitative difference between this system and the quench into the middle of the easy-plane, as given in Fig. 5.2. This time, we identify not only large phase fluctuations, but also very large fluctuations in the transverse spin length. These dips in the spin length coincide with jumps of π in the Larmor phase as we see a sort of dark spin soliton propagating through the system. It would be wrong to assume that the dynamics are restricted only to the $F_x - F_y$ plane, as evident by the filled up spin sphere in Fig. 6.4 (c).

The appearance of rich dynamics in the F_z direction is not a foreign concept for us. We have witnessed it also in the case of local rotations. The only difference is that these defects arise naturally in this case and are more sparse in the system, allowing us to inspect the system more closely. Since we are no longer restricted to the $F_x - F_y$ plane, the target manifold for our topological objects has changed from S^1 to S^2, the surface of the unit sphere. Since we are in a one dimensional setting, this would mean we would be looking for $\pi_1(S^2) = 0$, i.e. the trivial homotopy group. If we would calculate the topological charge as previously done, we would not obtain any stable charge. These objects are higher dimensional objects which are not protected by any conservation law, as they come and go. Nevertheless, it appears they dominate the dynamics of the system, whereas the instantonic excitations, whilst presumably still present, are not. In a long time simulation one observes the relaxation of the F_z dynamics and the well-known structure of the instantonic excitations regains its form. Sadly, this is after the system has left the hypothesized scaling regime.

Thus, we are now left with trying to obtain more intuition as to what is coarsening in the system. In analogy to our previous analysis of the defects we investigate the correlation of transverse spin length dips and Larmor phase jumps. We define a new current

$$j(x,t) = \Big(\langle |F_\perp| \rangle_x (t) - |F_\perp|(x,t) \Big) \cdot \partial_x \varphi_L(x,t), \tag{6.3}$$

where $\langle |F_\perp| \rangle_x$ is the spatial average of the spin length at each time.

In Fig. 6.5 (a) we see the above defined current as a function of space and time. We observe the correspondance of a strong signal in the current j to the dips and phase kinks we identify in Fig. 6.4. Naturally, the current was constructed this way, since these defects are comprised of a dip in the transverse spin length, which will cause a signal in $\langle |F_\perp| \rangle (t) - |F_\perp(x,t)|$, and a jump in the Larmor phase, which will create a signal in $\partial_x \varphi_L(x,t)$. Once more, in analogy to section 5.1.3, we utilize peak identification algorithms to calculate the relative distance r between the defects at each time. We then record these distances in a histogram, averaging over many truncated Wigner trajectories. The results can be seen in Fig. 6.5 (b). Once more, we observe an exponential decay in probability of defect separation occurrence. Using a least-squares method, we fit an exponential function $a \cdot e^{-r/\zeta}$ with a characteristic length scale ζ, which as we see from the fits seems to grow in time, obeying a power law with an exponent of

$$\nu' = 0.44 \pm 0.01. \tag{6.4}$$

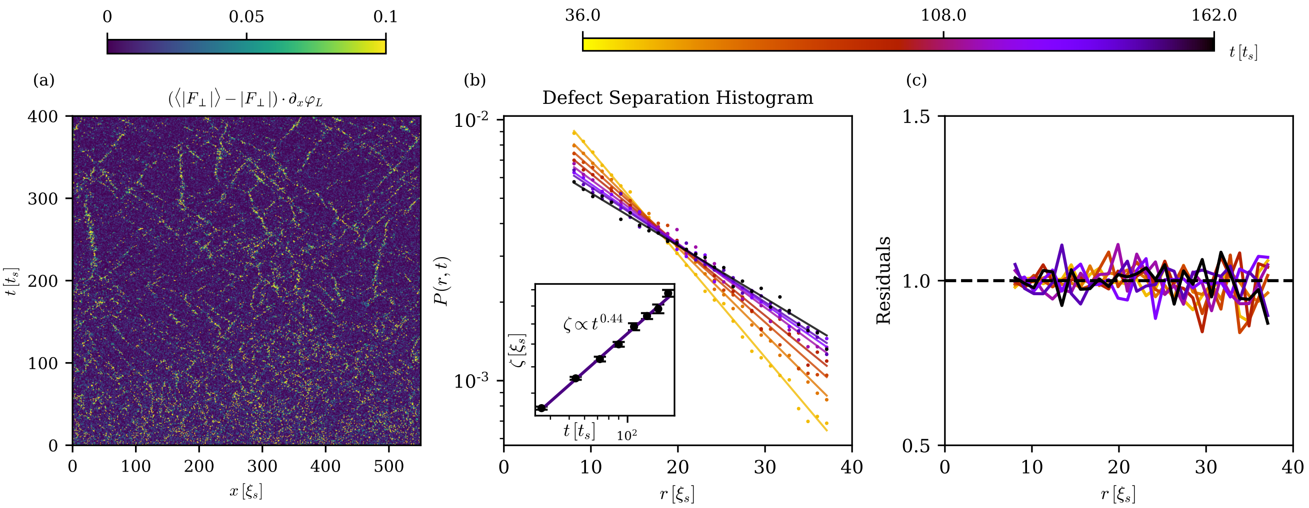

Figure 6.5: (a): Space-time evolution of the current j after a quench from the polar phase to the easy-plane phase with $q_f = 0.1n|c_1|$. (b): Histogram of relative distances between the defects which were defined as peaks of the current j on a linear-logarithmic scale. Exponential functions $ae^{-r/\zeta}$ (solid lines) were fitted onto the data (dots) in several times. The inset shows how the length scale set by ζ changes with time on a double logarithmic scale. The length scale follows a power law in time with $\zeta \propto t^{\nu'}$, with $\nu' = 0.44 \pm 0.01$. (c): Residuals of the exponential fit for different times. Due to the clear signals arising from j, better statistics were gathered even for large distances and low probabilities, thus rendering the exponential fit more successful.

This seems to coincide with the scaling of the power spectrum for the same q_f value within the error bounds. The same process can be applied to the different q_f values, yet as we quench further away from $q = 0$, the F_z excitations corresponding to dips in $|F_\perp|$ and jumps in the Larmor phase become less and less dominant and their identification with the current j becomes more and more difficult, thus rendering the peak identification rather unreliable.

What we have studied in this section up until now, was the rather continuous change of the scaling exponents depending on the final quadratic Zeeman coupling of the parameter quench. It is thus puzzling that one would speak of universal dynamics in this context, if one could always reach a continuous spectrum of scaling exponents. The argument we give in this thesis is that we may be observing two NTFP, which are competing against each other. These two NTFP correspond to the different behavior of the defects or excitations propagating through the system. On one hand, we have the instantonic excitations that we have identified in the polar quench into the middle of the easy-plane, which may be responsible for the coarsening of the system with $\alpha = \beta \approx 1/4$. On the other hand, we have the F_z excitations with a jump in the Larmor phase and dip in the transverse spin length, which can also be seen as dark soliton-like excitations in the transverse spin. These excitations seem to cause a scaling with larger exponents reaching $\beta \approx 1/2$. Either way, it is clear that by steering away from the middle of the easy-plane, we exit the regime in which the dominant degree of freedom is the Larmor phase living on S^1.

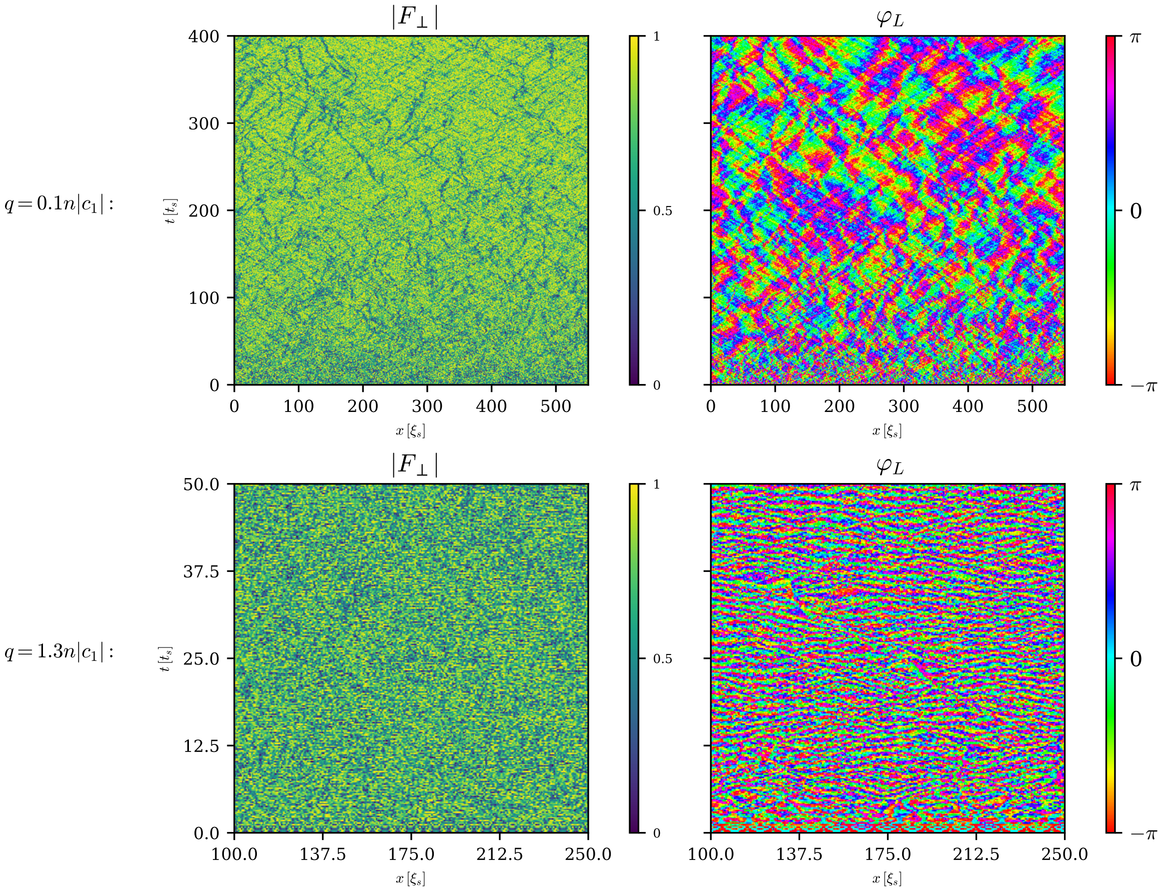

Figure 6.6: Space-time evolution of the transverse spin given by a single truncated Wigner trajectory of the 80 rotations initial condition. The upper row shows the quench to $q_f = 0.1n|c_1|$ and the full time evolution. The lower row shows a zoomed-in view of the beginning of the evolution after the quench to $q_f = 1.3n|c_1|$. Both systems were simulated with a particle number $N = 3 \cdot 10^6$ distributed over a physical length of $L = 220\mu m$ with interactions $|c_1/c_0| = 0.01$.

6.2.2 Local Rotations

As seen in Fig. 6.3, the curve for the case of inserting local rotations in the initial preparation of the system behaves differently than the curve for the polar quench alone. For low q_f values, the scaling exponents seem to coincide within their respective errors, yet with a tendency to larger exponents. The two curves appear to intersect in the middle of the easy-plane, and thereupon the curve for local rotations continues to lower and lower exponents. We might ask ourselves what is the difference between the respective systems? Once more the main thought is which kind of excitations dominate the time evolution of the length scales in the system. In the polar quench case, we have argued that for low q_f values, the F_z excitations dominate and show a different scaling behavior as before. The proximity to the QPT towards the strict ferromagnetic phase must have some sort of effect on their behavior and energetic favorability.

Fig. 6.6 shows the time evolution of the rotation initial condition under two different quenches: the top row shows a quench to $q_f = 0.1n|c_1|$, whereas the bottom row shows a zoomed-in view of the first $50t_s$ of the time evolution after a quench to $q_0 = 1.3n|c_1|$. For the former it seems the excitations we wrote in the system have no real effect on the system in the long time evolution. The proximity to the ferromagnetic phase seems to favor the F_z excitations and they appear to dominate the system as in the polar quench case. This also implies that the written-in defects using local rotations are not the same objects as the ones arising organically from the quench to a lower q_f. The situation seems to be different for the case of larger q_f values. In the same figure, we also observe the time evolution for $q_f = 1.3n|c_1|$. Since the dynamics are chaotic and the structures arising are very fine, we only look at a zoomed-in cutout of the system to better resolve it. The structure in the system appears to be rather static, or at least evolve extremely slowly, as supported by the slow scaling of the spectra (see Fig. 6.3). One might get the impression that for large enough q_f values these written-in defects are energetically favorable and seem to stay in the system, thus obstructing scaling phenomena.

One possible argument to this striking difference is the interaction of the written defects with the dynamical instabilities caused by the respective Bogoliubov modes. As we know from Bogoliubov theory, the dispersion relation gives us a spectrum of unstable modes, where the most negative mode is the most unstable. The value of this most unstable mode depends on the value of q according to

$$k_{mu} = \begin{cases} 0, & \text{for} \quad 0 < q < n|c_1| \\ \sqrt{-2(q + nc_1)}, & \text{for} \quad n|c_1| < q < 2n|c_1|. \end{cases} \tag{6.5}$$

Writing in this periodic structure of defects in the system causes an extreme over-occupation of a mode regime. Hence, according to the spectrum of unstable modes, the initial growth rate of these modes depends on the value of the quadratic Zeeman effect. Therefore, we might state that depending on q_f we have excited more or less stable modes which cause the defects to either stay in the system or decay rather quickly, whilst the unstable modes cause other excitations to dominate. This point of view is only qualitative, since the high fluctuations in the mode occupations contradict the underlying assumption for the validity of Bogoliubov theory. Nevertheless, we expect the very-short-time behavior of the system to be qualitatively adequately described by this behavior.

Fig. 6.7 helps us make this argument more plausible. The figures showing the short-time evolution of the polar quench help us gain intuition as to the unstable modes in the system and the distinct dynamics of instabilities according to the value of q_f, as the populations of the respective modes behave quite differently. The consequences for the short-time evolution of the local rotation initial condition can be argued for the case of $q_f = 01.n|c_1|$: The lower

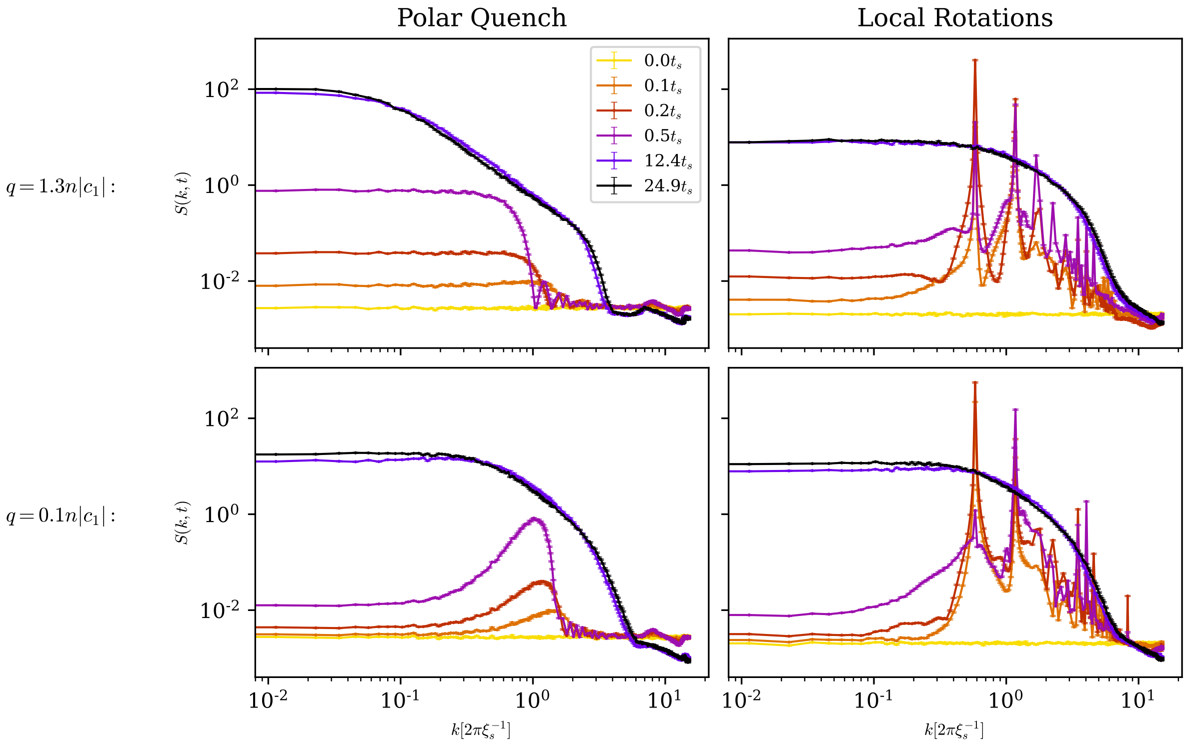

Figure 6.7: Comparison of the short-time evolution of the transverse spin structure factor $S(k,t) = \left\langle |F_\perp(k,t)|^2 \right\rangle$ for times up to $t = 25t_s$ for two different quenches. The left panels show the evolution for the polar quench system, whereas the right panels show the same for the case of 80 local rotations imprinted on the initial condition. All simulations were carried out with a particle number $N = 3 \cdot 10^6$, distributed over a physical length of $L = 220\mu m$, with interactions $|c_1/c_0| = 0.01$. The top row shows the quench to $q_f = 1.3n|c_1|$, whereas the bottom row to $q_f = 0.1n|c_1|$.

modes are more stable than the mode at $k \approx 2\pi/\xi_s$, where the bulk of the over-occupied modes reside, resulting in a slower quasi particle transfer from the over-occupied modes to the IR in the transverse spin, reflecting the fact that F_z excitations are building up rather than $F_\perp$. In contrast, for the case of $q_f = 1.3n|c_1|$, the unstable modes cause the written-in over-occupied modes to flatten more quickly as they are transported more quickly to the IR to build a flat plateau which seems to remain almost static.

This argument is also supported by the numerical results obtained by [51]. The stability analysis of dark-bright-dark (DBD) and dark-bright-bright (DBB) soliton solutions in the condensate led to the understanding that DBD configurations are only stable in various regimes of q. In contrast, DBB solutions seem to lose their structure quickly and decay into various degrees of freedom. In the process of writing in defects, we give rise to the formation of DBD solitons in the gas, which through spin changing collisions also change to DBB solitons [10]. Thus, depending on the value of q, such structures remain stable or decay more quickly, giving way to other excitations to dominate the dynamics of the system.

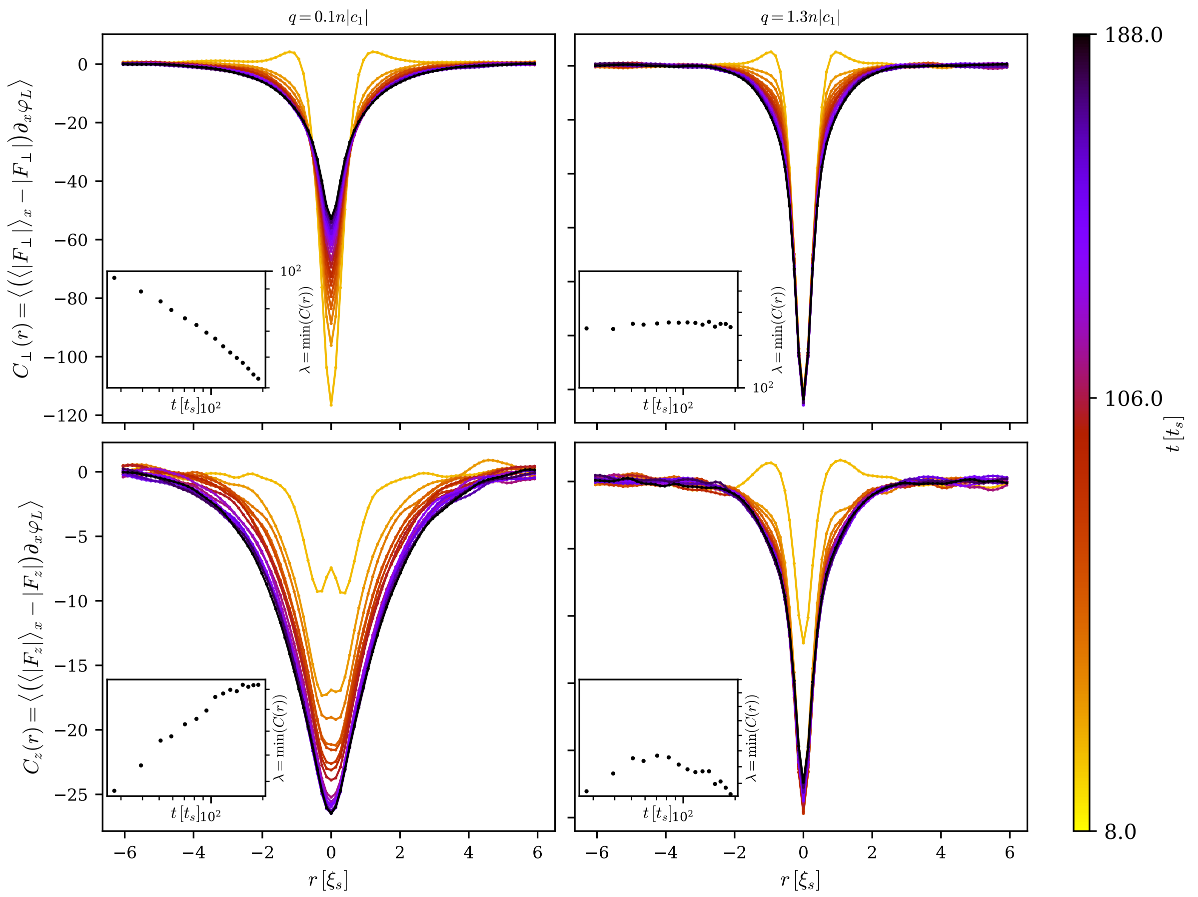

Figure 6.8: Spatial cross-correlation functions of mean spin deviations correlated with the gradient of the Larmor phase for two different quenches with 80 rotations, $N = 3 \cdot 10^6$, $L = 220\mu m$ and $|c_1/c_0| = 0.01$. Top row shows the cross-correlator for the transverse spin defects $C_\perp(r)$ as defined in Eq. (6.6). Bottom row shows the cross-correlator for the F_z excitations $C_z(r)$ as defined in Eq. (6.7). The figures to the right show the cross-correlators for $q_f = 1.3n|c_1|$ and the figures to the left show the cross-correlators for $q_f = 0.1n|c_1|$.

In order to gain a better understanding of this concept, we may study the structure of the defects more closely. The same analysis of the defects in $F_\perp$ as done for the polar quench case is not possible, since the signals given in the respective currents are ridden with noise which makes detection of single defects rather difficult. Therefore, we turn to cross-correlation functions. We define the following cross-correlations in analogy to our investigation of the $F_\perp$ defects in the polar quench case

$$C_\perp(r) = \Big\langle \Big(\langle |F_\perp| \rangle_x - |F_\perp|(x) \Big) \partial_x \varphi_L(y) \Big\rangle, \tag{6.6}$$

$$C_z(r) = \Big\langle \Big(\langle |F_z| \rangle_x - |F_z|(x) \Big) \partial_x \varphi_L(y) \Big\rangle, \tag{6.7}$$

where $\langle \cdots \rangle_x$ denotes the spatial average and $\langle \cdots \rangle$ denotes an average over many realizations. Fig. 6.8 shows the correlators Eq. (6.6) and (6.7) for differet times. As one readily sees, the two systems show, as expected, a strong signal in both correlators, but there exists a crucial difference between the two systems which we should discuss. First, the system quenched to

$q_f = 0.1n|c_1|$ shows a very present defect structure in the transverse spin which correlates to phase jumps in the Larmor phase, yet as the system evolves in time the presence of these kinds of defects seems to reduce with time, as seen by the weakening amplitude of the correlator. In contrast, the F_z structure of the defects shows the exact opposite behavior. In the beginning, there are only few localized F_z defects but as time goes by the system develops a strong presence of F_z defects, as seen by the increasing amplitude of the cross-correlator. This implies that the written-in defects play a less and less important role in the scaling of the system, whereas the F_z excitations corresponding to Larmor phase jumps gain importance, thus presumably leading the system to scale according to the length scale they set, as seen in Fig. 6.5.

The situation seems to develop differently for the quench to $q_f = 1.3n|c_1|$. In this case the written-in defects show themselves in the transverse spin from the beginning and remain stable, as seen by the constant amplitude of the correlator. The defects in the F_z direction though, must first develop over time as in the quench to $q_f = 0.1n|c_1|$, but once developed, they remain relatively stable and change their amplitude only slightly. It seems thus plausible to argue that the stability of the defects written in by the local rotations, as seen in the cross-correlators, leads to the prevention (or extreme slowing down) of scaling of length scales, since the disappearance or dissipation of defects as in the previous cases is no longer an effective mechanism.

Further investigation of the differences between the various systems may bring forth deeper insights as to the governing excitations and their scaling behavior in space and time. The newly gained understanding that the value of q_f is of great importance to the scaling behavior of the system may help us shed light on old and new acquired experimental results.

7. Conclusion

In the course of this thesis, we have numerically simulated and analyzed the one-dimensional spin-1 BEC, similar to a gas of ^{87}Rb atoms in the $F = 1$ hyperfine manifold. The system was prepared in an extreme out-of-equilibrium initial condition by performing a parameter quench of the quadratic Zeeman effect through a QPT from the polar phase to the easy-plane phase. The dynamics were then calculated using the TWA and a three-way split-step Fourier algorithm to solve the EOM. In our analysis, we have concentrated on the topological aspect of the time evolution of the system and studied the nature of defects which occupy the system.

In chapter 5, we have investigated a system prepared in the polar phase ground state and subsequently quenched into the easy-plane phase with $q_f = 0.9n|c_1|$. We observed the emergence of structures in the complex phase of the transverse spin, i.e., the Larmor phase. The self-similar temporal scaling of correlations in the transverse spin was studied, and the universal exponents $\alpha = 0.28 \pm 0.08$ and $\beta = 0.26 \pm 0.08$ were extracted numerically. This corroborates the earlier findings of [4]. To find an explanation to this scaling behavior, we turned to a topological analysis of the system by considering the gradient of the Larmor phase as a pure gauge field embedded in a scalar field theory. We found integer winding numbers in the system which change in time, presenting us with evidence of instantons in the system. The instantons were identified as vortices in space-time, and were subsequently localized on the grid with the help of a modified plaquette algorithm. Thereafter, we investigated the temporal decay in probability of instantonic excitations and found a stretched exponential behavior with an exponent $\delta = 0.311 \pm 0.004$. Furthermore, we used the topological current of the system to identify the spatio-temporal evolution of domain walls. We found that their associated length scale, given by their mean separation, scales in time with an exponent $\nu = 0.30 \pm 0.04$, which coincides with the exponents of the instanton decay and scaling of spectra within the error bounds.

The presence of instantonic excitations and their scaling behavior may imply a connection to an effective sine-Gordon model for Larmor phase excitations, which gives similar scaling analysis results [48]. To our knowledge, this is the first instance of evidence for such an effect in the regime of low interaction strength ratios $|c_1| \ll c_0$ being found to date. Research conducted in Ref. [52] has proposed a possible model for false vacuum decay in a spin-1 BEC and confirmed the predictions numerically for rather large interaction strength ratio $|c_1/c_0| \approx 0.5$. Thus, a deeper study of instantons in the spin-1 BEC may lead to exciting new results and understandings of the underlying mechanisms of various physical systems, e.g., false vacuum decay in the early universe or probing QED [53].

In the next step, we wrote in a dense ensemble of defects unto the polar phase initial condition utilizing local rotations in spin space. We followed this by quenching the system to $q_f = 0.9n|c_1|$. The dynamics observed in the system were qualitatively different than those in the polar quench, yet the scaling behavior of the system seemed to endure and stay within the realms of the $\alpha = \beta = 0.25$ hypothesized NTFP. Having introduced vector solitons into the system, the target manifold appears to have expanded from S^1 to S^2 as rich dynamics in the F_z direction were observed. As a result, topological arguments of the Larmor phase were rendered ineffective.

In chapter 6, we have investigated the numerical results in the context of discrepancies between the simulations and the experiment. The most prominent of which is the inability of numerical simulations to observe a scaling with $\alpha = \beta = 1/2$. We have argued that the expanded dimensionality of the system may have caused topological objects to become trivial, affecting the scaling behavior of the system. The hypothesis of altered dynamics through dimensionality was investigated by simulating a three-dimensional thin cylinder trap with the experimental parameters. Although the claim could not be fully verified or falsified, the simulated system still showed a scaling behavior close to the $\alpha = \beta = 1/4$ NTFP, leading us to search for the cause elsewhere.

The dependency of the scaling exponents on the quench parameter q_f was investigated for two initial conditions. It was found that by quenching to lower q_f, the system's vicinity to the QPT into the pure ferromagnetic phase gave rise to strong F_z excitations which took the form of dark solitons in the transverse spin degree of freedom. It was found that the mean separation of these objects scales in time with an exponent $\nu' = 0.44 \pm 0.01$, raising the hypothesis that a different NTFP will be observed depending on which kind of excitations is dominant. Thus, competing mixed effects of various excitations may give rise to a spectrum of effective exponents. For larger q_f, the scaling behavior of $\alpha = \beta = 1/4$ seemed to endure for the polar quench. In contrast, for an initial condition with 80 local rotations, it was found that for larger q_f the scaling slows down significantly. Investigation of the structure of the written-in defects and the naturally occuring defects has led us to believe they are two different kinds of excitations. The stability of the written-in defects was the main argument for the different scaling behaviors. For lower q_f we observed the decay of the solitonic excitations in $F_\perp$ and the rise of F_z excitations with time. For larger q_f we found that the F_z and $F_\perp$ defects remain stable at all times, thus presumably slowing down the time evolution of the governing length scales.

References

[1] Boris Nowak et al. *Non-thermal fixed points: universality, topology, and turbulence in Bose gases*. 2013. arXiv: 1302.1448 [cond-mat.quant-gas].

[2] Jürgen Berges, Alexander Rothkopf, and Jonas Schmidt. “Nonthermal Fixed Points: Effective Weak Coupling for Strongly Correlated Systems Far from Equilibrium”. In: *Phys. Rev. Lett.* 101 (4 2008), p. 041603. DOI: 10.1103/PhysRevLett.101.041603. URL: https://link.aps.org/doi/10.1103/PhysRevLett.101.041603.

[3] Maximilian Prüfer. “Experimentally testing quantum field theory concepts with spinor Bose gases far from equilibrium”. PhD thesis. Heidelberg Univesity, 2020. DOI: 10.11588/heidok.00027925. URL: https://archiv.ub.uni-heidelberg.de/volltextserver/27925/.

[4] Christian-Marcel Schmied et al. “Bidirectional universal dynamics in a spinor Bose gas close to a nonthermal fixed point”. In: *Physical Review A* 99.3 (2019). ISSN: 2469-9934. DOI: 10.1103/physreva.99.033611. URL: http://dx.doi.org/10.1103/PhysRevA.99.033611.

[5] Christian Marcel Schmied. “Universal Scaling Dynamics at Non-thermal Fixed Points in Multi-Component Bose Gases Far from Equilibrium”. PhD thesis. Heidelberg Univesity, 2020.

[6] Sebastian Erne et al. “Universal dynamics in an isolated one-dimensional Bose gas far from equilibrium”. In: *Nature* 563.7730 (2018), pp. 225229. ISSN: 1476-4687. DOI: 10.1038/s41586-018-0667-0. URL: http://dx.doi.org/10.1038/s41586-018-0667-0.

[7] Maximilian Prüfer et al. “Observation of universal dynamics in a spinor Bose gas far from equilibrium”. In: *Nature* 563.7730 (2018), pp. 217220. ISSN: 1476-4687. DOI: 10.1038/s41586-018-0659-0. URL: http://dx.doi.org/10.1038/s41586-018-0659-0.

[8] J. Berges et al. “Turbulent thermalization process in heavy-ion collisions at ultrarelativistic energies”. In: *Phys. Rev. D* 89 (7 2014), p. 074011. DOI: 10.1103/PhysRevD.89.074011. URL: https://link.aps.org/doi/10.1103/PhysRevD.89.074011.

[9] J. Berges. *Nonequilibrium Quantum Fields: From Cold Atoms to Cosmology*. 2015. arXiv: 1503.02907 [hep-ph].

[10] Stefan Lannig et al. “Collisions of Three-Component Vector Solitons in Bose-Einstein Condensates”. In: *Physical Review Letters* 125.17 (2020). ISSN: 1079-7114. DOI: 10.1103/physrevlett.125.170401. URL: http://dx.doi.org/10.1103/PhysRevLett.125.170401.

[11] J. Stenger et al. “Spin domains in ground-state BoseEinstein condensates”. In: *Nature* 396.6709 (1998), pp. 345348. ISSN: 1476-4687. DOI: 10.1038/24567. URL: http://dx.doi.org/10.1038/24567.

[12] Aleksandr N. Mikheev, Christian-Marcel Schmied, and Thomas Gasenzer. “Low-energy effective theory of nonthermal fixed points in a multicomponent Bose gas”. In: *Physical Review A* 99.6 (2019). ISSN: 2469-9934. DOI: 10.1103/physreva.99.063622. URL: http://dx.doi.org/10.1103/PhysRevA.99.063622.

[13] A.J. Bray. “Theory of phase-ordering kinetics”. In: *Advances in Physics* 43.3 (1994), pp. 357459. ISSN: 1460-6976. DOI: 10.1080/00018739400101505. URL: http://dx.doi.org/10.1080/00018739400101505.

[14] S. Lannig et al. “Experimental Observation of two non-thermal fixed points in a Spin-1 BEC (unpublished)”. 2022.

[15] Yuki Kawaguchi and Masahito Ueda. “Spinor Bose-Einstein condensates”. In: *Physics Reports* 520.5 (2012), pp. 253381. ISSN: 0370-1573. DOI: 10.1016/j.physrep.2012.07.005. URL: http://dx.doi.org/10.1016/j.physrep.2012.07.005.

[16] L.P. Pitaevskii and S. Stringari. *Bose-Einstein Condensation and Superfluidity*. International series of monographs on physics. Oxford University Press, 2016. ISBN: 9780198758884. URL: https://books.google.de/books?id=_y4ZswEACAAJ.

[17] Dan M. Stamper-Kurn and Masahito Ueda. “Spinor Bose gases: Symmetries, magnetism, and quantum dynamics”. In: *Rev. Mod. Phys.* 85 (3 2013), pp. 1191–1244. DOI: 10.1103/RevModPhys.85.1191. URL: https://link.aps.org/doi/10.1103/RevModPhys.85.1191.

[18] C.-M. Schmied, T. Gasenzer, and P. B. Blakie. “Violation of single-length-scaling dynamics via spin vortices in an isolated spin-1 Bose gas”. In: *Physical Review A* 100.3 (2019). ISSN: 2469-9934. DOI: 10.1103/physreva.100.033603. URL: http://dx.doi.org/10.1103/PhysRevA.100.033603.

[19] Philipp Kunkel et al. “Simultaneous Readout of Noncommuting Collective Spin Observables beyond the Standard Quantum Limit”. In: *Phys. Rev. Lett.* 123 (6 2019), p. 063603. DOI: 10.1103/PhysRevLett.123.063603. URL: https://link.aps.org/doi/10.1103/PhysRevLett.123.063603.

[20] Jürgen Berges and Thomas Gasenzer. "Quantum versus classical statistical dynamics of an ultracold Bose gas". In: *Phys. Rev. A* 76 (3 2007), p. 033604. DOI: 10.1103/PhysRevA.76.033604. URL: https://link.aps.org/doi/10.1103/PhysRevA.76.033604.

[21] Shun Uchino, Michikazu Kobayashi, and Masahito Ueda. "Bogoliubov theory and Lee-Huang-Yang corrections in spin-1 and spin-2 Bose-Einstein condensates in the presence of the quadratic Zeeman effect". In: *Phys. Rev. A* 81 (6 2010), p. 063632. DOI: 10.1103/PhysRevA.81.063632. URL: https://link.aps.org/doi/10.1103/PhysRevA.81.063632.

[22] Shun Uchino. "Spinor Bose gas in an elongated trap". In: *Phys. Rev. A* 91 (3 2015), p. 033605. DOI: 10.1103/PhysRevA.91.033605. URL: https://link.aps.org/doi/10.1103/PhysRevA.91.033605.

[23] Y. Nakamura et al. "Condition for emergence of complex eigenvalues in the Bogoliubovde Gennes equations". In: *Physical Review A* 77.4 (2008). ISSN: 1094-1622. DOI: 10.1103/physreva.77.043601. URL: http://dx.doi.org/10.1103/PhysRevA.77.043601.

[24] Christian Marcel Schmied. "Emergence of Structure in a Quenched (Quasi) One-dimensional Spin-1 Bose-Einstein Condensate in Comparison with Experiments". MA thesis. Heidelberg Univesity, 2020.

[25] T W B Kibble. "Topology of cosmic domains and strings". In: *Journal of Physics A: Mathematical and General* 9.8 (1976), pp. 1387–1398. DOI: 10.1088/0305-4470/9/8/029. URL: https://doi.org/10.1088/0305-4470/9/8/029.

[26] Xiaoquan Yu and P. B. Blakie. "Dark-soliton-like magnetic domain walls in a two-dimensional ferromagnetic superfluid". In: *Physical Review Research* 3.2 (2021). ISSN: 2643-1564. DOI: 10.1103/physrevresearch.3.023043. URL: http://dx.doi.org/10.1103/PhysRevResearch.3.023043.

[27] Maximilian Schmidt et al. "Non-thermal fixed points and solitons in a one-dimensional Bose gas". In: *New Journal of Physics* 14.7 (2012), p. 075005. DOI: 10.1088/1367-2630/14/7/075005. URL: https://doi.org/10.1088/1367-2630/14/7/075005.

[28] X.G. Wen. *Quantum Field Theory of Many-Body Systems:From the Origin of Sound to an Origin of Light and Electrons: From the Origin of Sound to an Origin of Light and Electrons*. Oxford Graduate Texts. OUP Oxford, 2004. ISBN: 9780198530947. URL: https://books.google.de/books?id=llnlrfdR4YgC.

[29] Nicholas Manton and Paul Sutcliffe. "Solitons general theory". In: *Topological Solitons*. Cambridge Monographs on Mathematical Physics. Cambridge University Press, 2004, pp. 75108. DOI: 10.1017/CBO9780511617034.005.

[30] A Patani, M Schlindwein, and Q Shafi. “Topological charges in field theory”. In: 9.9 (1976), pp. 1513–1520. DOI: `10.1088/0305-4470/9/9/012`. URL: `https://doi.org/10.1088/0305-4470/9/9/012`.

[31] F. Lenz. “Topological Concepts in Gauge Theories”. In: Feb. 2005, pp. 7–98. DOI: `10.1007/978-3-540-31532-2_2`.

[32] V. E. Zakharov and A. B. Shabat. “Interaction between solitons in a stable medium”. In: 1973.

[33] D J Frantzeskakis. “Dark solitons in atomic Bose–Einstein condensates: from theory to experiments”. In: 43.21 (2010), p. 213001. DOI: `10.1088/1751-8113/43/21/213001`. URL: `https://doi.org/10.1088/1751-8113/43/21/213001`.

[34] Hilmar Forkel. *A Primer on Instantons in QCD*. 2002. arXiv: `hep-ph/0009136 [hep-ph]`.

[35] J.H. Han. *Skyrmions in Condensed Matter*. Springer Tracts in Modern Physics. Springer International Publishing, 2017. ISBN: 9783319692463. URL: `https://books.google.de/books?id=tng5DwAAQBAJ`.

[36] Markus Karl and Thomas Gasenzer. “Strongly anomalous non-thermal fixed point in a quenched two-dimensional Bose gas”. In: *New Journal of Physics* 19.9 (2017), p. 093014. ISSN: 1367-2630. DOI: `10.1088/1367-2630/aa7eeb`. URL: `http://dx.doi.org/10.1088/1367-2630/aa7eeb`.

[37] Markus Karl, Boris Nowak, and Thomas Gasenzer. “Universal scaling at nonthermal fixed points of a two-component Bose gas”. In: *Physical Review A* 88.6 (2013). ISSN: 1094-1622. DOI: `10.1103/physreva.88.063615`. URL: `http://dx.doi.org/10.1103/PhysRevA.88.063615`.

[38] Thomas Gasenzer et al. “Gauge turbulence, topological defect dynamics, and condensation in Higgs models”. In: *Nuclear Physics A* 930 (2014), pp. 163186. ISSN: 0375-9474. DOI: `10.1016/j.nuclphysa.2014.07.030`. URL: `http://dx.doi.org/10.1016/j.nuclphysa.2014.07.030`.

[39] Christian-Marcel Schmied, Aleksandr N. Mikheev, and Thomas Gasenzer. “Non-thermal fixed points: Universal dynamics far from equilibrium”. In: *International Journal of Modern Physics A* 34.29 (2019), p. 1941006. ISSN: 1793-656X. DOI: `10.1142/s0217751x19410069`. URL: `http://dx.doi.org/10.1142/S0217751X19410069`.

[40] C.-M. Schmied et al. “Stability analysis of ground states in a one-dimensional trapped spin-1 Bose gas”. In: *Communications in Nonlinear Science and Numerical Simulation* 83 (2020), p. 105050. ISSN: 1007-5704. DOI: `10.1016/j.cnsns.2019.105050`. URL: `http://dx.doi.org/10.1016/j.cnsns.2019.105050`.

[41] Anatoli Polkovnikov. "Phase space representation of quantum dynamics". In: *Annals of Physics* 325.8 (2010), pp. 1790–1852. ISSN: 0003-4916. DOI: `https://doi.org/10.1016/j.aop.2010.02.006`. URL: `https://www.sciencedirect.com/science/article/pii/S0003491610000382`.

[42] P.B. Blakie et al. "Dynamics and statistical mechanics of ultra-cold Bose gases using c-field techniques". In: *Advances in Physics* 57.5 (2008), pp. 363455. ISSN: 1460-6976. DOI: `10.1080/00018730802564254`. URL: `http://dx.doi.org/10.1080/00018730802564254`.

[43] J. A. C. Weideman and B. M. Herbst. "Split-Step Methods for the Solution of the Nonlinear Schrodinger Equation". In: *SIAM Journal on Numerical Analysis* 23.3 (1986), pp. 485–507. ISSN: 00361429. URL: `http://www.jstor.org/stable/2157521`.

[44] Hanquan Wang. "A time-splitting spectral method for computing dynamics of spinor F=1 BoseEinstein condensates". In: *International Journal of Computer Mathematics* 84.6 (2007), pp. 925–944. DOI: `10.1080/00207160701458369`. eprint: `https://doi.org/10.1080/00207160701458369`. URL: `https://doi.org/10.1080/00207160701458369`.

[45] Weizhu Bao and Yanzhi Zhang. "Dynamical Laws of the Coupled Gross-Pitaevskii Equations for Spin-1 Bose-Einstein Condensates". In: *Methods and Applications of Analysis* 17.1 (2010), pp. 49 –80. DOI: `maa/1291644608`. URL: `https://doi.org/`.

[46] Isara Chantesana, Asier Piñeiro Orioli, and Thomas Gasenzer. "Kinetic theory of nonthermal fixed points in a Bose gas". In: *Phys. Rev. A* 99 (4 2019), p. 043620. DOI: `10.1103/PhysRevA.99.043620`. URL: `https://link.aps.org/doi/10.1103/PhysRevA.99.043620`.

[47] Asier Piñeiro Orioli, Kirill Boguslavski, and Jürgen Berges. "Universal self-similar dynamics of relativistic and nonrelativistic field theories near nonthermal fixed points". In: *Phys. Rev. D* 92 (2 2015), p. 025041. DOI: `10.1103/PhysRevD.92.025041`. URL: `https://link.aps.org/doi/10.1103/PhysRevD.92.025041`.

[48] P. Heinen et al. "Scaling in the sine-Gordon model (unpublished)". 2022.

[49] Philipp Heinen. "Phase Correlators in Gross-Pitaevskii Systems Far from Equilibrium". MA thesis. Heidelberg Univesity, 2020.

[50] Kevin Geier. "Dynamics of Vector Solitons in Spinor Bose-Einstein Condensates". MA thesis. Heidelberg Univesity, 2017.

[51] C.-M. Schmied and P. G. Kevrekidis. "Dark-antidark spinor solitons in spin-1 Bose gases". In: *Phys. Rev. A* 102 (5 2020), p. 053323. DOI: `10.1103/PhysRevA.102.053323`. URL: `https://link.aps.org/doi/10.1103/PhysRevA.102.053323`.

[52] Thomas P. Billam, Kate Brown, and Ian G. Moss. *False vacuum decay in an ultracold spin-1 Bose gas*. 2022. arXiv: `2108.05740 [cond-mat.quant-gas]`.

[53] V Kasper et al. “Implementing quantum electrodynamics with ultracold atomic systems”. In: *New Journal of Physics* 19.2 (2017), p. 023030. ISSN: 1367-2630. DOI: 10.1088/1367-2630/aa54e0. URL: http://dx.doi.org/10.1088/1367-2630/aa54e0.

A. Appendix: Spectra for q Dependancy

A.1 Polar Quench

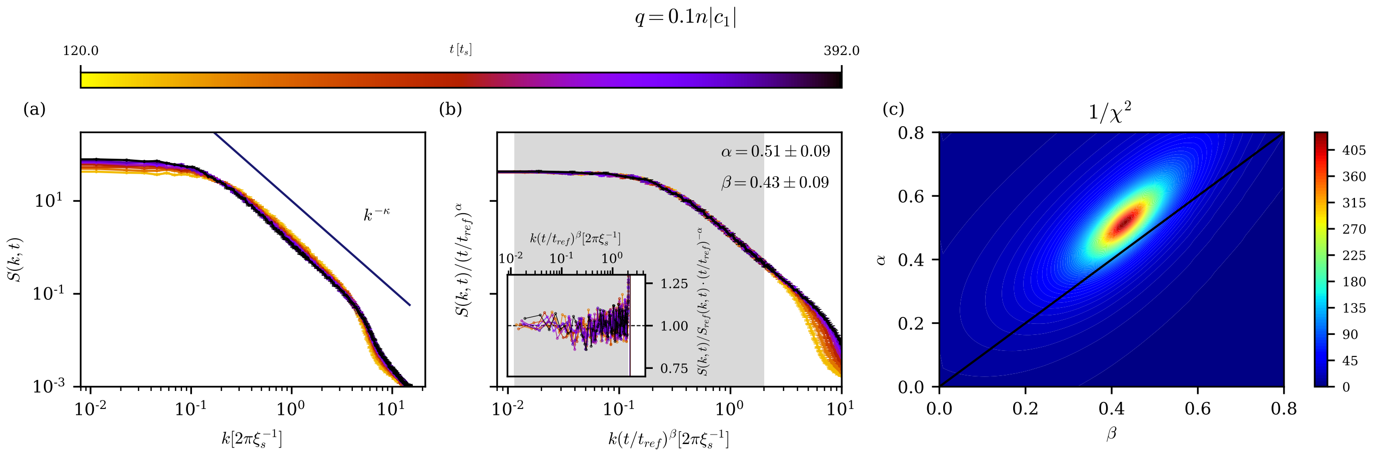

Figure A.1: Spectra of the transverse spin structure factor for a BEC prepared in the polar phase with $N = 3 \cdot 10^6$, $L = 220\mu m$ and $|c_1/c_0| = 0.01$ and quenched to $q_f = 0.1n|c_1|$. (a): Unscaled raw spectra from $t = 120t_s$ to $t = 392t_s$. A power law of $\sim k^{-2}$ was plotted as a visual aid. (b): Rescaled spectra and the resulting scaling exponents. The inset shows the residuals w.r.t the reference spectrum. (c): Contour plot of the inverse cumulative error $1/\chi^2$

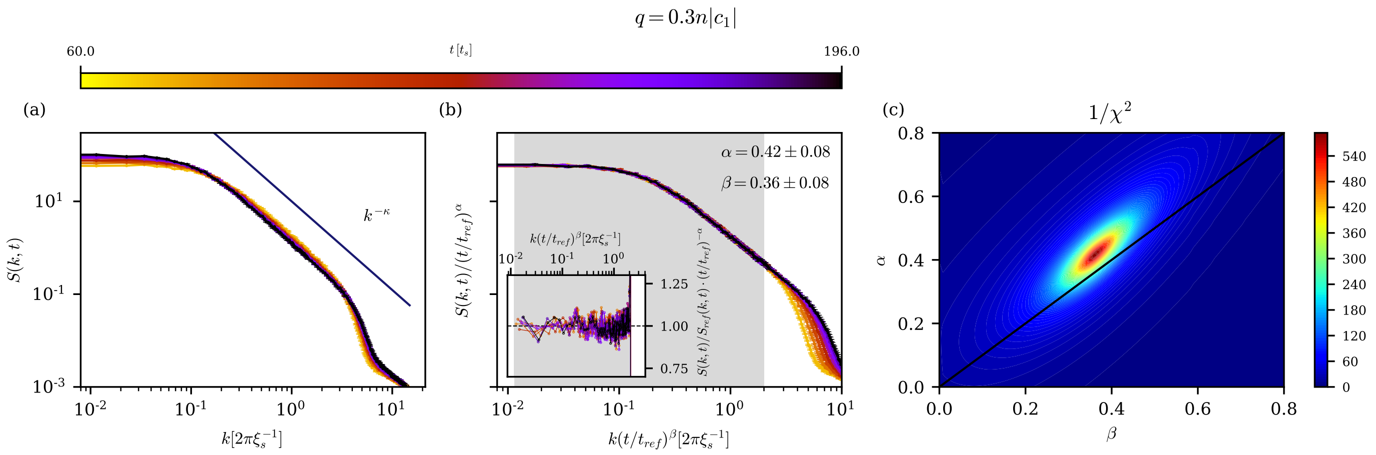

Figure A.2: Spectra of the transverse spin structure factor for a BEC prepared in the polar phase with $N = 3 \cdot 10^6$, $L = 220\mu m$ and $|c_1/c_0| = 0.01$ and quenched to $q_f = 0.3n|c_1|$. (a): Unscaled raw spectra from $t = 60t_s$ to $t = 196t_s$. A power law of $\sim k^{-2}$ was plotted as a visual aid. (b): Rescaled spectra and the resulting scaling exponents. The inset shows the residuals w.r.t the reference spectrum. (c): Contour plot of the inverse cumulative error $1/\chi^2$

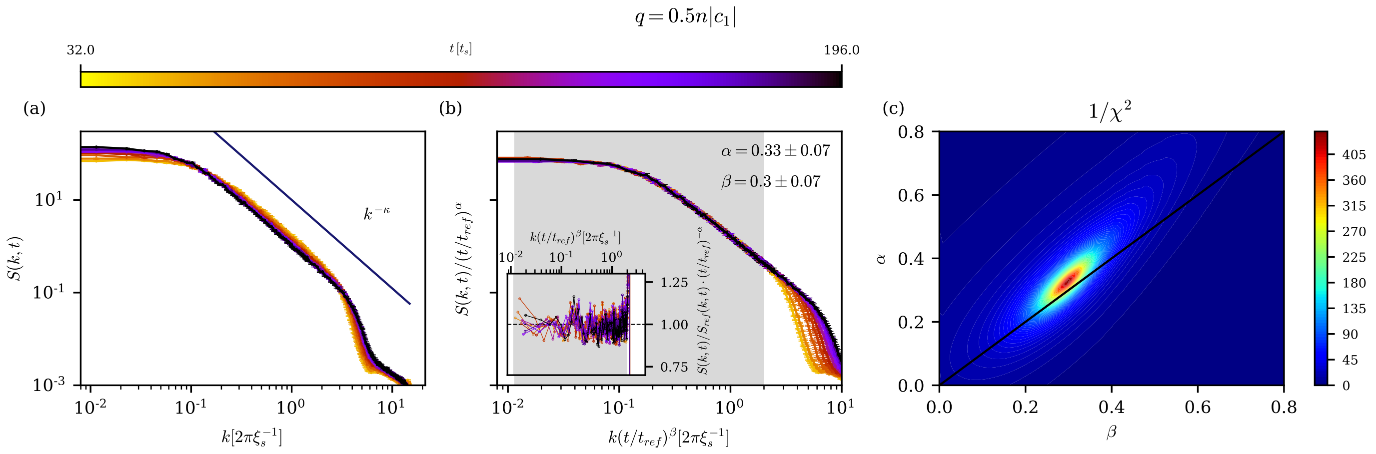

Figure A.3: Spectra of the transverse spin structure factor for a BEC prepared in the polar phase with $N = 3 \cdot 10^6$, $L = 220\mu m$ and $|c_1/c_0| = 0.01$ and quenched to $q_f = 0.5n|c_1|$. (a): Unscaled raw spectra from $t = 32t_s$ to $t = 196t_s$. A power law of $\sim k^{-2}$ was plotted as a visual aid. (b): Rescaled spectra and the resulting scaling exponents. The inset shows the residuals w.r.t the reference spectrum. (c): Contour plot of the inverse cumulative error $1/\chi^2$

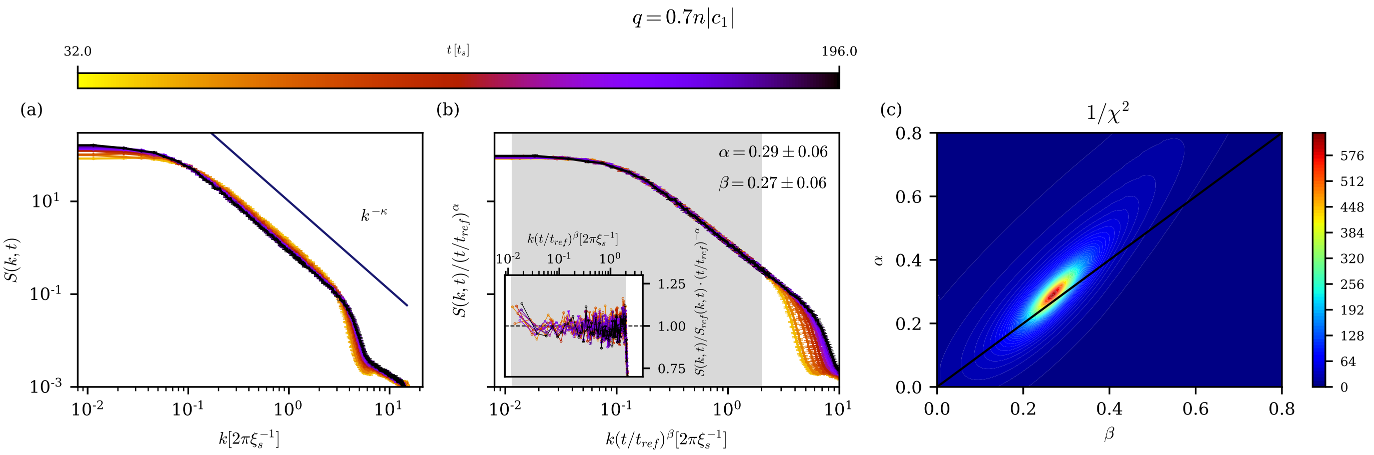

Figure A.4: Spectra of the transverse spin structure factor for a BEC prepared in the polar phase with $N = 3 \cdot 10^6$, $L = 220\mu m$ and $|c_1/c_0| = 0.01$ and quenched to $q_f = 0.7n|c_1|$. (a): Unscaled raw spectra from $t = 32t_s$ to $t = 196t_s$. A power law of $\sim k^{-2}$ was plotted as a visual aid. (b): Rescaled spectra and the resulting scaling exponents. The inset shows the residuals w.r.t the reference spectrum. (c): Contour plot of the inverse cumulative error $1/\chi^2$

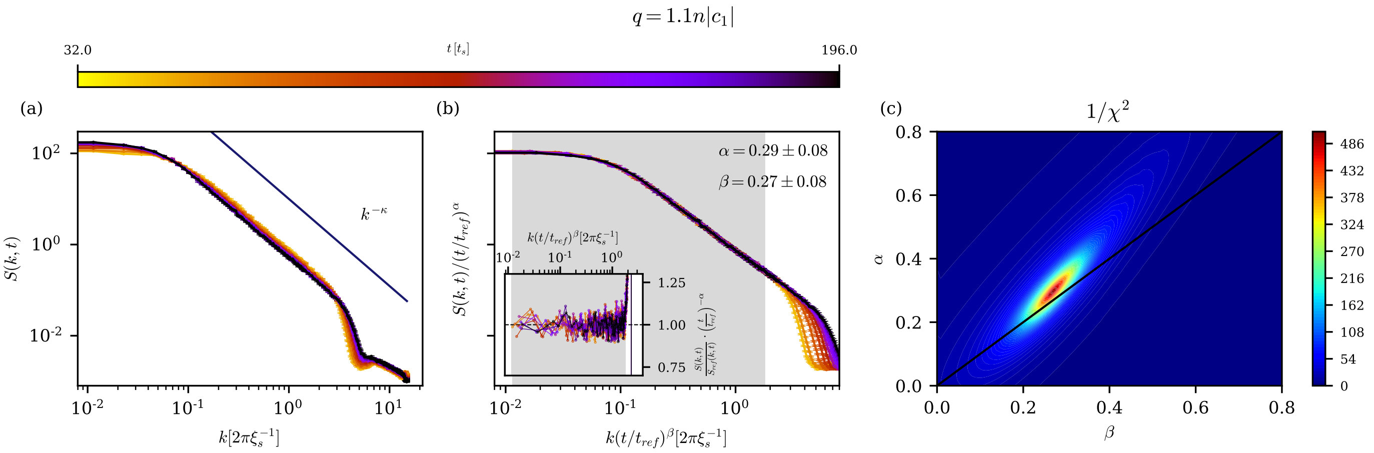

Figure A.5: Spectra of the transverse spin structure factor for a BEC prepared in the polar phase with $N = 3 \cdot 10^6$, $L = 220\mu m$ and $|c_1/c_0| = 0.01$ and quenched to $q_f = 1.1n|c_1|$. (a): Unscaled raw spectra from $t = 32t_s$ to $t = 196t_s$. A power law of $\sim k^{-2}$ was plotted as a visual aid. (b): Rescaled spectra and the resulting scaling exponents. The inset shows the residuals w.r.t the reference spectrum. (c): Contour plot of the inverse cumulative error $1/\chi^2$

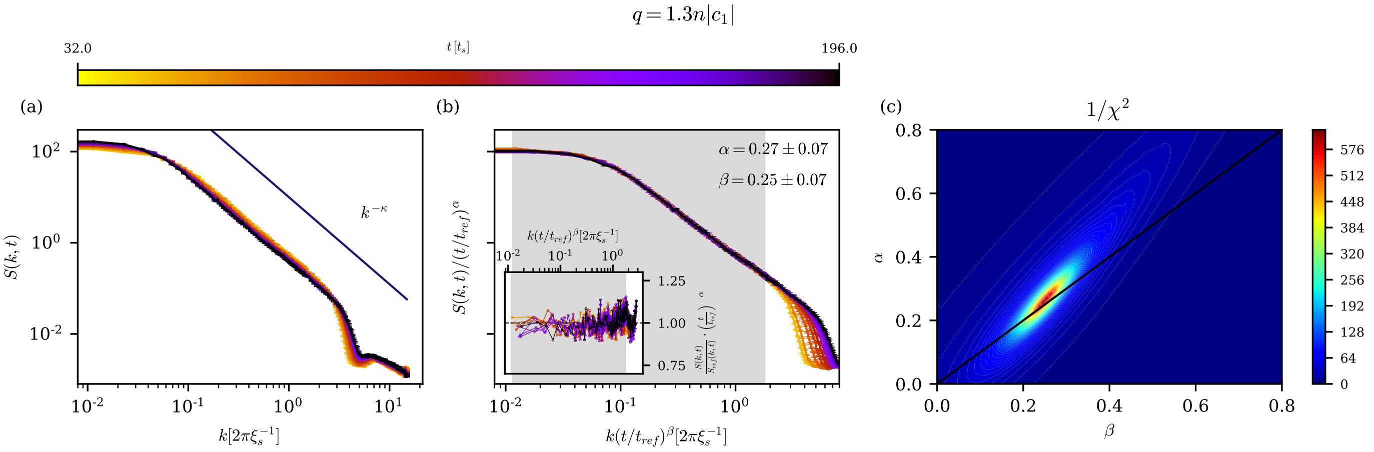

Figure A.6: Spectra of the transverse spin structure factor for a BEC prepared in the polar phase with $N = 3 \cdot 10^6$, $L = 220\mu m$ and $|c_1/c_0| = 0.01$ and quenched to $q_f = 1.3n|c_1|$. (a): Unscaled raw spectra from $t = 32t_s$ to $t = 196t_s$. A power law of $\sim k^{-2}$ was plotted as a visual aid. (b): Rescaled spectra and the resulting scaling exponents. The inset shows the residuals w.r.t the reference spectrum. (c): Contour plot of the inverse cumulative error $1/\chi^2$

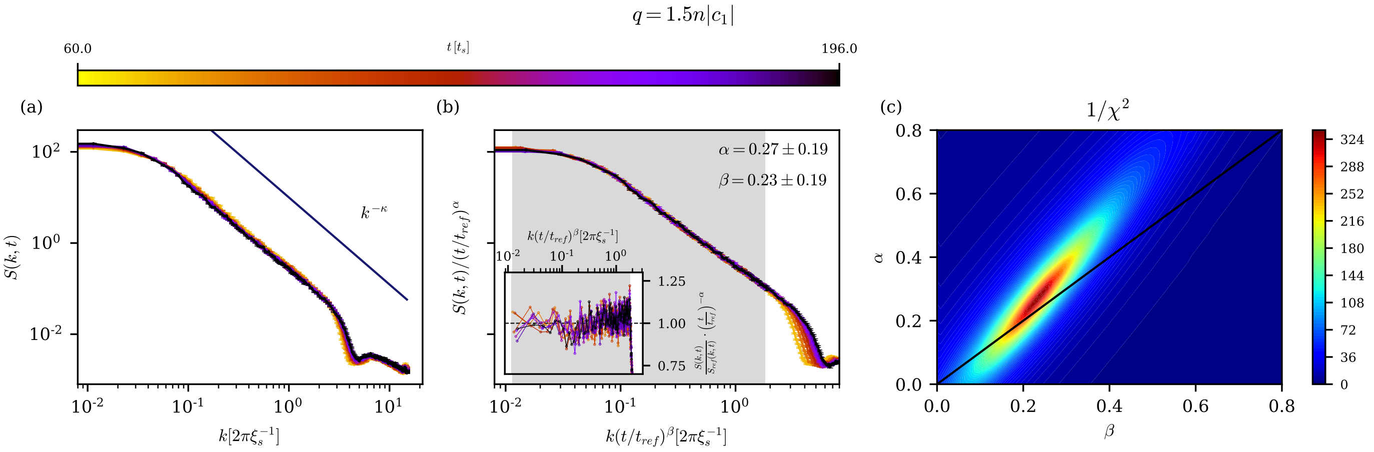

Figure A.7: Spectra of the transverse spin structure factor for a BEC prepared in the polar phase with $N = 3 \cdot 10^6$, $L = 220\mu m$ and $|c_1/c_0| = 0.01$ and quenched to $q_f = 1.5n|c_1|$. (a): Unscaled raw spectra from $t = 60t_s$ to $t = 196t_s$. A power law of $\sim k^{-2}$ was plotted as a visual aid. (b): Rescaled spectra and the resulting scaling exponents. The inset shows the residuals w.r.t the reference spectrum. (c): Contour plot of the inverse cumulative error $1/\chi^2$

A.2 80 Rotations

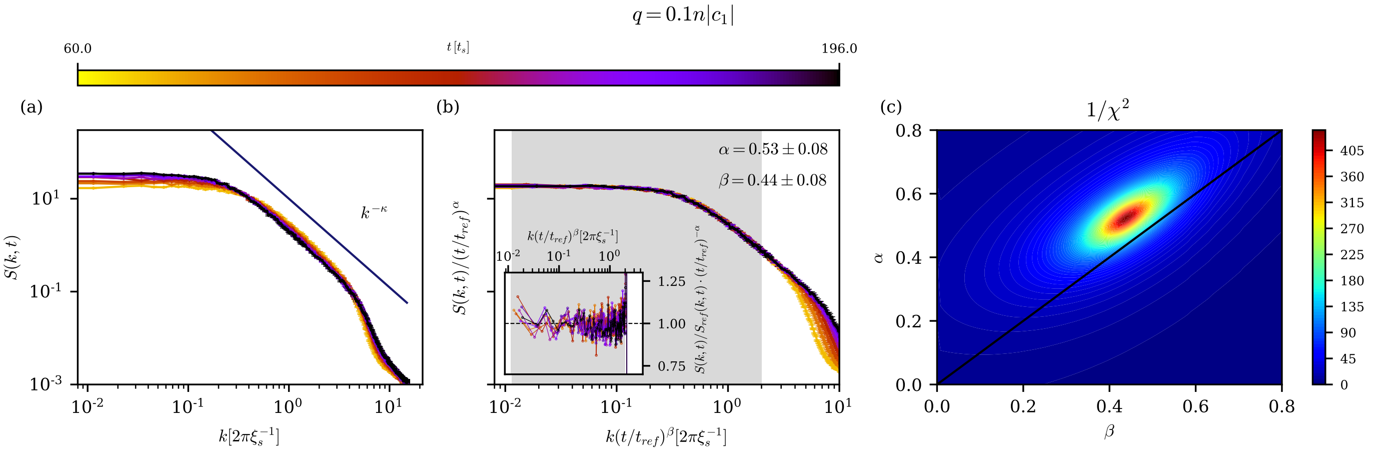

Figure A.8: Spectra of the transverse spin structure factor for a BEC prepared with 80 local rotations in the polar phase with $N = 3 \cdot 10^6$, $L = 220\mu m$ and $|c_1/c_0| = 0.01$ and quenched to $q_f = 0.1n|c_1|$. (a): Unscaled raw spectra from $t = 60t_s$ to $t = 196t_s$. A power law of $\sim k^{-2}$ was plotted as a visual aid. (b): Rescaled spectra and the resulting scaling exponents. The inset shows the residuals w.r.t the reference spectrum. (c): Contour plot of the inverse cumulative error $1/\chi^2$

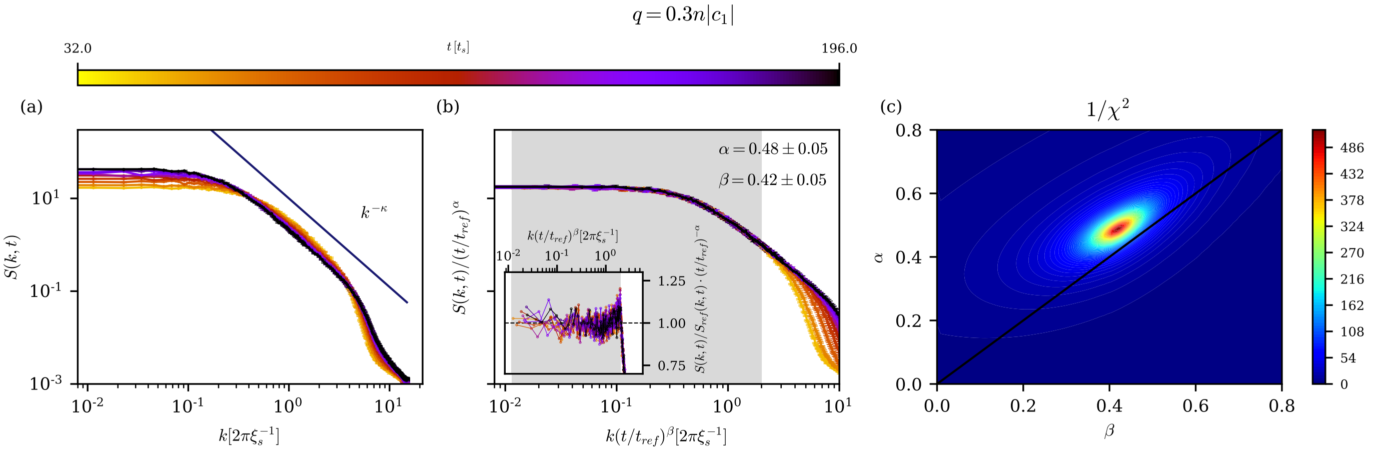

Figure A.9: Spectra of the transverse spin structure factor for a BEC prepared with 80 local rotations in the polar phase with $N = 3 \cdot 10^6$, $L = 220\mu m$ and $|c_1/c_0| = 0.01$ and quenched to $q_f = 0.3n|c_1|$. (a): Unscaled raw spectra from $t = 32t_s$ to $t = 196t_s$. A power law of $\sim k^{-2}$ was plotted as a visual aid. (b): Rescaled spectra and the resulting scaling exponents. The inset shows the residuals w.r.t the reference spectrum. (c): Contour plot of the inverse cumulative error $1/\chi^2$

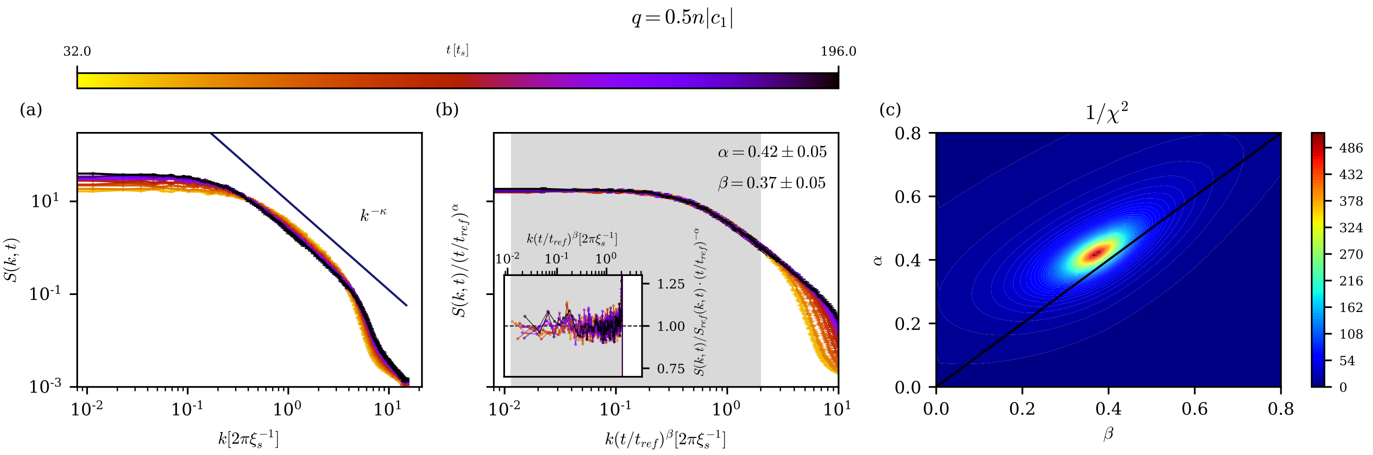

Figure A.10: Spectra of the transverse spin structure factor for a BEC prepared with 80 local rotations in the polar phase with $N = 3 \cdot 10^6$, $L = 220\mu m$ and $|c_1/c_0| = 0.01$ and quenched to $q_f = 0.5n|c_1|$. (a): Unscaled raw spectra from $t = 32t_s$ to $t = 196t_s$. A power law of $\sim k^{-2}$ was plotted as a visual aid. (b): Rescaled spectra and the resulting scaling exponents. The inset shows the residuals w.r.t the reference spectrum. (c): Contour plot of the inverse cumulative error $1/\chi^2$

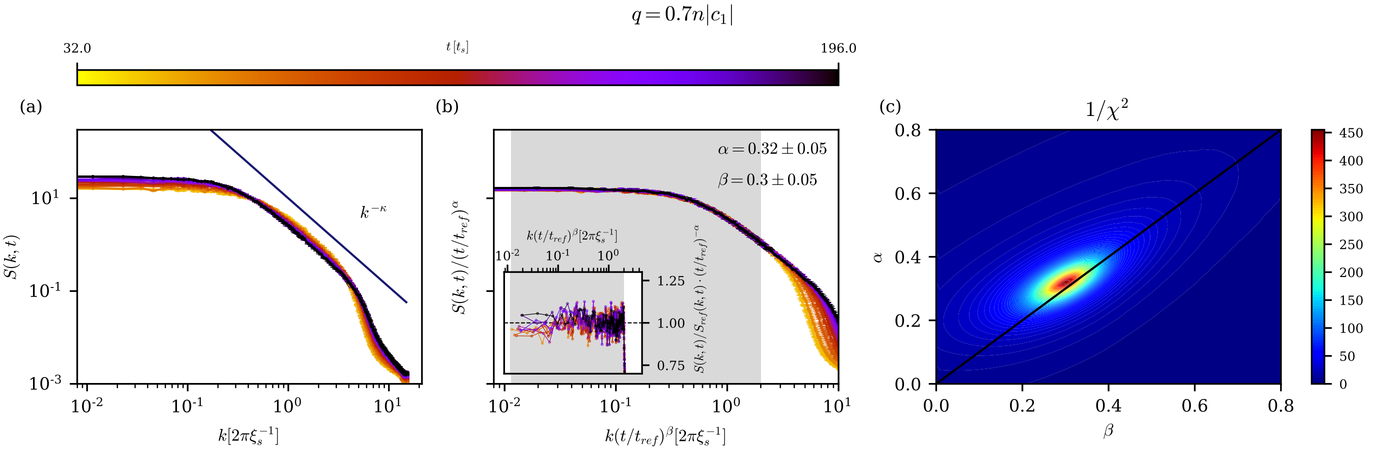

Figure A.11: Spectra of the transverse spin structure factor for a BEC prepared with 80 local rotations in the polar phase with $N = 3 \cdot 10^6$, $L = 220\mu m$ and $|c_1/c_0| = 0.01$ and quenched to $q_f = 0.7n|c_1|$. (a): Unscaled raw spectra from $t = 32t_s$ to $t = 196t_s$. A power law of $\sim k^{-2}$ was plotted as a visual aid. (b): Rescaled spectra and the resulting scaling exponents. The inset shows the residuals w.r.t the reference spectrum. (c): Contour plot of the inverse cumulative error $1/\chi^2$

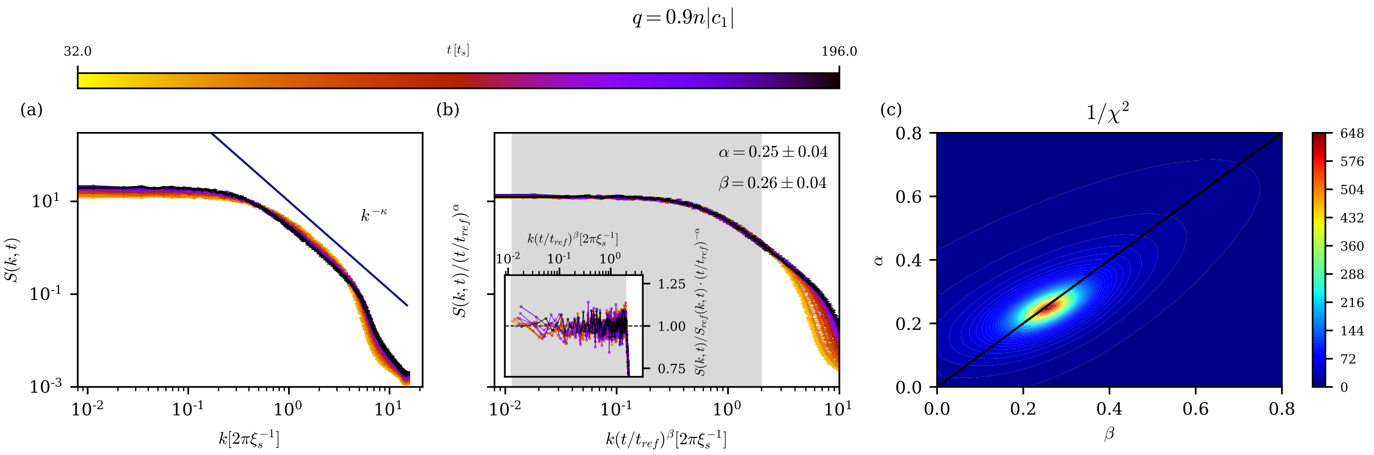

Figure A.12: Spectra of the transverse spin structure factor for a BEC prepared with 80 local rotations in the polar phase with $N = 3 \cdot 10^6$, $L = 220\mu m$ and $|c_1/c_0| = 0.01$ and quenched to $q_f = 0.9n|c_1|$. (a): Unscaled raw spectra from $t = 32t_s$ to $t = 196t_s$. A power law of $\sim k^{-2}$ was plotted as a visual aid. (b): Rescaled spectra and the resulting scaling exponents. The inset shows the residuals w.r.t the reference spectrum. (c): Contour plot of the inverse cumulative error $1/\chi^2$

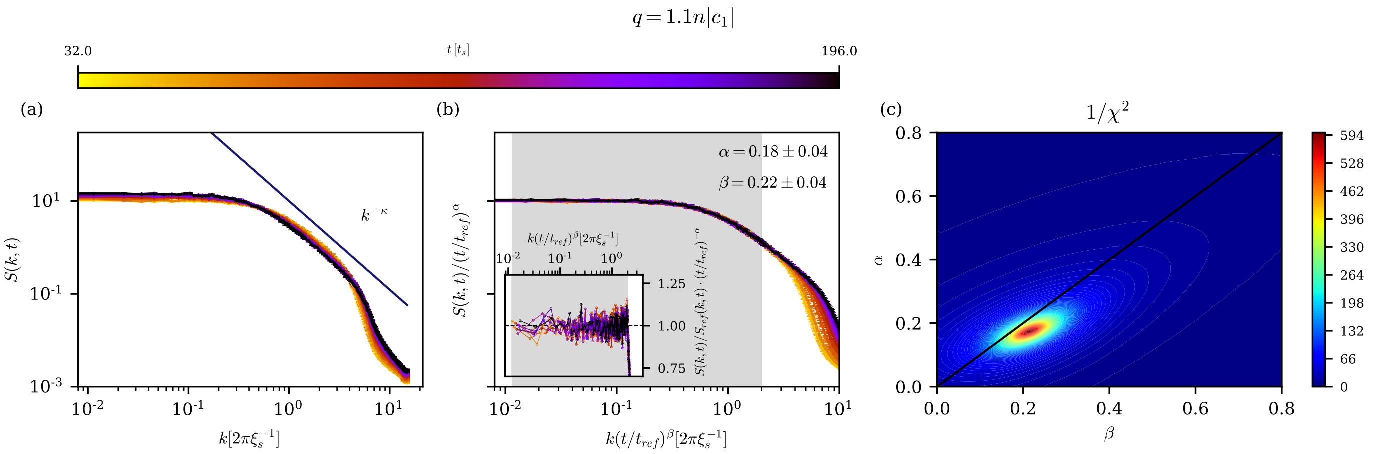

Figure A.13: Spectra of the transverse spin structure factor for a BEC prepared with 80 local rotations in the polar phase with $N = 3 \cdot 10^6$, $L = 220\mu m$ and $|c_1/c_0| = 0.01$ and quenched to $q_f = 1.1n|c_1|$. (a): Unscaled raw spectra from $t = 32t_s$ to $t = 196t_s$. A power law of $\sim k^{-2}$ was plotted as a visual aid. (b): Rescaled spectra and the resulting scaling exponents. The inset shows the residuals w.r.t the reference spectrum. (c): Contour plot of the inverse cumulative error $1/\chi^2$

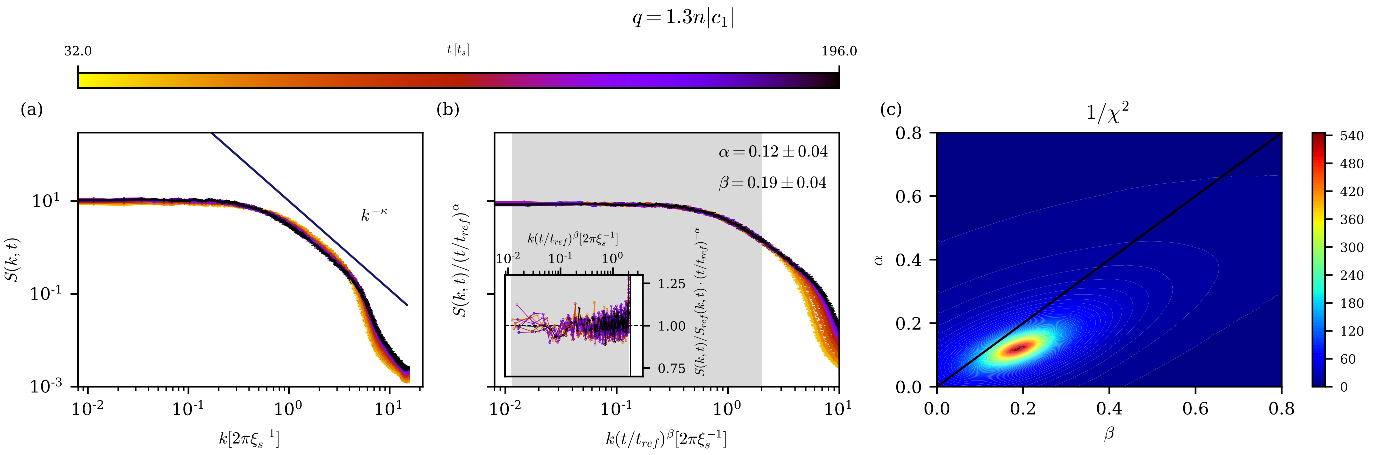

Figure A.14: Spectra of the transverse spin structure factor for a BEC prepared with 80 local rotations in the polar phase with $N = 3 \cdot 10^6$, $L = 220\mu m$ and $|c_1/c_0| = 0.01$ and quenched to $q_f = 1.3n|c_1|$. (a): Unscaled raw spectra from $t = 32t_s$ to $t = 196t_s$. A power law of $\sim k^{-2}$ was plotted as a visual aid. (b): Rescaled spectra and the resulting scaling exponents. The inset shows the residuals w.r.t the reference spectrum. (c): Contour plot of the inverse cumulative error $1/\chi^2$

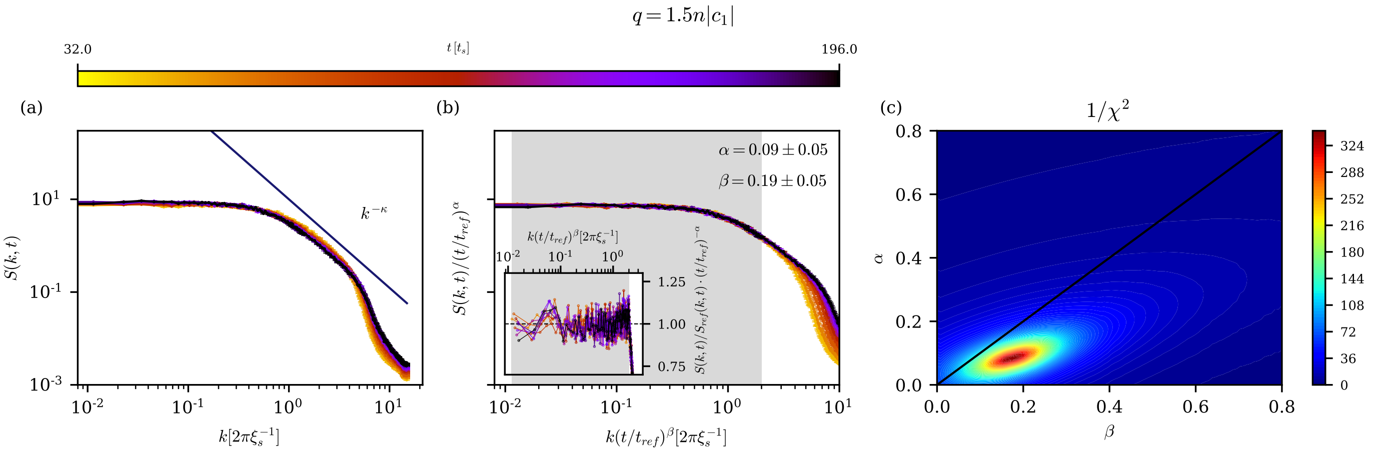

Figure A.15: Spectra of the transverse spin structure factor for a BEC prepared with 80 local rotations in the polar phase with $N = 3 \cdot 10^6$, $L = 220\mu m$ and $|c_1/c_0| = 0.01$ and quenched to $q_f = 1.5n|c_1|$. (a): Unscaled raw spectra from $t = 32t_s$ to $t = 196t_s$. A power law of $\sim k^{-2}$ was plotted as a visual aid. (b): Rescaled spectra and the resulting scaling exponents. The inset shows the residuals w.r.t the reference spectrum. (c): Contour plot of the inverse cumulative error $1/\chi^2$

Acknowledgments

At this point, I would like to express my thanks and appreciation to all those who have supported and accompanied me during the course of completing this thesis.

First and foremost, I want to thank Thomas Gasenzer for allowing me to work on this project in his group. The countless discussions, suggestions and presented opportunities under his supervision have been crucial for the progress in this research. His impressive approach to research is one of the many reasons i look forward to working with him in the future.

I would also like to express my gratitude to Christian Schmied for his hard work on making the code needed for this research as accessible and efficient as possible. Moreover, for the time he spent introducing me to the numerical and physical background involved in this field of research. Furthermore, many thanks to Paul Große-Bley for his unending patience while helping me deal with the new concepts of programming on GPUs and the long times spent debugging. My thanks go to Aleksandr and Philipp for discussions regarding the interpretation of numerical data.

I want to give my thanks to Markus Oberthaler for his consent to take over the role of the second supervisor in this thesis. Moreover, the collaboration with his research group and especially with Stefan Lannig has led to many interesting developments in this thesis. Without their precious input and teamwork, my work would not have been the same. The cooperation with the experiment was an interesting and exciting opportunity, which i look forward to continue.

Finally, I would like to express my deep gratitude to all my friends, family and the person closest to me: my wonderful wife. This thesis was written in difficult times during a global pandemic and the overwhelming support by friends and family has helped to keep me motivated, focused and achieve my goals. You’re all irreplaceable!

Erklärung

Ich versichere, dass ich diese Arbeit selbstständig verfasst und keine anderen als die angegebenen Quellen und Hilfsmittel benutzt habe.

Heidelberg, den ..., 24/02/2022